Title
Semiconductor Nanowires and Nanotubes for Energy Conversion

Author
Fardy, Melissa Anne

Publication Date
2010

Peer reviewed|Thesis/dissertation

Semiconductor Nanowires and Nanotubes for Energy Conversion

By

Melissa Anne Fardy

A dissertation submitted in partial satisfaction

of the requirement for the degree

Doctor of Philosophy

in

Chemistry

and the Designated Emphasis

in

Nanoscale Science and Engineering

in the

Graduate Division

of the

University of California, Berkeley

Committee in Charge:

Professor Peidong Yang, Chair
Professor Angelica Stacy
Professor Junqiao Wu

Fall 2010

Semiconductor Nanowires and Nanotubes for Energy Conversion

by Melissa Anne Fardy

Abstract

Semiconductor Nanowires and Nanotubes for Energy Conversion

by

Melissa Anne Fardy

Doctor of Philosophy in Chemistry

with a Designated Emphasis in Nanoscale Science and Engineering

University of California, Berkeley

Professor Peidong Yang, Chair

In recent years semiconductor nanowires and nanotubes have garnered increased attention for their unique properties. With their nanoscale dimensions comes high surface area and quantum confinement, promising enhancements in a wide range of applications. 1-dimensional nanostructures are especially attractive for energy conversion applications where photons, phonons, and electrons come into play. Since the bohr exciton radius and phonon and electron mean free paths are on the same length scales as nanowire diameters, optical, thermal, and electrical properties can be tuned by simple nanowire size adjustments. In addition, the high surface area inherent to nanowires and nanotubes lends them towards efficient charge separation and superior catalytic performance.

In thermoelectric power generation, the nanoscale wire diameter can effectively scatter phonons, promoting reductions in thermal conductivity and enhancements in the thermoelectric figure of merit. To that end, single-crystalline arrays of PbS, PbSe, and PbTe nanowires have been synthesized by a chemical vapor transport approach. The electrical and thermal transport properties of the nanowires were characterized to investigate their potential as thermoelectric materials. Compared to bulk, the lead chalcogenide nanowires exhibit reduced thermal conductivity below 100 K by up to 3 orders of magnitude, suggesting that they may be promising thermoelectric materials. Smaller diameters and increased surface roughness are expected to give additional enhancements.

The solution-phase synthesis of PbSe nanowires via oriented attachment of nanoparticles enables facile surface engineering and diameter control. Branched PbSe nanowires synthesized by this approach showed near degenerately doped charge carrier concentrations. Compared to the bulk, the PbSe nanowires exhibited a similar Seebeck coefficient and a significant reduction in thermal conductivity in the temperature range 20 K to 300 K. Thermal annealing of the PbSe nanowires allowed their thermoelectric properties to be controllably tuned by increasing their carrier concentration or hole mobility. After optimal annealing, single PbSe nanowires exhibited a thermoelectric figure of merit (ZT) of 0.12 at 300 K. In addition, using a field-effect gated device, the Seebeck coefficient of single PbSe

nanowires could be tuned from 64 to 193 $\mu V \cdot K^{-1}$. This direct electrical field control of the electrical conductivity and Seebeck coefficient suggests a powerful strategy for optimizing *ZT* in thermoelectric devices and these results represent the first demonstration of field-effect modulation of the thermoelectric figure of merit in a single semiconductor nanowire. This novel strategy for thermoelectric property modulation could prove especially important in optimizing the thermoelectric properties of semiconductors where reproducible doping is difficult to achieve.

Recent theoretical work has shown large enhancements in *ZT* for single-crystal nanowires containing nanoscale interfaces along their lengths. $M_2O_3(ZnO)_n$ (*M* = In, Ga, Fe) superlattice nanowires were synthesized via a novel solid-state diffusion approach to investigate this possible enhancement. Using atomic resolution Z-contrast STEM imaging a detailed structural analysis was performed on $In_{2-x}Ga_xO_3(ZnO)_n$ nanowires, leading to the discovery that octahedral inclusions within the superlattice structure are likely generated through a defect-assisted process. Single-nanowire thermal and electrical measurements on $In_{2-x}Ga_xO_3(ZnO)_n$ reveal a simultaneous improvement in all contributing factors to the thermoelectric figure of merit, giving an order of magnitude enhancement over similar bulk materials at room temperature. This is the first report of enhancement of all three thermoelectric parameters (Seebeck coefficient, electrical conductivity, and thermal resistivity) for a nanowire system.

Photoelectrochemical water splitting is another exciting renewable energy application that can benefit from the high surface area of nanomaterials. Recently, $(Ga_{1-x}Zn_x)(N_{1-x}O_x)$ has gained widespread attention as a high efficiency material for visible-light-driven H_2 and O_2 generation. To improve the crystallinity of the material and reduce charge recombination $(Ga_{1-x}Zn_x)(N_{1-x}O_x)$ nanotubes were synthesized by epitaxial coating of GaN onto ZnO nanowires. The nanotubes were single-crystalline, solid solutions of GaN and ZnO with ZnO compositions up to 10% and bandgaps as low as 2.6 eV. Incorporation of In into these nanotubes pushed the absorption even further into the visible. After decoration with $Rh_{2-y}Cr_yO_3$ nanoparticle cocatalysts, $(Ga_{1-x}Zn_x)(N_{1-x}O_x)$ nanotubes spontaneously generated H_2 in aqueous solutions under illumination. The photoanodic properties of these nanotubes are still under investigation.

The significant reductions in thermal conductivity achieved using lead chalcogenide and $In_{2-x}Ga_xO_3(ZnO)_n$ nanowires highlight their use in thermoelectric power generation. The promise of 1-dimensional materials for energy conversion is further evident in the superior crystalline quality and high surface areas of the $(Ga_{1-x}Zn_x)(N_{1-x}O_x)$ nanotubes. As research continues along these direction we move ever closer toward implementation of nanowires and nanotubes for clean, renewable, and more efficient energy use.

I dedicate this dissertation to my horse, Mr. Elegant.

Table of Contents

Acknowledgements

I would first, and foremost like to thank may advisor, Professor Peidong Yang, for giving me the opportunity to work in his group during the past five and half years. His hard work and dedication are inspiring and I owe much of my success as a scientist to his guidance and support.

I must also thank the numerous Yang group members who I've worked with over the years. Considering the enormous amount of time spent in lab, I was extremely lucky to have been able to spend that time with such smart, hardworking, helpful, and fun people. I am especially thankful of Josh Goldberger and Allon Hochbaum who served as my mentors when I first arrived at Berkeley. I thoroughly enjoyed working with Josh, Allon, Wenjie Liang, Oded Rabin, Sean Andrews, and Michael Moore on the various thermoelectric projects contained in this thesis. The hard work of Catherine Nguyen and Michelle Natera Comte were instrumental to the photoelectrochemical water splitting project and Catherine was especially helpful in keeping me motivated along the way. Thank you to Candace Chan, Sylvia Lo, and Harun Tueysuez who comprise the rest of the GC water splitting crew. It was a tough and frustrating project, but somehow they made it fun. I must also thank Lori Greene, Marty Mulvihill, Ben Yuhas, Erik Garnett, Yunjeong Hwang, Dan Gargas, Tev Kuykendall, Sean Andrews, Michael Moore, Chris Hahn, Ruoxue Yan, Frank Tsung, Eugenia Tomil Molares, and Anna Goldstein who have been great friends over the years. The Yang group has been my second family for a long time now and I will truly miss everyone when I leave.

In addition to my friends and colleagues in the Yang group, I must thank my other chemistry friends, George Holinga, Derek Butcher, and David Okawa, who have been enormously supportive and provided a lot of fun and joy over the years. I don't think I would've survived without them.

Finally, thank you to my family for being there for me for so many years. I really appreciate all their love, sacrifice, and support that have enabled me to attain this degree. And, I most certainly must thank my boyfriend, Will Hudson, who has had to put up with a lot of stress and crazy times as a result of this Ph.D. I could not have done it without him.

Chapter 1:
Introduction

1.1 – Semiconductor Nanowires and Nanotubes

Over the last decade there has been an exponential increase in research reports on semiconductor nanowires. In 2009 there were close to 6000 publications up from just a few hundred in 2000[1]. The intense interest into nanowires and nanotubes is related to their unique properties and the vast array of applications that follow. Compared to bulk materials, one-dimensional (1-D) semiconductor nanomaterials possess several fundamental differences related to the similarities between the dimensions of the nanomaterials and the characteristic length scales of several physical phenomena, such as the Bohr exciton radius and the electron and phonon mean free paths.

A more obvious advantage is the vast increase in surface area attained in nanoscale versus bulk materials. This high surface area is interesting for a variety of applications requiring a junction for charge separation or recombination, such as in p-n junction solar cells, photoelectrochemical cells, and light emitting diodes (LEDs). With increasing surface area there is also an increase in catalytic reaction sites, requiring significantly less material to achieve the same output.

When the diameter of the nanowire is smaller than the semiconductor's Bohr exciton radius, charges are restricted within two dimensions, resulting in quantum confinement. Quantum confinement alters the electronic density of states which change depending on the dimensionality of the nanostructure (Figure 1[2]). In quantum dots, charges are confined in all 3 dimensions, resulting in discrete energy levels that closely resemble those of single atoms. In quantum confined structures, the bandgap of the semiconductor can be tuned by simply changing the dimensions. For example, in CdSe quantum dots, a change in diameter from 20 to 2 nm results in a change in bandgap from 1.7 to 2.4 eV[3]. This property is especially attractive for solar applications where broadband absorption is desirable. A local change in the density of states can also be used to increase the Seebeck coefficient in thermoelectric materials, which will be discussed in greater detail later in this chapter.

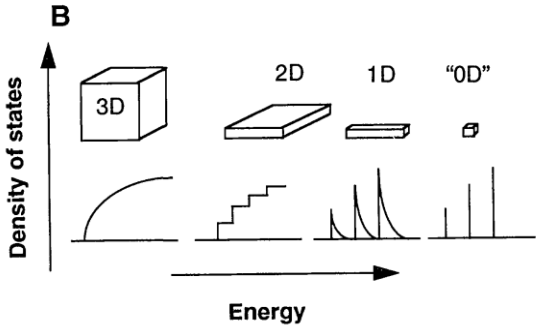

Figure 1 – Changes in the Density of States with quantum confinement: The density of states vs. energy for 3D, 2D, 1D, and "0D" systems. This figure was adopted from reference 2.

Electrical and thermal transport are also of particular interest in semiconductor nanomaterials. The discrepancy in the length scales of the electron and phonon mean free paths make it possible to scatter phonons on the surface of nanowires while electrons conduct freely. In addition, the single, un-restricted dimension present in nanowires and nanotubes facilitates better charge conduction compared to the highly resistive charge hopping that must occur to achieve conduction within nanoparticle films.

1.2 – Synthesis of Semiconductor Nanowires and Nanotubes

Over the years, numerous methods have been developed for the synthesis of 1-D semiconductor nanomaterials[4,5]. The bottom-up synthesis of semiconductor nanowires and nanotubes can produce high-quality, single-crystalline materials with extremely low defect densities. Single-crystal nanowires can also be grown on a variety of lattice-mismatched substrates without the formation of defects which are prevalent in bulk materials grown on the same substrates[1,6]. To achieve 1-D growth, a template, catalyst particle, or some other structure directing agent or force must be used to restrict lateral growth, as will be discussed in the following sections.

1.2.a – Vapor-Phase Synthesis

One popular approach for the synthesis of nanowires is chemical vapor transport, in which precursors are vaporized at high temperature and transported to a cooler region where they condense and crystallize. Nanowires can be synthesized by this method via a vapor-liquid-solid (VLS) mechanism. The VLS mechanism was first reported by Wagner and Ellis in 1964[7]. In the VLS mechanism, metal nanoparticle catalysts are used to restrict the dimensions of crystallization. During the synthesis the metal nanoparticles melt and precursor vapors begin to alloy with the metal. As the precursors reach the super-saturation point, a nucleation event generates a crystal seed. Since the precipitation of the crystalline material occurs at the interface with the metal nanoparticle, crystal growth continues on top of the initial seed within the lateral dimensions defined by the metal catalyst. Thus, the size of the metal nanoparticle controls the dimensions of the nanowires. When an epitaxial substrate is used, vertically oriented nanowire arrays may be generated. Si[8], ZnO[9], GaN[10], PbSe[11], CdS[12], and a variety of other materials can be grown by this mechanism[4].

Vapor-phase syntheses can also achieve 1-D growth in conjunction with a template approach[13]. This often involves the use of a nanoporous membrane, such as alumina, or a carbon nanotube template, onto which the desired semiconductor is deposited[14-18]. After the nanowires have been generated within the template, the template can be removed, leaving behind a free-standing array. One down-side of this approach is that the resultant nanowire arrays are often polycrystalline making them less desirable for those applications requiring good electrical conductivity. However, other templating procedures can be used to give high-

quality materials. For example, an epitaxial casting approach, wherein the template and casted material have a very close lattice match, can be used to generate single crystalline nanostructures. One notable example is the synthesis of GaN nanotubes using ZnO nanowire templates[19].

1.2.b – Solution-phase Synthesis

Solution-phase syntheses are desirable for nanomaterials production because they are more readily scaled and more favorable for industrial processes. In many colloidal syntheses, the nanowire shape is directed by stabilizers that attach to specific facets of the growing crystal, limiting the growth in some directions and allowing it to proceed in others[4,20,21]. In the case of CdTe[22], PbSe[23,24] and ZnO[25], nanowire growth can proceed by oriented attachment of nanoparticles. The oriented attachment is driven by dipoles within each nanocrystal, directing attachment along specific crystallographic directions. A solid-liquid-solid mechanism, which is the solution-phase cousin of the VLS mechanism, can also be used to direct 1-D growth in solution[26-28].

1.3 – Energy Conversion

The increasing environmental concerns associated with fossil fuel-based energy production have induced a wave of scientific research into affordable alternative energy sources that are both clean and renewable[29]. Semiconductors are currently being developed for a wide variety of energy conversion and storage applications, including photovoltaics, photoelectrochemical cells, thermoelectrics, and batteries. The unique properties of semiconductor nanowires and nanotubes are especially relevant for many of these applications and are currently the focus of intense research efforts. Thermoelectric power generation and photoelectrochemical water splitting will be discussed in detail below.

1.3.a – Thermoelectric Power Generation

While efforts into green power generation continue in a variety of exciting and promising directions, one avenue that has caught the attention of the scientific community over the past few years is thermoelectrics, wherein electrical power is generated through the scavenging of waste heat. According to the U.S. Energy Information Administration, over 60% of the energy we produce today is wasted as heat. If even some percentage of this heat could be converted back into useable energy via thermoelectrics, a significant increase in efficiency and a significant reduction in CO_2 emissions could be achieved. Currently, thermoelectric technologies are only used in niche applications due to their low efficiencies. One promising route to increase the efficiency is through the use of materials containing nanometer-sized

structural and compositional features which can exhibit enhanced thermoelectric performance due to the decoupling of certain electrical and thermal properties.

1.3.a.i – Thermoelectric Basics

Thermoelectric power generation is based on the Seebeck effect, defined as the change in voltage across a temperature gradient (S = dV/dT). Typical thermoelectric modules are composed of pairs of p-doped and n-doped semiconductors, configured such that they are connected electrically in series, but thermally in parallel (Figure 2[30]). When placed in a temperature gradient, the majority carriers move from the hot side to the cold side, generating a current in the circuit. Compared with other technologies, thermoelectric devices offer distinct advantages: they have no toxic emissions, no moving parts, and have a long lifetime of reliable operation. Efficient thermal to electrical power conversion requires low thermal conductivity to sustain a good temperature gradient and high charge carrier mobility to generate electrical power. Unfortunately, current thermoelectric materials have found limited commercial application due to their low efficiency.

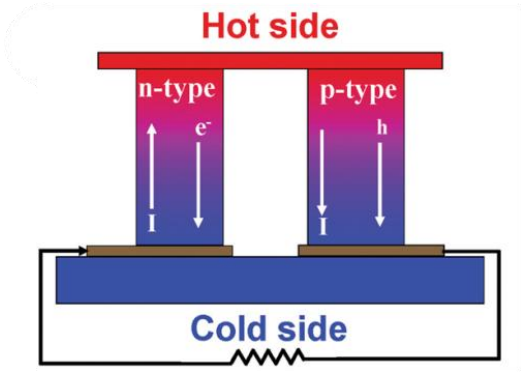

Figure 2 – Thermoelectric Power Generation: Typical p-n module for thermoelectric power generation. Figure was adopted from ref 30.

The efficiency of a thermoelectric device is related to the material-dependent figure of merit, $ZT=S^2\sigma T/k$, where S, σ, T, and k represent the Seebeck coefficient, electrical conductivity, absolute temperature, and thermal conductivity, respectively. Despite decades of scientific study, material engineering directed at maximizing ZT has been complicated by the interdependencies of the previously mentioned parameters, limiting the efficiency (Figure 3)[31]. Specifically, the Seebeck coefficient's inverse dependence on carrier concentration is at odds with the electrical conductivity's direct

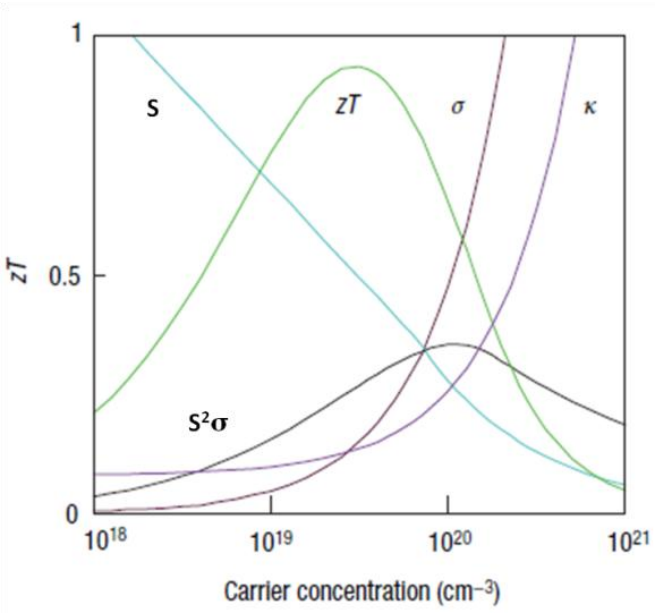

Figure 3 – Interdependence of the Thermoelectric Parameters: Plot showing the dependence of S, σ, k, and ZT on the material's carrier concentration. The maximum in ZT occurs at carrier concentrations around 10^{19}. This figure was adopted from reference 31.

dependence. An additional problem is that electrons carry both charge and heat, causing a synchronous increase in the electrical and thermal conductivities with carrier concentration. The interplay of these parameters has limited the *Z*T of bulk materials to ~1 at 300 K. For a solid state thermoelectric module to compete on the commercial market, a *Z*T of 3 or greater is considered necessary[32].

1.3.a.ii – Nanomaterials for Thermoelectrics

Theoretical studies pioneered by Hicks and Dresselhaus predict that it is possible to increase *Z*T by using low dimensional materials, for example, nanowires[33]. The advantages offered by low-dimensional structures include the enhancement of the density of states near the Fermi level (leading to an increase in the Seebeck coefficient), and increased boundary scattering of phonons (leading to a decrease in thermal conductivity)[34-38]. The positive effects of low-dimensionality on *ZT* have already been demonstrated through several theoretical[38-41] and experimental[42-46] investigations. Harman et al. achieved an especially high *ZT* of 2.0 at 300 K with PbSeTe/PbTe quantum dot superlattices[47].

Seebeck enhancements have been observed in a few structures as a result of the band structure changes introduced by quantum confinement. PbTe is a promising material for this enhancement since its bohr exciton radius is 46 nm, allowing quantum confinement to be achieved in relatively large structures. In 2008 Tai et al. measured a Seebeck coefficient of 628 $\mu V \cdot K^{-1}$ in 30 nm single-crystalline PbTe nanowires, which represents a 37% increase over the state of the art bulk PbTe[48]. Another notable example in which band structure changes lead to an increase in the Seebeck coefficient is that of bulk PbTe doped with thallium[37]. The Tl doping introduced additional energy levels, creating a local increase in the density of states, leading to a *Z*T of 1.5 at 773 K, which is double that of the best convention p-type PbTe alloy material. The *Z*T of the Tl-doped PbTe is expected to increase even further if nanostructuring is introduced to promote reductions in the thermal conductivity.

A variety of nanostructured systems have shown significant reductions in thermal conductivity compared to their bulk counter parts. The thermal conductivity of a material (*k*) is equal to $1/3C\nu\ell$, where *C* is the heat capacity, ν is the group velocity, and ℓ is the phonon mean free path. Decreases in the phonon mean free path should lead to subsequent decreases in the thermal conductivity. The phonon mean free path can be reduced by introducing scattering boundaries, such as crystal domain boundaries, impurity atoms, and additional surfaces. In nanomaterials, the phonon mean free path is limited by the size of the material since phonons are easily scattered at the semiconductor/air interface. Due to the large discrepancies in electron and phonon scattering lengths, electrons can pass though these materials oblivious to the additional interfaces while phonon propagation is retarded. By changing the diameter of the nanowire the thermal conductivity can be tailored. This has been shown by both the Yang and Heath groups in Si nanowires[45,46,49]. In Si nanowires with rough surfaces, additional decreases in thermal conductivity were achieved, with lattice contributions to the thermal conductivity approaching that of amorphous Si[45].

Semiconductor nanowires with superlattice structures are also promising for thermoelectrics[38]. Depending on the sizes of the superlattice features, the nanowire can resemble chains of quantum dots in which the density of states can be tailored to give enhanced Seebeck coefficients, and the boundaries between the quantum dots can act to reduce the thermal conductivity. In Si/SiGe superlattice nanowires, Li et al. demonstrated a 5-fold reduction in thermal conductivity compared to pure Si nanowires of comparable diameters[50]. This significant reduction was attributed to both interface scattering at the superlattice blocks as well as alloy scattering in the SiGe segments.

1.3.b – Photoelectrochemical Water Splitting

A possible alternative to our current hydrocarbon-based economy is one based on hydrogen. The appeal of H_2 stems from its high energy density (140 kJ/gram) and clean emissions ($H_2 + O_2 \rightarrow H_2O$ + electricity)[6]. However, there are several issues that need to be addressed, including production, transportation, storage, and use, before a H_2 economy can be realized. Currently H_2 is produced through steam reformation of natural gas. Unfortunately this method also generates a large amount of CO_2. One method that can be used to produce H_2 in a clean and renewable manner is photoelectrochemical water splitting. Unfortunately, like the thermoelectric materials discussed in the previous section, photoelectrochemical water splitting suffers from low efficiency. However, the high surface area and other unique properties of nanostructured materials can enhance the efficiency of H_2 production in photoelectrochemical systems.

1.3.b.i –Photoelectrochemical Water Splitting Basics

H_2 generation by water splitting is an uphill process (ΔG = 237.2 kJ/mol, E°= 1.23 V vs. Normal Hydrogen Electrode (NHE)) requiring 1.23 V to proceed[6]. This can be accomplished using two Pt electrodes to catalyze the oxidation and reduction reactions, and an electricity source to generate the required voltage. However, photoelectrochemical water splitting, in addition to being a clean and renewable source of H_2, is a more direct and potentially cheaper method compared to traditional electrolysis.

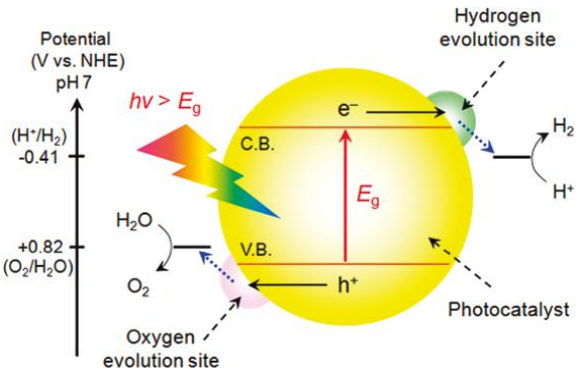

Figure 4 – Schematic showing overall PEC water splitting: This figure was adopted from ref 51.

Photoelectrochemical (PEC) water splitting occurs through a 3-step process (Figure 4[51]). First, a photon is absorbed by the semiconductor photocatalyst and an electron-hole pair is generated. This electron-hole pair is separated and the electrons and holes travel to the surface of the photocatalyst. Finally, the electrons and

holes reduce and oxidize chemical species adsorbed on the surface of the semiconductor. In an acidic media the overall reaction and two half reactions are as follows.

$$2H_2O + 4h\nu \rightarrow 2H_2 + O_2$$

$$2H_2O + 4h^+ \rightarrow 4H^+ + O_2$$
$$2H^+ + 2e^- \rightarrow H_2$$

To drive the water splitting reaction, the bandgap of the semiconductor must be at least 1.23 eV. However, some amount of overpotential is required to promote water oxidation and H^+ reduction, which raises the bandgap requirement to closer to 2.0 eV[52]. These overpotentials can be reduced somewhat by the addition of appropriate cocatalysts, such as Pt and RuO_2, but 2.0 eV remains a good benchmark for the photocatalyst bandgap. The importance of cocatalysts is highlighted by the vast number of systems that cannot split water in their absence.

To separate the electron-hole pairs, PEC water splitting takes advantage of the interfacial electric field generated by the semiconductor-electrolyte junction. When a semiconductor is placed in an electrolyte, charge will flow between the semiconductor and electrolyte until equilibrium is established (Figure 5a,b[52]). In the case of an n-type semiconductor, electrons pass from the semiconductor into the electrolyte. This creates a region of positively charged, uncompensated dopant atoms within the semiconductor, called the depletion region, and a much smaller negatively charged region within the electrolyte, called the Helmholtz layer. As a result of the electric field generated by these two regions, the bands bend upward at the surface in an n-type semiconductor, sweeping holes towards the surface and into the electrolyte. The opposite is true of a p-type semiconductor, in which the bands bend downward and electrons are swept to the surface. This electric field can effectively separate photogenerated electron-hole pairs. Thus, it is important that the electron-hole pairs

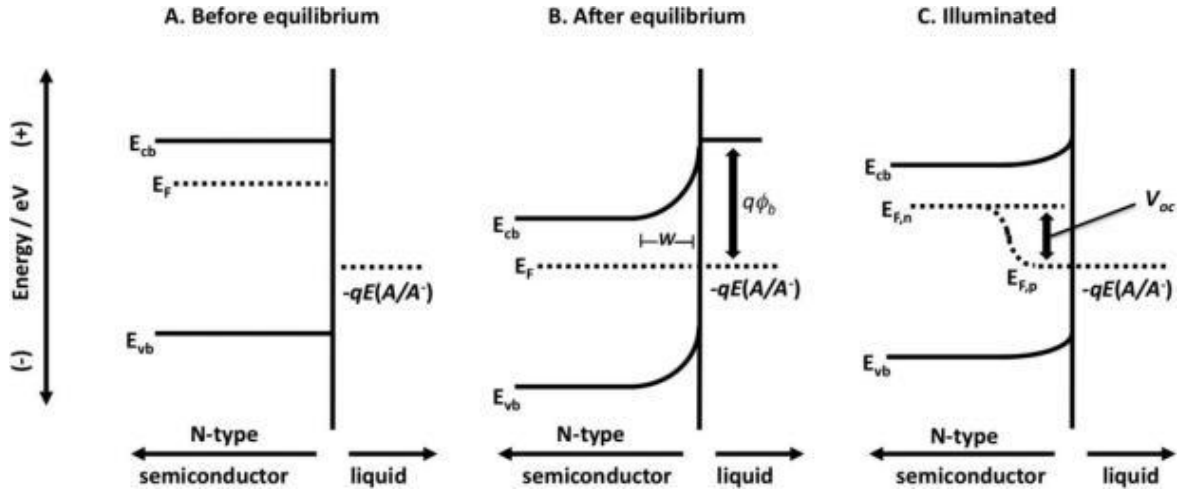

Figure 5 – Band energetics of an n-type semiconductor/electrolyte junction: Band energetics (a) before equilibrium, (b) after equilibrium, and (c) under illumination. This figure was adopted from ref 52.

be able to migrate to the surface without recombining.

In traditional PEC cells, a photocathode or photoanode is electrically connected to a counter electrode, often Pt, which catalyzes the other half reaction. The benefits of this system include the ability to apply an external bias to facilitate water splitting. However, it's also possible to use a particulate photocatalyst on which both the oxidation and reduction reactions are performed. In this case, at least one cocatalyst is generally used to locally alter the electric field at the surface of the semiconductor, allowing either electrons (in n-type semiconductors) or holes (in p-type semiconductors) to move towards the surface to participate in the water splitting.

Currently, PEC water splitting is extremely inefficient. Most of the difficulties are a result of the strict material demands that must be met in order to spit water. To perform overall water splitting on a single material under visible light, the semiconductor must a) have a bandgap around 2.0 eV, b) straddle the H^+/H_2 and H_2O/O_2 reduction and oxidation potentials, c) be stable under water splitting conditions, and d) be able to efficiently separate photogenerated charges and move them to the surface. There are several oxides, most notably TiO_2[53], that have the proper band positions, stability, and a high quantum efficiency, but their UV band gaps preclude them from reaching a high efficiency under sunlight (Figure 6 [54]). Several other materials with smaller bandgaps, such as CdS meet all the requirements except the stability criterion. In many of these smaller bandgap materials, oxidation of the semiconductor is more favorable than the oxidation of water, leading to a degradation of the photocatalyst over time. Many more materials do not straddle the oxidation and reduction potentials However, these materials are interesting for Z-scheme water splitting whereby two smaller band gap materials with different band alignments are used separately for the two half reactions. While the Z-scheme allows a wider range of materials to be used for water splitting, it necessitates some degree of device fabrication or the addition of redox couples. These materials may also be used in a PEC cell in which a photoanode or photocathode is connected to a counter electrode (usually Pt) such that a bias can be applied to shift the band to the appropriate condition for water splitting. However, the application of a bias reduces the efficiency of the H_2 production. It would be especially interesting to find a single material that could meet all the aforementioned criteria.

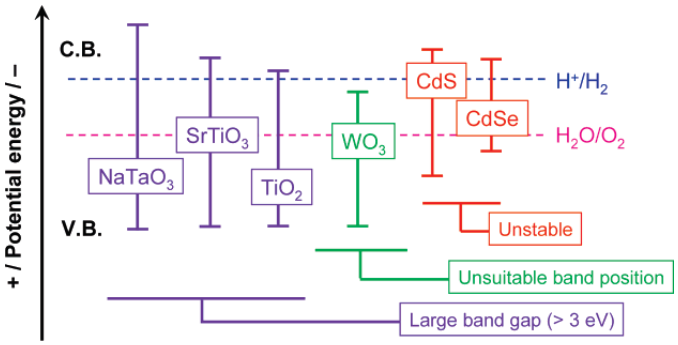

Figure 6 – Potential photocatalysts for PEC water splitting: Figure adopted from ref 54.

Single photocatalyst materials with appropriate cocatalysts have been developed that can effect overall water splitting[55]. However, the efficiency remains painfully low. The solar to hydrogen conversion efficiencies of a PEC cell can be calculated based on the following equation[56]

$$\eta = I \frac{1.23 - V_{bias}}{J_{light} \times A}$$

Where I is the photocurrent, V_{bias} is the applied external bias, J_{light} is the light irradiance and A is the area irradiated. For spontaneous water splitting, V_{bias} should be zero. The efficiency can also be calculated by monitoring the H_2 and O_2 generation from a particulate photocatalyst.

1.3.b.ii – Nanomaterials for Photoelectrochemical Water Splitting

One of the most promising methods for enhancing the efficiency of PEC water splitting is the use of nanostructured materials[6]. The potential benefits include increased surface area and smaller diffusion lengths for photogenerated charges. Plus, the synthesis of nanomaterials, as discussed earlier, generates single-crystalline, highly defect-free crystals wherein there is less recombination. The nanoscale features can also act as anti-reflection coatings facilitating increased absorption compared to similar bulk materials. In addition, when quantum confinement is introduced, it's possible to tune the bandgaps and band positions of the photocatalysts.

Since the oxidation and reduction reactions occur on the surfaces of the photocatalyst/cocatalyst system in PEC water splitting, it's beneficial to have a system with high surface area. Basically, the more surface you have, the more potential reaction sites that exist. In addition, since the surface to volume ratio is very high in nanomaterials, a larger percentage of the semiconductor will be affected by the interfacial electric field, promoting better charge separation and reduced recombination. In line with this, in nanomaterials, the distance that photogenerated charges must travel before reaching the surface is significantly reduced compared to the bulk, facilitating less recombination and again higher efficiencies. The important figure here is the minority carrier diffusion length. In a nanowire, a diameter of half the minority diffusion length should allow all photogenerated charges to reach the surface before recombining. This was shown recently in Si wire arrays by Nate Lewis's group. In fact, since the hole diffusion length in their VLS-synthesized Si wires was so large (~1 μm), the wires could be made on the microscale[57]. However, in less pure Si, which is significantly cheaper but possesses much shorter carrier diffusion lengths, nanoscale dimensions are effective in preventing recombination[58]. In many cases it is impossible to decouple these effects. A wide range of nanostructured systems, including TiO_2[53], CdS[59], WO_2[60], and Fe_2O_3[61] have shown enhancements in PEC water splitting efficiency compared to bulk.

Besides nanowires, nanotubes are another promising geometry. They offer additional surface area but overall, less material for light absorption than nanowires[62-65]. Thus, for nanotube materials, there exists some ideal tube wall thickness and tube diameter to achieve the optimal efficiency[62]. This is also true of nanowire diameters, which as discussed previously, are generally believed to give a maximum efficiency at twice the carrier diffusion length.

In PEC cells, it's been shown that oriented arrays of nanowires can scatter incident light, enhancing light absorption compared to a flat surface. In effect, the nanowire arrays function as an antireflection coating for their own absorption. This was shown recently in a Si/TiO_2-core/shell nanowire array[66]. In this case, the nanowire array showed a 2.5 times improvement

in photocurrent compared to the bulk material, which was attributed to both the increase in surface area and the low reflectance of the nanowire array. Also, compared to nanoparticles, nanowires provide a direct route for electrical transport to the back contact giving higher photocurrents and higher efficiencies. This has been shown for ZnO dye-sensitized solar cells, which are also PEC cells[67].

In addition, quantum confinement can push materials will unfavorable bandgaps or band positions to the point that they can participate in PEC water splitting. In photosensitized systems in which additional semiconductors are used for light absorption, quantum confinement can be used to achieve different wavelengths of absorption[68-72]. In TiO_2 nanorods decorated with CdS photosensitizers, an efficiency of 4.15% under AM 1.5 was attained[71] and Kongkanand et al. used CdSe quantum dots of various sizes decorated on TiO_2 nanotubes to achieve broadband absorption with power conversion efficiencies of ~1%[69]. Quantum confinement can also be used to aid in charge separation. For example, in CdS rods with embedded CdSe seeds, quantum confinement was able to localize the holes within the CdSe seeds, while the electron wave function was delocalized and easily transferred to a Pt tip for H^+ reduction[59].

1.4 – Outlook

As a result of the explosion of research over the last decade, we now have a good understanding of the unique properties of semiconductor nanowires and nanotubes and how these properties can be applied for a variety of applications, notably energy conversion. As research continues in this field, many new fundamental discoveries are expected, hopefully one day leading to greener and more sustainable energy production and use.

1.5 – References

1. Yang, P.D., R.X. Yan, and M. Fardy, *Semiconductor Nanowire: What's Next?* Nano Letters, 2010. **10**(5): p. 1529-1536.
2. Alivisatos, A.P., *Semiconductor clusters, nanocrystals, and quantum dots.* Science, 1996. **271**(5251): p. 933-937.
3. Murray, C.B., D.J. Norris, and M.G. Bawendi, *Synthesis and Characterization of Nearly Monodisperse Cde (E = S, Se, Te) Semiconductor Nanocrystallites.* Journal of the American Chemical Society, 1993. **115**(19): p. 8706-8715.
4. Law, M., J. Goldberger, and P.D. Yang, *Semiconductor nanowires and nanotubes.* Annual Review of Materials Research, 2004. **34**: p. 83-122.
5. Xia, Y.N., et al., *One-dimensional nanostructures: Synthesis, characterization, and applications.* Advanced Materials, 2003. **15**(5): p. 353-389.
6. Li, Y. and J.Z. Zhang, *Hydrogen generation from photoelectrochemical water splitting based on nanomaterials.* Laser & Photonics Reviews, 2010. **4**(4): p. 517-528.

7. Wagner, R.S. and W.C. Ellis, *Vapor-Liquid-Solid Mechanism of Single Crystal Growth (New Method Growth Catalysis from Impurity Whisker Epitaxial + Large Crystals Si E).* Applied Physics Letters, 1964. **4**(5): p. 89-90.
8. Garnett, E.C., W.J. Liang, and P.D. Yang, *Growth and electrical characteristics of platinum-nanoparticle-catalyzed silicon nanowires.* Advanced Materials, 2007. **19**(19): p. 2946–2950.
9. Huang, M.H., et al., *Catalytic growth of zinc oxide nanowires by vapor transport.* Advanced Materials, 2001. **13**(2): p. 113-116.
10. Kuykendall, T., et al., *Crystallographic alignment of high-density gallium nitride nanowire arrays.* Nature Materials, 2004. **3**(8): p. 524-528.
11. Zhu, J., et al., *Formation of chiral branched nanowires by the Eshelby Twist.* Nature Nanotechnology, 2008. **3**(8): p. 477-481.
12. Wang, Y.W., et al., *Catalytic growth of large-scale single-crystal CdS nanowires by physical evaporation and their photoluminescence.* Chemistry of Materials, 2002. **14**(4): p. 1773-1777.
13. Huczko, A., *Template-based synthesis of nanomaterials.* Applied Physics a-Materials Science & Processing, 2000. **70**(4): p. 365-376.
14. Prieto, A.L., et al., *Electrodeposition of ordered Bi2Te3 nanowire arrays.* Journal of the American Chemical Society, 2001. **123**(29): p. 7160-7161.
15. Lombardi, I., et al., *Synthesis of high density, size-controlled Si nanowire arrays via porous anodic alumina mask.* Chemistry of Materials, 2006. **18**(4): p. 988-991.
16. Li, Y., et al., *Preparation of cadmium sulfide nanowire arrays in anodic aluminum oxide templates.* Chemistry of Materials, 1999. **11**(12): p. 3433–3435.
17. Klein, J.D., et al., *Electrochemical Fabrication of Cadmium Chalcogenide Microdiode Arrays.* Chemistry of Materials, 1993. **5**(7): p. 902-904.
18. Ajayan, P.M., et al., *Carbon Nanotubes as Removable Templates for Metal-Oxide Nanocomposites and Nanostructures.* Nature, 1995. **375**(6532): p. 564-567.
19. Goldberger, J., et al., *Single-crystal gallium nitride nanotubes.* Nature, 2003. **422**(6932): p. 599-602.
20. Greene, L.E., et al., *Solution-grown zinc oxide nanowires.* Inorganic Chemistry, 2006. **45**(19): p. 7535-7543.
21. Kang, C.C., et al., *Surfactant- and temperature-controlled CdS nanowire formation.* Small, 2007. **3**(11): p. 1882-1885.
22. Tang, Z.Y., N.A. Kotov, and M. Giersig, *Spontaneous organization of single CdTe nanoparticles into luminescent nanowires.* Science, 2002. **297**(5579): p. 237-240.
23. Cho, K.S., et al., *Designing PbSe nanowires and nanorings through oriented attachment of nanoparticles.* Journal of the American Chemical Society, 2005. **127**(19): p. 7140-7147.
24. Lu, W.G., et al., *Perfect orientation ordered in-situ one-dimensional self-assembly of Mn-doped PbSe nanocrystals.* Journal of the American Chemical Society, 2004. **126**(45): p. 14816-14821.
25. Pacholski, C., A. Kornowski, and H. Weller, *Self-assembly of ZnO: From nanodots, to nanorods.* Angewandte Chemie-International Edition, 2002. **41**(7): p. 1188–1191.

26. Heitsch, A.T., et al., *Solution-liquid-solid (SLS) growth of silicon nanowires.* Journal of the American Chemical Society, 2008. **130**(16): p. 5436-5437.
27. Fanfair, D.D. and B.A. Korgel, *Bismuth nanocrystal-seeded III-V semiconductor nanowire synthesis.* Crystal Growth & Design, 2005. **5**(5): p. 1971-1976.
28. Ouyang, L., et al., *Catalyst-assisted solution-liquid-solid synthesis of CdS/CdSe nanorod heterostructures.* Journal of the American Chemical Society, 2007. **129**(1): p. 133-138.
29. Hochbaum, A.I. and P. Yang, *Semiconductor nanowires for energy conversion.* Chemical Reviews, 2010. **110**(1): p. 527-546.
30. Minnich, A.J., et al., *Bulk nanostructured thermoelectric materials: current research and future prospects.* Energy & Environmental Science, 2009. **2**(5): p. 466-479.
31. Snyder, G.J. and E.S. Toberer, *Complex thermoelectric materials.* Nature Materials, 2008. **7**(2): p. 105-114.
32. Majumdar, A., *Thermoelectricity in semiconductor nanostructures.* Science, 2004. **303**(5659): p. 777-778.
33. Hicks, L.D. and M.S. Dresselhaus, *Thermoelectric figure of merit of a one-dimensional conductor.* Physical Review B, 1993. **47**(24): p. 16631-16643.
34. Donadio, D. and G. Galli, *Atomistic simulations of heat transport in silicon nanowires.* Physical Review Letters, 2009. **102**(19): p. 195901.
35. Lee, J.H., G.A. Galli, and J.C. Grossman, *Nanoporous Si as an efficient thermoelectric material.* Nano Letters, 2008. **8**(11): p. 3750-3754.
36. Martin, P., et al., *Impact of phonon-surface roughness scattering on thermal conductivity of thin Si nanowires.* Physical Review Letters, 2009. **102**(12): p. 125503.
37. Heremans, J.P., et al., *Enhancement of thermoelectric efficiency in PbTe by distortion of the electronic density of states.* Science, 2008. **321**(5888): p. 554-557.
38. Lin, Y.M. and M.S. Dresselhaus, *Thermoelectric properties of superlattice nanowires.* Physical Review B, 2003. **68**(7): p. 075304.
39. Hicks, L.D. and M.S. Dresselhaus, *Effect of Quantum-Well Structures on the Thermoelectric Figure of Merit.* Physical Review B, 1993. **47**(19): p. 12727-12731.
40. Dresselhaus, M.S., et al., *The promise of low-dimensional thermoelectric materials.* Microscale Thermophysical Engineering, 1999. **3**(2): p. 89-100.
41. Broido, D.A. and T.L. Reinecke, *Thermoelectric transport in quantum well superlattices.* Applied Physics Letters, 1997. **70**(21): p. 2834-2836.
42. Venkatasubramanian, R., et al., *Thin-film thermoelectric devices with high room-temperature figures of merit.* Nature, 2001. **413**(6856): p. 597-602.
43. Beyer, H., et al., *PbTe based superlattice structures with high thermoelectric efficiency.* Applied Physics Letters, 2002. **80**(7): p. 1216-1218.
44. Heremans, J.P., C.M. Thrush, and D.T. Morelli, *Thermopower enhancement in lead telluride nanostructures.* Physical Review B, 2004. **70**(11): p. 115334
45. Hochbaum, A.I., et al., *Enhanced thermoelectric performance of rough silicon nanowires.* Nature, 2008. **451**(7175): p. 163-167.
46. Boukai, A.I., et al., *Silicon nanowires as efficient thermoelectric materials.* Nature, 2008. **451**(7175): p. 168-171.

47. Harman, T.C., et al., *Quantum dot superlattice thermoelectric materials and devices.* Science, 2002. **297**(5590): p. 2229-2232.
48. Tai, G., B. Zhou, and W.L. Guo, *Structural characterization and thermoelectric transport properties of uniform single-crystalline lead telluride nanowires.* Journal of Physical Chemistry C, 2008. **112**(30): p. 11314-11318.
49. Li, D.Y., et al., *Thermal conductivity of individual silicon nanowires.* Applied Physics Letters, 2003. **83**(14): p. 2934-2936.
50. Li, D.Y., et al., *Thermal conductivity of Si/SiGe superlattice nanowires.* Applied Physics Letters, 2003. **83**(15): p. 3186-3188.
51. Maeda, K. and K. Domen, *Photocatalytic Water Splitting: Recent Progress and Future Challenges.* Journal of Physical Chemistry Letters, 2010. **1**(18): p. 2655-2661.
52. Walter, M.G., et al., *Solar Water Splitting Cells.* Chemical Reviews, 2010. **110**(11): p. 6446-6473.
53. Ni, M., et al., *A review and recent developments in photocatalytic water-splitting using TiO2 for hydrogen production.* Renewable & Sustainable Energy Reviews, 2007. **11**(3): p. 401-425.
54. Maeda, K. and K. Domen, *New non-oxide photocatalysts designed for overall water splitting under visible light.* Journal of Physical Chemistry C, 2007. **111**(22): p. 7851-7861.
55. Maeda, K., et al., *Photocatalyst releasing hydrogen from water - Enhancing catalytic performance holds promise for hydrogen production by water splitting in sunlight.* Nature, 2006. **440**(7082): p. 295-295.
56. Murphy, A.B., et al., *Efficiency of solar water splitting using semiconductor electrodes.* International Journal of Hydrogen Energy, 2006. **31**(14): p. 1999-2017.
57. Maiolo, J.R., et al., *High aspect ratio silicon wire array photoelectrochemical cells.* Journal of the American Chemical Society, 2007. **129**(41): p. 12346-12347.
58. A. Boukai, P.H., A. Katzenmeyer, G.M. Gallatin, A.A. Talin, P. Yang, *Efficiency Enhancement of Copper Contaminated Radial p-n Junction Solar Cells.* Chemical Physics Letters, 2010. DOI: 10.1016/j.cplett.2010.11.069
59. Amirav, L. and A.P. Alivisatos, *Photocatalytic Hydrogen Production with Tunable Nanorod Heterostructures.* Journal of Physical Chemistry Letters, 2010. **1**(7): p. 1051-1054.
60. Wolcott, A., et al., *Synthesis and characterization of ultrathin WO3 nanodisks utilizing long-chain poly(ethylene glycol).* Journal of Physical Chemistry B, 2006. **110**(50): p. 25288-25296.
61. Saremi-Yarahmadi, S., et al., *Nanostructured alpha-Fe2O3 Electrodes for Solar Driven Water Splitting: Effect of Doping Agents on Preparation and Performance.* Journal of Physical Chemistry C, 2009. **113**(12): p. 4768-4778.
62. Mor, G.K., et al., *Enhanced photocleavage of water using titania nanotube arrays.* Nano Letters, 2005. **5**(1): p. 191-195.
63. Mor, G.K., et al., *p-Type Cu-Ti-O Nanotube Arrays and Their Use in Self-Biased Heterojunction Photoelectrochemical Diodes for Hydrogen Generation (vol 8, pg 1906, 2008).* Nano Letters, 2008. **8**(10): p. 3555-3555.

64. Mohapatra, S.K., et al., *Design of a highly efficient photoelectrolytic cell for hydrogen generation by water splitting: Application of TiO(2-)xC(x) nanotubes as a photoanode and Pt/TiO2 nanotubes as a cathode.* Journal of Physical Chemistry C, 2007. **111**(24): p. 8677-8685.
65. Mor, G.K., et al., *Vertically oriented Ti-Fe-O nanotube array films: Toward a useful material architecture for solar spectrum water photoelectrolysis.* Nano Letters, 2007. **7**(8): p. 2356-2364.
66. Hwang, Y.J., A. Boukai, and P.D. Yang, *High Density n-Si/n-TiO2 Core/Shell Nanowire Arrays with Enhanced Photoactivity.* Nano Letters, 2009. **9**(1): p. 410-415.
67. Law, M., et al., *Nanowire dye-sensitized solar cells.* Nature Materials, 2005. **4**(6): p. 455-459.
68. Lee, Y.L., C.F. Chi, and S.Y. Liau, *CdS/CdSe Co-Sensitized TiO2 Photoelectrode for Efficient Hydrogen Generation in a Photoelectrochemical Cell.* Chemistry of Materials, 2010. **22**(3): p. 922-927.
69. Kongkanand, A., et al., *Quantum dot solar cells. Tuning photoresponse through size and shape control of CdSe-TiO2 architecture.* Journal of the American Chemical Society, 2008. **130**(12): p. 4007-4015.
70. Tak, Y., et al., *Solution-Based Synthesis of a CdS Nanoparticle/ZnO Nanowire Heterostructure Array.* Crystal Growth & Design, 2009. **9**(6): p. 2627-2632.
71. Sun, W.T., et al., *CdS quantum dots sensitized TiO2 nanotube-array photoelectrodes.* Journal of the American Chemical Society, 2008. **130**(4): p. 1124-1125.
72. Lin, C.J., et al., *Surface modification of highly ordered TiO2 nanotube arrays for efficient photoelectrocatalytic water splitting.* Applied Physics Letters, 2009. **94**(11): p. 113102.

Chapter 2:
Lead Chalcogenide (Pb*X*, *X* = S, Se, Te) Nanowires

2.1 – Introduction to Lead Chalcogenides

Lead chalcogenides refer to the group of materials containing Pb cations and either S, Se, or Te anions. All three of these compounds crystallize in the NaCl crystal structure which consists of two interpenetrating face centered cubic (fcc) lattices, one each for the cation and anion. The bandgaps of PbS, PbSe, and PbTe are 0.37, 0.27, and 0.29 eV, respectively[1]. While PbS has a direct bandgap, both PbSe and PbTe have indirect bandgaps, limiting their absorption coefficients. In PbS, PbSe, and PbTe, the bohr exciton radius is unusually large with values of 18, 46, and 46 nm, respectively[2]. This unique feature enables quantum confinement within relatively large nanocrystals. Multiple exciton generation (MEG) has also been demonstrated in PbSe nanocrystals, whereby several electron-hole pairs can be formed after the absorption of a single photon[3]. MEG is especially promising for solar cell applications since it can lead to quantum efficiencies (carriers/photons absorbed) of several hundred percent. Lead chalcogenides are also frequently used as thermoelectric materials due to their relatively high efficiencies[4].

2.2 – Thermoelectric Applications of Lead Chalcogenides

Bulk lead chalcogenides are some of the most efficient thermoelectric materials to date[4]. Their high efficiency is partially due to their low thermal conductivity, for example, 2.4 $W \cdot m^{-1} \cdot K^{-1}$ for PbTe at 300 K[5]. Dimensional reduction could further boost their thermoelectric properties. Recently, Wang et al.[6] showed that thermopower increased monotonically in PbSe quantum dot films with decreasing quantum dot size, and in 2002, Harman et al.[7] reported PbSeTe/PbTe quantum dot superlattices with $ZT \approx 2$. In addition, theoretical work by Hicks and Dresselhaus on PbSe/PbS and PbSe/PbTe superlattice nanowires with 5 nm diameters have predicted *Z*Ts of as high as 4 and 6 due to both phonon scattering and Seebeck enhancement[8]. Based on these predictions, it is feasible that large enhancements in the thermoelectric figure of merit could be obtained in lead chalcogenide nanowires.

2.3 – Synthesis of Lead Chalcogenide Nanowires

A variety of methods have been utilized to synthesize lead chalcogenide (Pb*X*, *X* = S, Se, Te) nanowires, including templating in mesoporous silica channels[9,10] and anodic alumina membranes[10,11], oriented attachment of nanoparticles[12], seeded solution synthesis[13], lithographically patterned electrodeposition[14], colloidal synthesis[15], and solvothermal[16,17], hydrothermal[18,19], and soft template routes[20]. A facile chemical vapor transport (CVT) synthesis of thin, high aspect ratio PbS nanowire arrays has also been reported[21]. This last method produces high-quality, single crystalline nanowires, highlighting CVT as a promising method for synthesis of Pb*X* nanowires as novel thermoelectric materials.

2.4 – Synthesis, Characterization, and Thermoelectric Properties of Pb*X* Nanowires grown by Chemical Vapor Transport (CVT)

CVT synthesis is a well-known method for the synthesis of nanowires. It has been used successfully for growth of nanowires by the vapor-liquid-sold (VLS) mechanism for a wide range of materials[22]. When considering a synthetic method to prepare Pb*X* nanowires with good crystallinity and low defect density, CVT is a promising approach. In the following sections the synthesis, structure, and thermoelectric properties of CVT-synthesized Pb*X* nanowires will be described.

2.4.a – Synthesis of Pb*X* Nanowires by CVT

PbS, PbSe, and PbTe nanowires were prepared by chemical vapor transport of Pb and chalcogen precursors inside a horizontal tube furnace. Alumina boats filled with $PbCl_2$ and the desired chalcogen were positioned in a quartz tube near the center of the furnace. Si (100) substrates were placed downstream from the precursors in the cooler region of the tube to collect the deposited products. In each synthesis, the furnace was heated to the reaction temperature for 10 minutes under a carrier gas flow of N_2, 5% H_2 balance N_2, Ar, or 10% H_2 balance Ar. The details for each synthesis are described below.

The experimental apparatus for all of the syntheses consisted of a quartz tube inside a Lindberg/Blue horizontal tube furnace (Figure 7). The furnace is constructed such that the hottest temperature exists directly at the center (thermocouple position) and the temperature falls off with distance from the center[23]. A typical synthesis for PbS nanowires is as follows: 0.80 g $PbCl_2$ (Alfa Aesar, 99%) and 0.33 g S powder (Alfa Aesar, 325 mesh, 99.5%) were loaded into separate alumina boats. The $PbCl_2$ boat was positioned directly in the middle of the furnace where the temperature could be strictly controlled. The S boat was placed 3 cm from the center on the upstream side. Single-crystalline Silicon (100) wafers were cut into substrates approximately 1×3 cm^2. All substrates were cleaned by sonication in isopropanol and dried

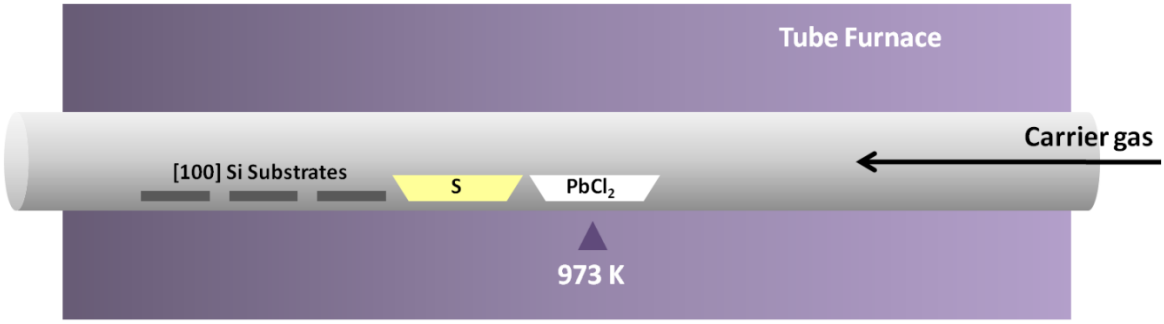

Figure 7 – Experimental Apparatus for CVT Synthesis of PbS Nanowires: Schematic showing the apparatus and setup for the synthesis of PbS nanowires.

under a N_2 stream. Several Si (100) substrates were then positioned on the downstream side of the tube, 5–16 cm from the center. Prior to deposition, the tube was purged with carrier gas for 30 min at room temperature to remove oxygen from the reaction environment. The tube was heated between 600–700°C for 10 min under 45–80 sccm of N_2, 5% H_2 balance N_2, Ar, or 10% H_2 balance Ar. After heating, the tube was allowed to cool to room temperature.

For the synthesis of PbSe and PbTe nanowires, the PbS synthesis procedure was used except for the following adjustments. To synthesize PbSe nanowires 0.57 g of $PbCl_2$ and 0.45 g of amorphous Se powder (Alfa Aesar, 325 mesh, 99.999%), were loaded into the tube with the Se boat 3.5 cm from the center on the upstream side. The reaction was carried out at 900–950°C under 5–60 sccm of carrier gas flow. For the synthesis of PbTe nanowires, 0.57 g $PbCl_2$ and 0.57 g Te powder (Alfa Aesar, 200 mesh, 99.5%) were inserted into the tube with the Te boat 4 cm upstream from the center. The tube was heated to 800–900°C under 5–125 sccm of carrier gas flow.

2.4.b – Structural Characterization of CVT-Synthesized Pb*X* Nanowires

X-ray diffraction (XRD) patterns were taken using a Bruker D-8 GADDS diffractometer with Co K_α irradiation. Patterns taken from the as-synthesized nanowire substrates (Figure 8) demonstrate the high quality, crystalline nature of the materials. Substrates chosen for XRD characterization were covered with nanowires over an area of 1–3 cm^2. The diffraction peaks in each pattern were indexed to the fcc crystal structure of pure PbS, PbSe, and PbTe, with calculated lattice constants of 5.943 Å, 6.116 Å, and 6.406 Å, respectively. These lattice constants correspond well to those of the bulk material, 5.94 Å (PbS), 6.12 Å (PbSe), and 6.50 Å (PbTe)[24]. The minor peaks in the PbTe pattern belong to hexagonal Te. This Te was likely deposited as particulates or thin film, but was not present on the nanowire surfaces, as confirmed by transmission electron microscopy imaging.

The morphologies of the Pb*X* nanowires were examined using both scanning electron microscopy (SEM) and transmission electron microscopy (TEM). The SEM and TEM analyses were performed using a JEOL JSM-6340F Field Emission SEM operating at 5 kV and a Philips CM

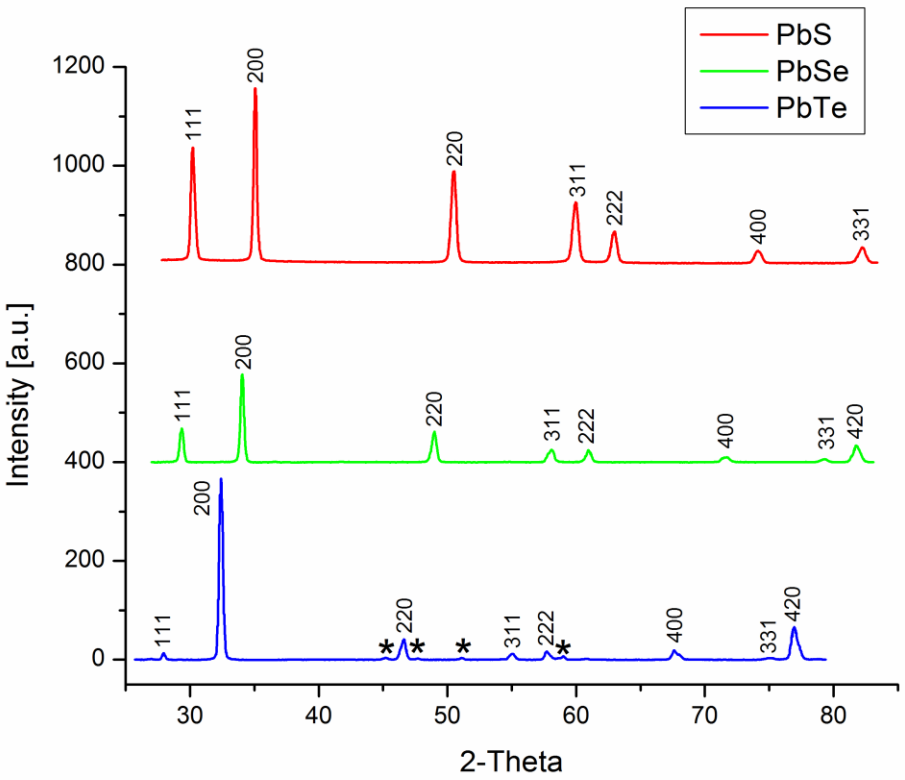

Figure 8 – XRD Patterns of CVT-synthesized Pb*X* Nanowires: XRD patterns taken from (a) Pbs, (b) PbSe, and (c) PbTe nanowire substrates (stars indicate Te peaks), which confirm their chemical composition and fcc structure.

200 FEG operating at 200 kV, respectively. Samples for TEM characterization were prepared by contact transfer onto 200 mesh carbon-coated copper grids.

The nanowires grown in this CVT synthesis have similar diameter and length distributions, independent of the material. The typical diameters and lengths of the nanowires are 40–100 nm and 10–70 µm for PbS (Figures 9a,b), 40–200 nm and 10–100 µm for PbSe (Figures 9c,d), and 100–200 nm and 40–100 µm for PbTe (Figures 9e,f). As shown in the SEM images in Figure 9, the nanowires in each array are aligned either parallel or perpendicular to one another and are arranged in two different types of arrays. The first type of array (Figure 9, top row) has been previously reported for PbS CVT nanowires and consists of a central cube with nanowires growing perpendicularly from each of the six faces[21]. In this case, Ge et al. proposed a homogeneous, epitaxial growth process in which defects on the surfaces of the cubes serve as nucleation sites for the nanowire growth. The second type of array is self supporting and does not contain a central cube (Figure 9, bottom row)[25]. The morphology of these arrays varies between a net of wires and a structure similar to that of the orthogonal arrays with cubes. It's likely that the nanowires grew by a self-catalyzed VLS mechanism using a Pb catalyst. Although Pb catalyst tips were not observed on most of the nanowires, they were observed on some larger nanowires. It's possible that the Pb catalysts were consumed by the

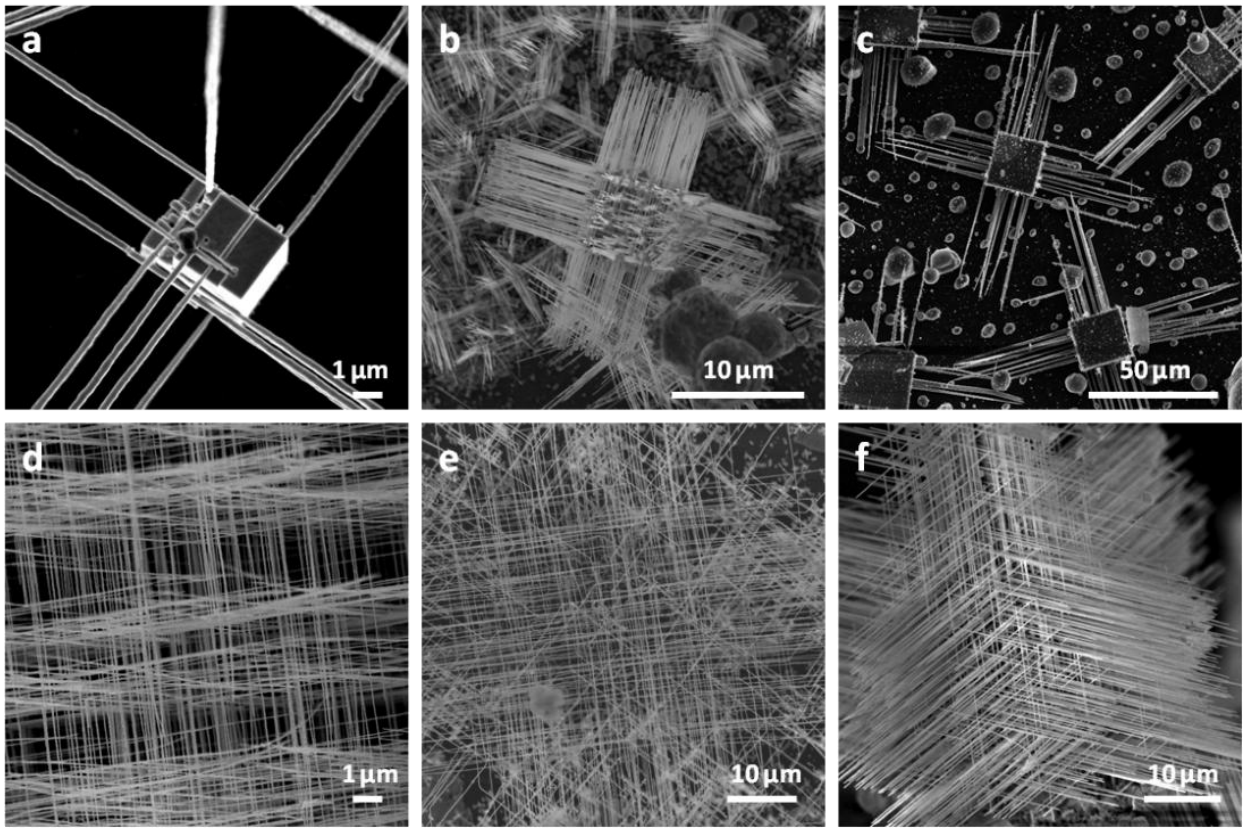

Figure 9 – SEM Characterization of CVT-Synthesized Pb*X* Nanowires: SEM images displaying central cube arrays (a,b,c) and self-supporting arrays (d,e,f) of PbS (a,d), PbSe (b,e), and PbTe (c,f) nanowires.

reaction or diffused along the nanowires during the synthesis. Interfacial dewetting and large differences in the interfacial thermal expansion can also cause the catalyst tips to pop off during cooling[22]. In the case of the nanowire arrays with central cubes, it is likely that the cubes grew in the early stages of the reaction and then became coated with Pb nanoparticles which acted as VLS catalysts for the growth of the Pb*X* nanowires. Self-catalyzed VLS nanowire growth is advantageous in that foreign catalyst metals can be eliminated from the reaction system, which avoids possible contamination and its subsequent effects on the nanowire quality. However, it is disadvantageous in that it is difficult to control the nanowire diameter since the catalyst particles are developed *in-situ.*

The selected area electron diffraction (SAED) patterns (Figures 10a–c, insets), taken from the [100] zone axis, suggest that the nanowires are single crystalline and grow along the <100> directions. No secondary or hexagonal phases were detected, thus confirming that the crystalline Te observed in the XRD pattern was not deposited on the nanowires. The single crystallinity and structural parameters were further verified by high-resolution transmission electron microscopy (HRTEM) images of the nanowires (Figures 10a–c). Elemental analysis was performed on the nanowires using a Phillips CM200 FEG equipped with an Oxford Energy Dispersive X-ray Spectroscopy (EDS) detector. The EDS spectra (Figures 10d–f) confirm the purity of the nanowires, with the Cu peaks arising from the copper grids used for TEM analysis. Cl peaks were also detected and likely result from surface impurities remaining from the $PbCl_2$

precursor. In addition to the aforementioned species, the EDS spectra show presence of both Si and O signals. As seen in the HRTEM images, the nanowires have 2–6 nm thick coatings of amorphous silica. This silica coating can be etched using a buffered hydrofluoric acid (BHF) solution. Several groups have previously reported amorphous silica coatings on CVT-synthesized PbS nanowires[21,25]. This silica most likely originates from etching of the silicon substrates and quartz reaction tube during the synthetic process[26].

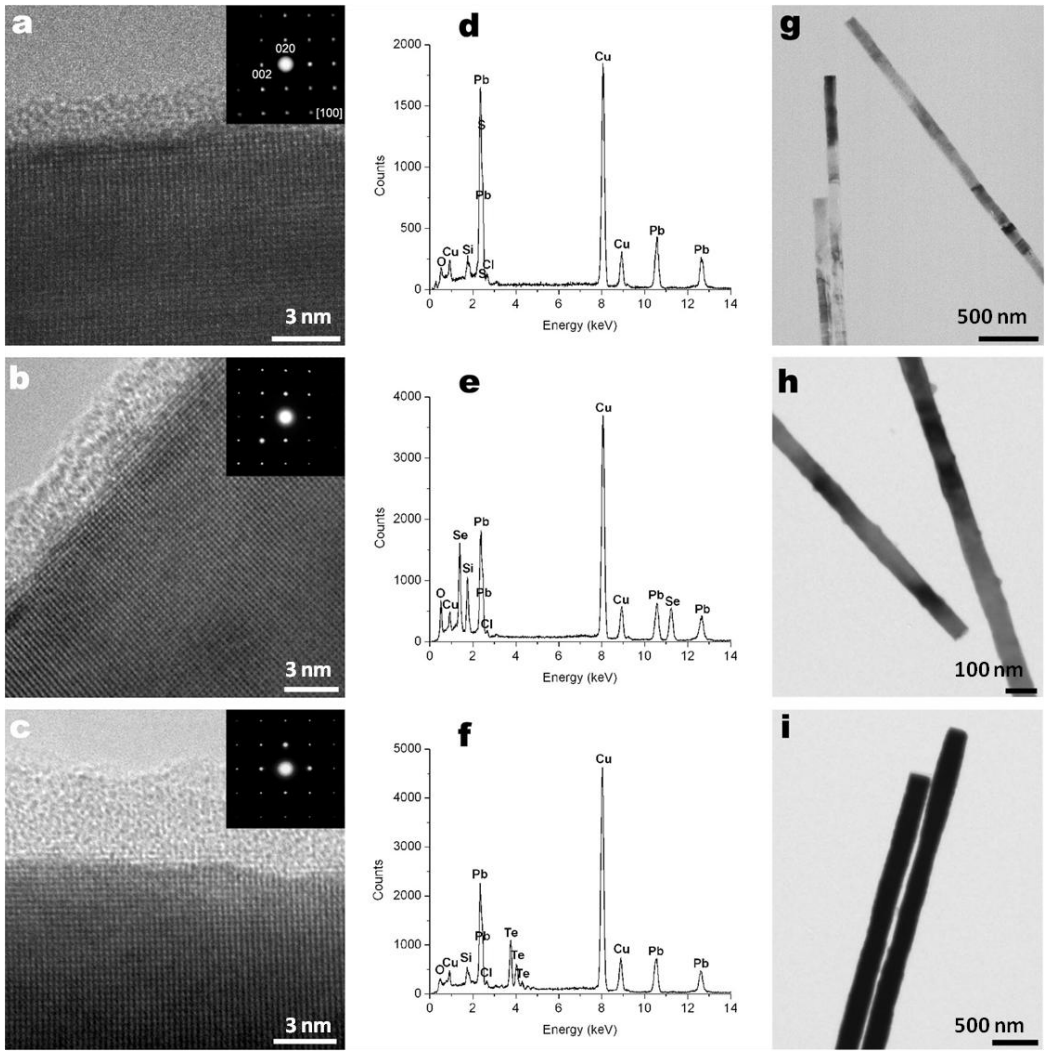

Figure 10 – TEM Characterization of CVT-synthesized Pb*X* Nanowires: HRTEM images of (a) PbS, (b) PbSe, and (c) PbTe nanowires showing their crystalline structure as well as the amorphous silica coatings. Insets are SAED patterns of each material taken from the [100] zone axis indicating that the growth direction of the nanowires is in the <100> directions. EDS spectra from (d) PbS, (e) PbSe, and (f) PbTe nanowires, confirming their purity. TEM images of (g) PbS, (h) PbSe, and (i) PbTe nanowires displaying typical diameters.

2.4.c - Thermoelectric Characterization of CVT-Synthesized Pb*X* Nanowires

Electronic properties of CVT-grown Pb*X* nanowires were measured using contacts patterned by electron-beam lithography[27]. Nanowires were sonicated into isopropanol, and the suspension was drop-cast onto substrates. The substrates consisted of prefabricated Au probe-pad electrodes on top of a degenerately p-doped Si wafer with 350 nm Si_3N_4 gate dielectric that was deposited using a low-pressure chemical vapor deposition Tystar furnace. The substrates were then soaked in 10:1 BHF to selectively remove the insulating silica coating on the outer surface of the nanowires. For the cases of PbS and PbTe, little to no degradation or measurable contraction of the nanowire diameter was observed in HRTEM after the samples were treated with BHF. However, the outer amorphous silica shell was completely removed. The PbSe nanowires, on the other hand, were completely etched away after 20–30 seconds of BHF exposure. As a result, PbSe devices had to be fabricated using an alternative procedure (described below). After spinning a PMMA layer onto the substrates, EBL contacts were generated using a JEOL series 6400 SEM and Nanometer Pattern Generation System (NPGS). The exposed PMMA regions were developed with a methyl isobutyl ketone:isopropanol (1:3) mixture and the substrates were washed for 5 seconds in 10:1 BHF and rinsed for 12 seconds in deionized water. The devices were cleaned using oxygen plasma for 60 s at 50 W. 5/3/200/50 nm Pd/Ti/Pd/Au were deposited sequentially onto the exposed substrate by electron-beam evaporation. For the PbSe nanowires, a FEI Strata Dual Beam Focused Ion Beam (FIB) was used to deposit Pt contacts on the thermal measurement devices.

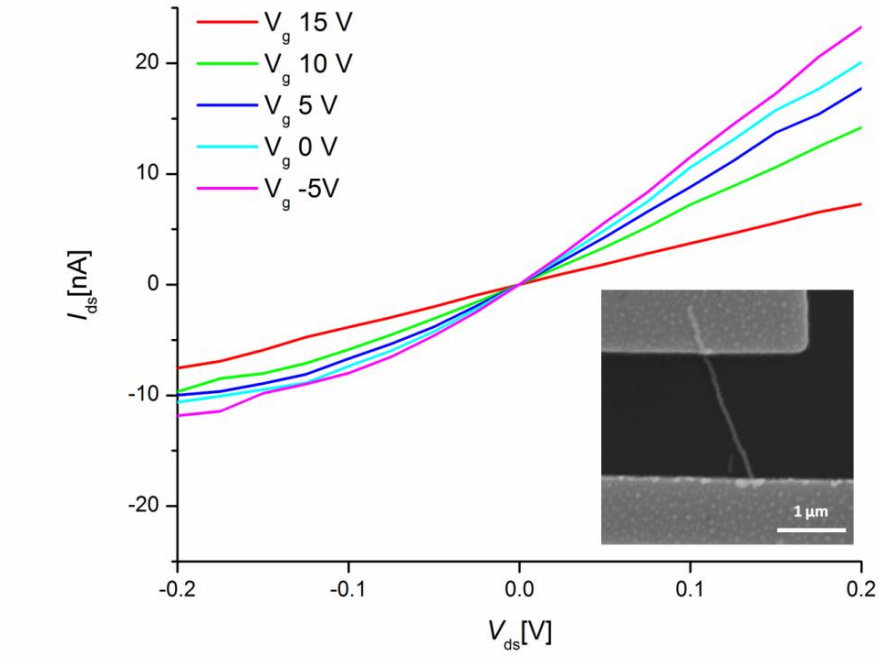

Figure 11 – Electrical Properties of CVT-Synthesized PbS Nanowires: *I-V* Characteristics of a 63 nm PbS nanowire. Inset is an SEM image of the electrical device.

Figure 11 shows the *I–V* characteristics for a 63 nm diameter PbS nanowire field-effect transistor (FET) device under different gate voltages. The device is p-type with a resistivity of 1.7 Ω·cm. The calculated carrier concentration is 3.7×10^{18} cm^{-3} and the mobility is 1.0 $cm^2 \cdot V^{-1} \cdot s^{-1}$, as determined from the transconductance plot of the data. *I–V* data was also taken from an 83 nm PbTe nanowire. A roughly linear *I–V* curve was obtained, which is indicative of nearly ohmic contacts. Unlike the PbS devices, the PbTe device only weakly gates, due to its higher carrier concentration of 8.4×10^{19} cm^{-3}. This device is p-type and has a resistivity of 0.1 Ω·cm and a mobility of 0.71 $cm^2 \cdot V^{-1} \cdot s^{-1}$. Several PbSe nanowire devices were measured, and with an average wire diameter of 95 nm, the wires have an average resistivity of 0.15 Ω·cm, though some samples exhibit resistivities below 1×10^{-2} Ω·cm. Mobility and carrier concentration values for the PbS and PbTe devices were determined using the standard back-gate nanowire transistor formulas derived from the cylinder-on-plate electrostatic model[28]. This model neglects the influence of contact resistance, surface trap states, and poor gating efficiency across the nanowire width[29], thus causing these values to be a lower estimate of the true semiconductor mobility. Moreover, it is conceivable that higher mobility values can be achieved by carrier concentration reduction as well as surface passivation.

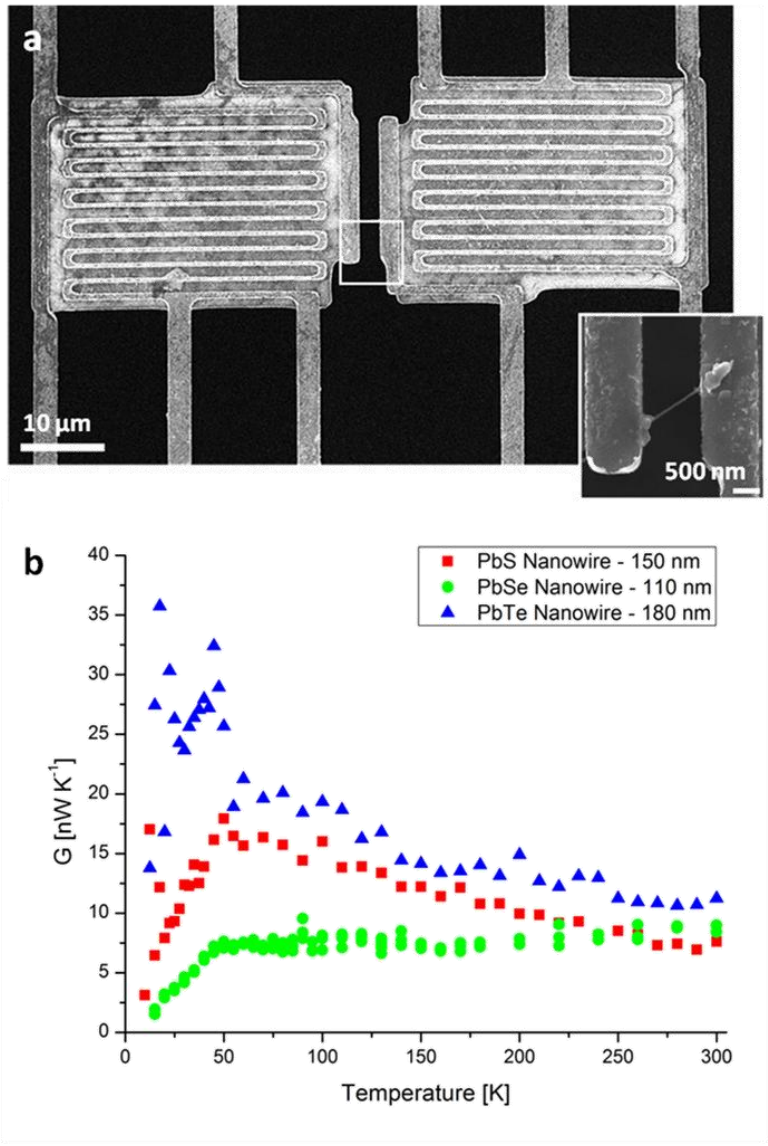

Figure 12: Thermal Conductance of CVT-Synthesized Pb*X* Nanowires: (a) SEM image of a nanowire bridging two suspended heating pads for thermal conductance measurement. Inset is the bridging nanowire highlighted in the main figure. (b) Temperature dependent thermal conductance of a PbS, PbSe, and PbTe nanowire. The nanowire diameters are 150, 110, and 180 nm, respectively.

In order to measure the thermal conductivity of these materials, individual nanowires were thermally bonded between suspended heating and sensing pads, as described previously[30]. The pads consist of suspended SiN_x

membranes with Pt lines patterned on top (Figure 12a). Each pad has a Pt coil and four contact lines to make four-point measurements of the coil resistance. To prepare thermal devices, substrates containing nanowires were briefly sonicated in isopropanol, and the suspension was drop-cast onto chips containing arrays of the microfabricated thermal measurement devices. Individual nanowires bridging the heating and sensing pads were thermally anchored to the suspended membranes by electron beam-induced decomposition of a Pt precursor using an FEI Strata 235 Dual Beam FIB. The external contact pads were wire-bonded to a 24-pin chip package and placed in a liquid Helium-cooled Lake Shore ST100 cryostat for measurement. One pad is heated by passing a current through the Pt coil, ramping the temperature ~2–5 K above the ambient temperature. The increase in resistance of the other pad is used to calculate the temperature rise at the cold end of the wire. The difference in temperature between the two pads can be used to calculate the thermal conductance of the nanowire.

The thermal conductance (G) measurements shown in Figure 12b are from silica-coated PbS, PbSe, and PbTe nanowires. The thermal conductivity can be calculated from the conductance using the diameter of the nanowire and the conduction length between the two suspended membranes[30]. The nanowires diameters were measured from SEM images of bridging devices. Though the bulk materials have a similar temperature-dependent thermal conductivity, the effects of phonon confinement can be seen as the nanowire diameter decreases. Even at 180 nm in diameter, the peak G of the PbTe nanowire is shifted out to 40 K as compared to 10 K in bulk[31]. The peak G of the 150 nm PbS nanowire occurs near 50 K, while the 110 nm PbSe nanowire has no apparent peak whatsoever. G of the PbSe nanowire is highest when it reaches 9 $nW \cdot K^{-1}$ at 300 K.

Using dimensions measured from SEM images, the thermal conductivity of the PbSe nanowire is estimated to be lower than those of bulk PbSe at the same temperatures by a factor of 10–1000[31]. The conductivity plateaus above 50 K, and approaches the bulk value near room temperature[24]. The peak in bulk thermal conductivity occurs when normal and Umklapp phonon-phonon scattering processes dominate other scattering mechanisms, such as boundary and impurity scattering[30]. In the PbSe nanowire, however, this transition shifts to higher temperatures because phonon scattering at the nanowire surface or $PbSe/SiO_2$ interface dominates thermal transport over a much larger temperature range.

In the Si nanowire case[30], thermal conductivity values even above 300 K are significantly lower than the bulk values due to strong boundary scattering. This is not the case for the PbSe nanowire, and in light of the fact that the phonon mean free path in bulk PbSe[8] is significantly shorter than in Si, phonon transport may be operating in an intermediate regime at the PbSe nanowire size scale. The significant increase in phonon scattering as compared to bulk at low temperatures—when phonon mean free paths are long—and the regression to bulk scattering processes as the mean free path drops below the nanowire diameter, suggest a smaller diameter nanowire may be necessary to effectively scatter phonons at high temperatures. Nonetheless, the large disparity between nanowire and bulk thermal transport below 100 K may improve the *ZT* of nanowire-based Pb*X* materials in this temperature region.

2.4.d - CVT-Synthesized Pb*X* Nanowires: Conclusions

In summary, lead chalcogenide nanowire arrays have been synthesized by a CVT method. XRD, SEM, HRTEM, SAED, and EDX were used to characterize the nanowire structures, and they were found to be single crystalline. This CVT method is equally applicable to PbS, PbSe, and PbTe nanowires, and may possibly be extended to the Pb*X* alloy nanowire systems for better engineering of phonon scattering. The thermal conductivity of PbSe nanowires is greatly diminished from the bulk PbSe values below 100 K, and may significantly increase the overall efficiency of these materials in this temperature region. In order to accurately gauge their potential as novel thermoelectric materials, future experiments should include Seebeck coefficient measurements. The decrease in thermal conductivity of two to three orders of magnitude suggests that nanowire systems of promising thermoelectric bulk materials could push the upper limits of their Z*T* values.

2.4.e - CVT-Synthesized Pb*X* Nanowires: Follow-up

After this work was completed several research group published additional information on CVT-synthesized Pb*X* nanowires. Cui and coworkers used a CVT synthesis to grow hyperbranched PbSe nanowires by a VLS mechanism using In, Ga, and Bi catalysts and a PbSe precursor[32]. By using PbSe rather that $PbCl_2$, they were able to eliminate the deposition on SiO_2 on the surfaces of the PbSe nanowires. They also used NaCl as an epitaxial substrate for the growth of oriented PbSe nanowire networks. Jin and coworkers proposed a self-catalyzed VLS growth of PbSe and PbS nanowires grown by CVT using the same precursors used in our synthesis[33]. Based on these two results, it is likely that our nanowires did indeed grow via the VLS mechanism. In addition to epitaxial growth on NaCl, PbS nanowires have also been grown on rutile TiO_2 and muscovite mica[34].

In 2008 the groups of both Song Jin and Yi Cui proposed a catalyst-free growth mechanism for Pb*X* nanowires with branched and pine-tree morphologies wherein the 1-D growth of the nanowires is promoted by axial screw dislocations that provide step edges for layer by layer crystal growth[35,36]. As the nanowires grow, the strain caused by the screw dislocations creates a twist in the nanowires called Eshelby twist. The central nanowire is grown by a dislocation-driven mechanism and the branches are grown by the VLS mechanism from the deposition of Pb droplets. This mechanism is unlikely to have been a factor in the 1-D growth of our Pb*X* nanowires due to the absence of the Eshelby twist. Low super-saturation conditions are necessary to promote the dislocation-driven growth over the VLS growth[37] and likely did not exist in our reactor. Jin and coworker also showed the generality of the mechanism by showing that it is also responsible for the 1-D morphology of hydrothermally grown ZnO nanowires and nanotubes[38].

In 2009 Jang et al. reported on the transport properties of n-type PbTe nanowires grown by CVT[39]. Although they used synthetic conditions similar to ours, the PbTe nanowires produced in their synthesis were n-type. They measured the electrical transport properties and found that their PbTe nanowires had carrier concentrations of 8.8×10^{17} cm^{-3} and mobility values of 0.83 $cm^2 \cdot V^{-1} \cdot s^{-1}$. Their mobility values were very similar to that obtained for our p-type PbTe

nanowires. They also measured a Seebeck value of -72 $\mu V \cdot K^{-1}$ which is significantly less than the 300 $\mu V \cdot K^{-1}$ measured in bulk PbTe with similar carrier concentration[40].

Additional results on the thermal conductivity of CVT-synthesized PbTe nanowires have been reported by Roh et al[41]. Using PbTe nanowires with different diameters (436, 277, 182 nm) they showed a decrease in thermal conductivity with nanowire diameter. The 182 nm PbTe nanowire had a thermal conductivity of 1.29 $W \cdot m^{-1} \cdot K^{-1}$ at 300 K which is very similar to the thermal conductivity measured in our study for a 180 nm PbTe nanowire (~1.5 $W \cdot m^{-1} \cdot K^{-1}$). Their value is approximately half of that measured for bulk PbTe (~2.4 $W \cdot m^{-1} \cdot K^{-1}$)[5]. The shapes of their thermal conductivity vs. temperature plots were similar to that observed in our study and indicate the importance of boundary scattering in the reduction of the thermal conductivity. The 436 nm PbTe nanowire measured in their study has a thermal conductivity similar to that of the bulk while the 277 nm nanowire has a thermal conductivity less than the bulk. These results indicate that the phonon mean free path in PbTe is somewhere between 277 and 436 nm.

2.5 – Synthesis, Characterization, and Thermoelectric Properties of PbSe Nanowires Grown by Solution-Phase Methods

While the CVT synthesis of Pb*X* nanowires was successful in producing high-quality single-crystalline nanowires, there were some drawbacks to the CVT synthetic technique including a low yield of nanowires, large nanowire diameters (d > 40 nm), and using $PbCl_2$ as a precursor, the nanowires were coated with an insulating SiO_2 layer. In addition, the evaporation of Pb and chalcogenide precursors can produce an array of toxic fumes, including H_2S. In comparison to the CVT synthesis, solution phase methods are often more reproducible, as well as safer, since they eliminate the use of toxic vapor species. Solution phase methods are also capable of producing nanowires with diameters as small as 3.5 nm, which, according to theory by Dresselhaus and coworkers, could possess a high *ZT*[8]. Taking these points into consideration a solution-phase synthesis was used for further studies on the thermoelectric properties of lead chalcogenide nanowires.

2.5.a – Synthesis of PbSe Nanowires by Solution-Phase Methods

All PbSe solution phase nanowires were prepared using standard Schlenk line techniques under Ar flow using a procedure similar to that reported by Cho et al[12]. The morphology, diameter, and length of the nanowires could be tailored by changing the stabilizing agent and growth time. The lead and selenium precursors for all syntheses were lead oleate and trioctylphospine selenide (TOPSe). The TOPSe was prepared by adding 0.55 g of Se to 40 mL of TOP and heating for 5 minutes at 150°C. To generate lead oleate, either 0.44g of

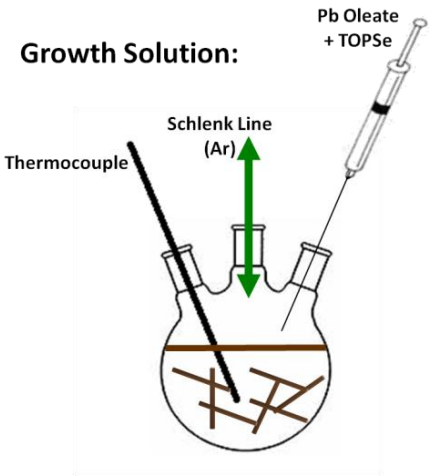

Figure 13 – Schematic of Solution Phase Synthesis: Growth solution immediately after injection of TOPSe and Pb oleate precursors to form PbSe nanowires.

PbO or 0.76 g of lead acetetate trihydrate ($Pb(Ac)_2 \bullet 3H_20$) were reacted with 2 mL of oleic acid in 8 or 10 mL of diphenyl ether, respectively. Use of PbO over $Pb(Ac)_2 \bullet 3H_20$ reduced the amount of water that had to be removed from the solution during drying. Complete removal of water appears to be important for synthesis of long, ultra-thin PbSe nanowires. The flask of PbO (or $Pb(Ac)_2 \bullet 3H_20$), oleic acid, and diphenyl ether was heated under vacuum at 85°C for 30 min (drying) then heated at 150°C under Ar (formation of Pb oleate), followed by a second 30 min heating under vacuum at 85°C. After cooling the lead oleate solution to 60°C, 4 mL of TOPSe were injected. It is important that both the TOPSe and lead oleate solutions be cooled to prevent premature nanoparticle nucleation. Once the TOPSe and Pb oleate were mixed, the entire solution was immediately injected into 15 mL of dried phenyl ether preheated to 250°C. The temperature drop after injection was critical to determining the product of the reaction. If the temperature dipped below 170°C the majority of the product was nanoparticles, while temperatures above 170°C produced a majority of nanowires[12]. The reaction was allowed to heat for 50 seconds and then cooled to room temperature using a water bath. The nanowire solution was mixed with an equal volume of hexanes and centrifuged at 6000 rpm for 30 minutes. The product was washed a second time with hexanes and stored in chloroform. The nanowires remained stable in solution for a period of over a year.

To tailor the morphology of the nanowires additional stabilizers were added to the phenyl ether growth solution. Using only oleic acid as a stabilizer (no additional stabilizers) the nanowires were capped entirely by {111} facets giving the nanowires a zigzag morphology. A similar morphology was achieved using hexadecylamine (HDA). It is presumed that both oleic acid and HDA stabilize the {111} facets over the {100} facets causing the {100} facets to grow more rapidly. With longer growth times the less stable {100} facets continued to grow producing a branching effect. By using n-tetradecylphosphonic acid (n-TDPA) the {100} facets were stabilized, giving straight nanowires.

Growing the nanowires for only 50 seconds produced nanowires with lengths of 10-30 µm and diameters 7-10 nm. By extending the growth time to 2 min the diameters were increased to 50–100 nm and the lengths decreased to 5-10 µm due to Oswald ripening. Further tuning could be achieved using different growth times.

2.5.b – Structural Characterization of Solution-Synthesized PbSe Nanowires

The anisotropic nature of these PbSe nanowires is believed to originate from the oriented attachment of PbSe nanocrystals[12]. Due to the strength of interaction between the nanocrystals, the force is likely to be a result of dipole-dipole interactions. Calculations by Murray and coworkers have shown that the most probable, as well as strongest dipole moment is that directed along the <100> direction. In the NaCl fcc crystal structure of PbSe, the {100} facets are capped by both Pb and Se and the {111} facets are capped by either Pb or Se. To keep the proper stoichiometry, four for the {111} facets are capped by Pb and four are capped by Se. The electronegativities of Pb and Se are 2.33 and 2.55, respectively, giving a difference of 9.4%. Depending on the arrangement of the Pb and Se terminated {111} facets, a dipole can exist in the [100], [110], or [111] directions. Klokkenburg et al. used cryogenic TEM to study the presence of dipoles within liquid dispersions of PbSe nanocrystals[42]. They observed anisotropic assembly of the nanoparticles and calculated a dipolar attraction of $-8 \pm 1\ k_BT$ for spherical PbSe nanoparticles (6.8 nm diameter). Using this unique growth mechanism, nanoparticles with a variety of shapes can be assembled to produce different nanowire morphologies. The only requirement is that the nanoparticles have some percentage of {111} facets. Cubic particles cannot be assembled into nanowires since they are capped entirely by {100} facets, thus eliminating the dipole. It is important to note that in order to obtain high quality nanowires

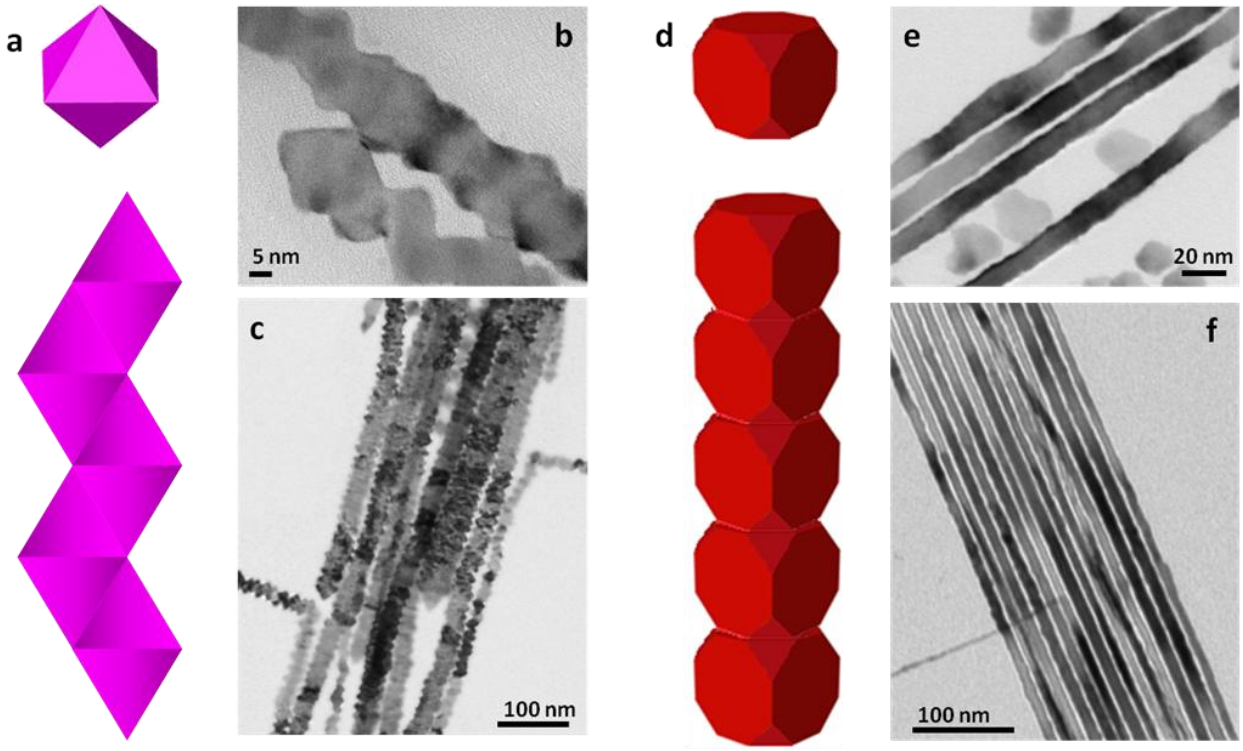

Figure 14 – Oriented Attachment of Nanoparticles: (a) Oriented attachment of octahedral nanoparticles to form zigzag nanowires. (b,c) TEM images of the zigzag nanowires prepared using oleic acid as a stabilizer. (d) Oriented attachment of truncated cubic nanoparticles to form straight nanowires. (e,f) TEM images of the straight nanowires prepared with n-TDPA as a stabilizer.

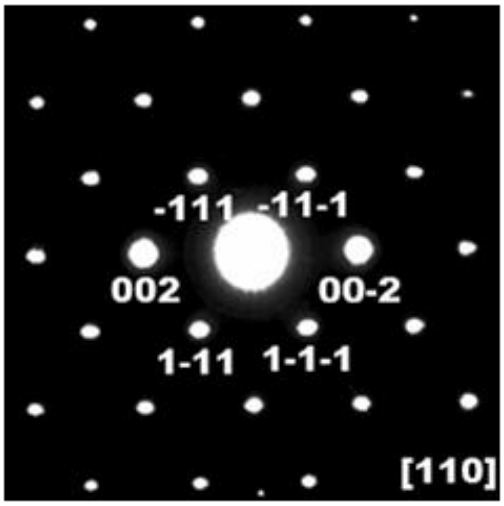

Figure 15 – Electron Diffraction Pattern from a single PbSe Nanowire: SAED pattern of a PbSe nanowire taken from the [110] zone axis showing the single crystallinity of the nanowire and confirming the growth direction as <100>.

without interfacial defects, the nanoparticle growth and assembly must occur simultaneously. At the high temperatures present during nanowire assembly, interfacial defects can be removed. A large density of defects can be seen in nanoparticles assembled at room temperature, which will lead to poor electrical properties[12]. Both PbS[43] and PbSe[12,44] nanowires have been synthesized by this growth mechanism. However, there are no reports of PbTe nanowires grown by oriented attachment.

By adding different stabilizers during the synthesis of the PbSe nanowires it was possible to control the shape of the nanoparticles that would later assemble into nanowires. When only oleic acid or oleic acid and HDA were used, the {111} facets were stabilized over the {100} facets. This generated octahedral particles that, when assembled, produced nanowires with a zigzag morphology (Figure 14 a-c). This morphology is ideal for decreasing thermal conductivity, since an increased surface area will lead to an increase in boundary phonon scattering. Other morphologies, such as straight nanowires, could be obtained using alternative stabilizers[12]. For example, n-TDPA stabilized the {100} facets over the {111} facets giving truncated cubes. If the growth were allowed to proceed at temperatures below 170°C the nanoparticles would eventually be cubic. However, at higher temperature the truncated cubes (still containing some {111} facets) were able to assemble to give straight nanowires

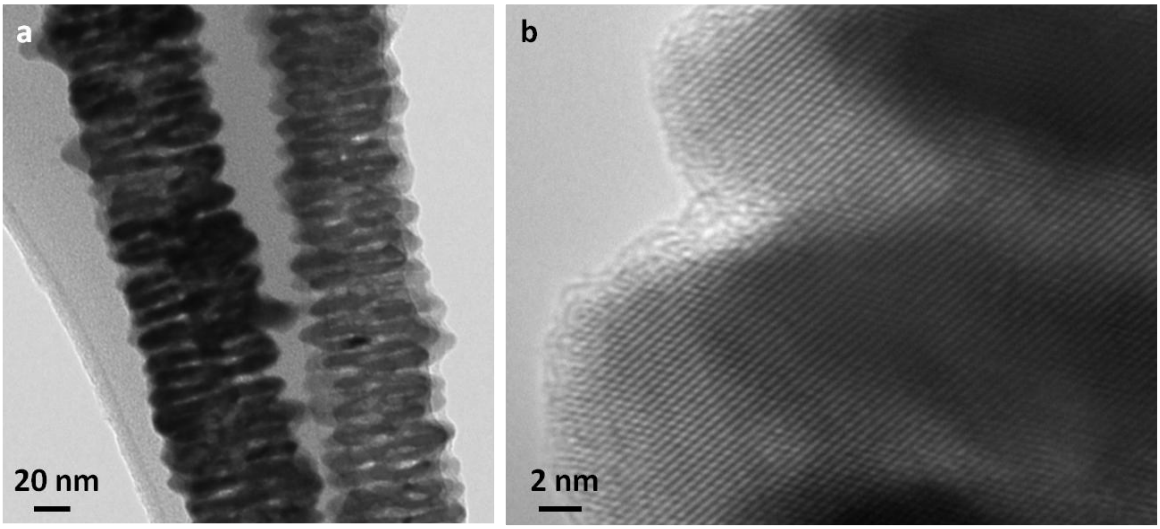

Figure 16 – TEM images of PbSe Nanowires prepared with a 2 minute growth time: (a) TEM image showing the branched morphology of the nanowires. (b) HRTEM image showing the single-crystalline nature of the branched nanowires.

(Figure 14 d-f). The diameter is still somewhat modulated in the final nanowires as a result of the truncation of the cubes. It is likely that if the growth were allowed to continue for a longer time the nanowires would become completely smooth as a result of atom migration along the nanowire surface. All nanowires synthesized in this study grew in the <100> direction as determined by SAED. A representative pattern from a nanowire synthesized with an oleic acid stabilizer is shown in Figure 15.

Increasing the growth time from 50 sec to 2 min caused a significant increase in nanowire diameter from around 10 nm to closer to 100 nm. Using oleic acid as the only stabilizer these nanowires showed a very unique morphology. Since the {111} facets are capped by oleic acid, their growth is significantly slowed compared to that of the {100} facets. Thus, growth continues at a faster rate in the [100] directions producing branches on the nanowire (Figure 16). In nanoparticles prepared using the same growth times, star-shaped nanoparticles result. The branching introduces additional roughness, making the nanowires ideal for thermoelectric measurements. In addition, compared to the 10 nm nanowires generated after 50 sec of growth, the larger diameters of these nanowires make them much easier to handle for device fabrication. Despite the polycrystalline appearance of the nanowires HRTEM confirms that they are single-crystalline across these nanoparticle "boundaries".

The nanowire yield for this synthesis is almost 100%, eliminating the need for size-selective precipitation and removal of nanoparticles. However, when the product was entirely composed of nanowires the nanowires tended to bundle together, making it difficult to separate a single nanowire for measurement. Some of the bundling issues could be averted by allowing a small concentration of nanoparticles to remain in solution. These nanoparticles often collected around individual nanowires separating them from one another.

The structure and composition of the nanowires were verified by XRD and EDS. XRD

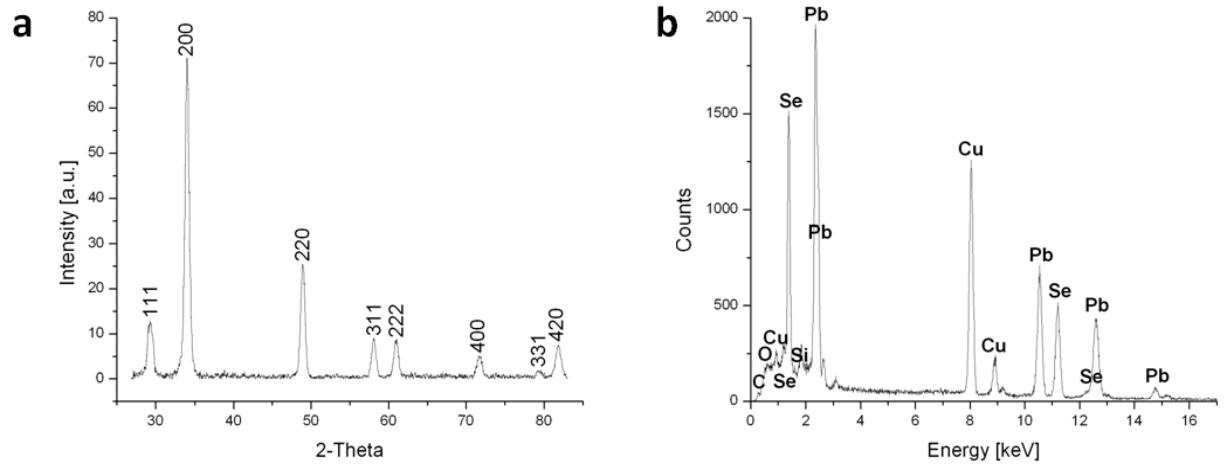

Figure 17: XRD and EDS of PbSe Nanowires: (a) XRD pattern of a PbSe sample made with an oleic acid stabilizer. All peaks were indexed to fcc PbSe. (b) EDS spectrum showing the purity of the PbSe nanowire sample.

patterns of the PbSe nanowires taken using Co K_α irradiation (Figure 17) demonstrate the high quality, crystalline nature of the materials. All diffraction peaks were indexed to fcc PbSe indicating the formation of a pure product. The EDS spectra also verify their purity, with the Cu peaks arising from the copper grids used for TEM analysis.

2.5.c – Thermoelectric Properties of Solution-Synthesized PbSe Nanowires

Electrical, Seebeck, and thermal conductivity studies were all based on single nanowire measurements, allowing the intrinsic properties of the nanowire to be clearly distinguished from ensemble effects. Although PbSe nanowires are relatively flexible at the size scale used in this study, they remain fragile and are very sensitive to processing steps and conditions. Consequently, great care was taken in every step of device fabrication to avoid thermal shock, mechanical stress, and oxidation. Prior to device fabrication, the as-made PbSe nanowires were washed with ethanol, followed by centrifugation and redispersal in chloroform. The devices used for thermopower and electrical measurements were constructed in the same way except the thermopower devices were fabricated on Pyrex glass and the electrical devices were fabricated on either Pyrex or Si wafers with a 600 nm coating of thermal oxide. Immediately upon evaporation of the solvent, the substrate was coated with I-line photoresist. Standard photolithographic processing was used to pattern the electrodes. 1/150/35 nm Ti/Pd/Au metal films were then deposited by electron-beam evaporation. The evaporation step was divided into 5 min segments, between which the chip was allowed to cool down for 5 min to prevent overheating. Finally, the substrate was soaked in acetone for 30-60 min to dissolve the photoresist and lift off the metal film. All devices were stored in a desiccator under vacuum and measurements were performed in air. The electrical properties of the nanowires slowly degraded if exposed to air and after several days the nanowires became insulating. When kept in a desiccator they could be preserved for months.

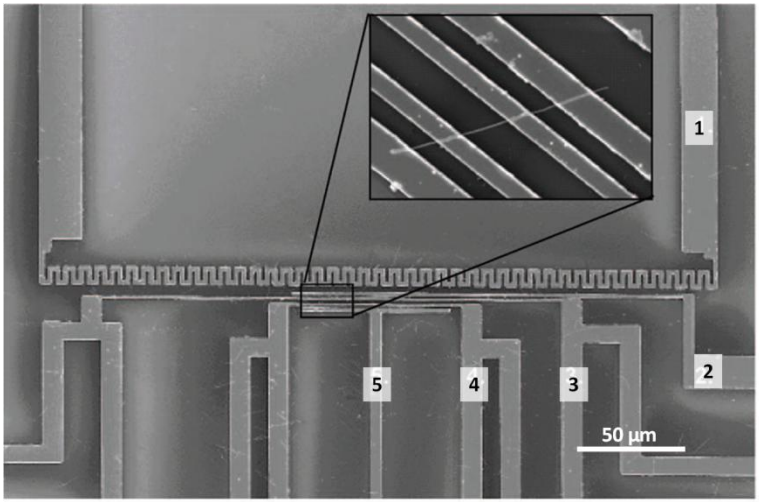

Figure 18 – Single Nanowire Devices: SEM image of the circuit used for electrical and thermoelectric power measurements of single PbSe nanowires. Electrode 1 is a heating line, and 2, 3, 4, and 5 are for four-point probe resistance measurements. Electrodes 3 and 4 are used as electrodes and resistive thermometers for the thermoelectric power measurement. Inset shows a PbSe nanowire bridging electrodes 2-5.

Figure 18 shows an SEM image of a device with a single PbSe nanowire bridging four

electrodes. A heater was positioned next to the electrodes to generate a temperature gradient in the direction normal to that of the electrodes[6,45]. Any pair of electrodes could be used to measure the electrical conductance and thermal voltage generated in the PbSe nanowire when heated. The middle two electrodes were each attached to four electrodes so the change in their resistance as a function of temperature could be recorded and calibrated, allowing them to serve as temperature sensors for thermopower measurements.

Four-point probe measurements were used to study the electrical properties of single PbSe nanowires. A voltage was applied between the outer two electrodes using a National Instruments 6052E multifunction data acquisition (DAQ) card while the drain current (I) on the outer electrodes and voltage (V) between the inner two electrodes were monitored using a DL 1211 current preamplifier and Stanford Research Systems SR560 voltage preamplifier, respectively. The field-effect properties of single PbSe nanowires were measured by applying a gate voltage (V_g) to the device. Current passing through the nanowire evolved linearly with voltage, suggesting that the Ti/Pd/Au formed ohmic contacts to the PbSe nanowire. Two-point probe and four-point probe resistance measurements confirmed that the contact resistance was indeed negligible. The as-made PbSe nanowires had resistivities ranging from 0.1 to 1 Ω·cm.

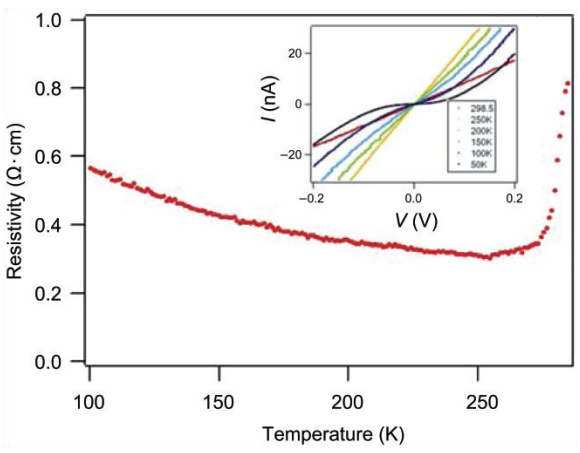

Figure 19 – Temperature Dependent Resistivity: Single-nanowire resistivity measurements as a function of temperature. Inset is a four-point probe *I-V* measurement at different temperatures.

I-V characteristics of PbSe nanowire devices were studied under different gate voltages[46]. Plots of the conductance (G) vs. V_g of single nanowire devices show that increasingly negative values of V_g led to more conductive PbSe nanowires. This trend indicates that the PbSe nanowire has hole-dominated charge transport and that the nanowire is a p-type semiconductor. A large proportion of the measured PbSe nanowire devices with ohmic contacts showed no change in conductance with varying gate voltage, suggesting that they were degenerately doped with holes. A carrier concentration of 10^{19} cm^3 and higher is ideal for semiconducting thermoelectric materials. Hence, our as-made PbSe nanowires exhibit a suitable carrier concentration without the need to introduce other dopant species.

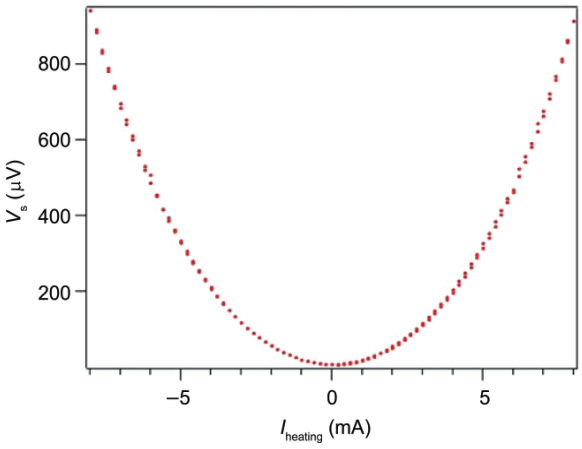

Figure 20 – Thermal Voltage: Thermal voltage measured across a single PbSe nanowire

The temperature dependent four-point probe resistivity is shown in Figure 19. As the

temperature decreased from 300 K, resistivity initially dropped sharply and then increased more slowly. This temperature dependence was reproducible, although the amplitude of the change in resistivity varied from device to device. The metallic-type temperature dependence near room temperature is consistent with the fact that the PbSe nanowires are heavily doped and charge carrier scattering predominates. At lower temperatures (~200 K to 100 K), on the other hand, thermal excitation of charge carriers dominates. From the temperature dependent resistivity plot, the calculated thermal excitation energy was 10 meV. When temperature dropped below 100 K, the four-point probe *I-V* curves became non-linear, suggesting that an energy dependent scattering mechanism operates inside the nanowires.

Devices for thermopower measurement were fabricated on Pyrex glass substrates in order to achieve larger temperature gradients at a given heating power. A Keithley 236 source-measurement unit was used as a current source to generate heat in the heater, while the thermal voltage between the attached electrodes on the hot and cold ends of a single PbSe nanowire was recorded using a Keithley 2182 nanovoltmeter. The sign convention is such that a positive voltage indicates that hole carriers are responsible for thermal transport. Figure 20 shows a plot of measured thermal voltage from a PbSe nanowire as a function of heating current. Positive thermal voltages were generated and the voltages evolved in a parabolic fashion with heating current. A heating current of 8 mA produced a thermal voltage of 920 μV across the nanowire. During the heating process the change in resistance of the thermal sensors was recorded using two lock-in amplifiers. The temperatures of the electrodes were calibrated using temperature coefficient of resistance (TCR) measurements. The thermopower is given by $S = V_s/\Delta T$, where V_s is the thermal voltage and ΔT is the temperature difference across the nanowire. More than 10 samples were measured and their thermopowers ranged from 223 to 445 $\mu V \cdot K^{-1}$ with an average of 339 $\mu V \cdot K^{-1}$. These values are comparable to that of bulk PbSe with comparable charge carrier concentrations[47].

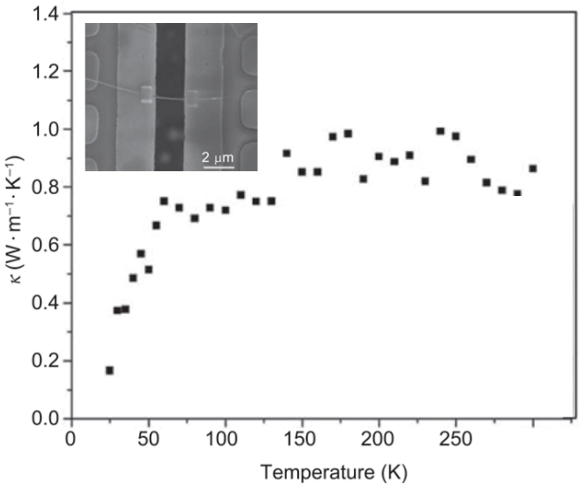

Figure 21 - Thermal Conductivity of PbSe: Thermal conductivity as a function of temperature for a single PbSe nanowire. Inset is a SEM image of the measured device.

To measure the thermal conductivity of individual PbSe nanowires, they were drop-cast onto prefabricated devices [30,48]. The devices consisted of suspended SiN_x heating and sensing pads, each with a Pt heating coil and four Pt contact lines. Once an individual nanowire was found bridging the heating and sensing pads, it was bonded with Pt to create a better thermal interface (Figure 21, inset). To measure the thermal conductivity of a suspended nanowire, the temperature of one pad was increased while the temperature change of the opposite pad was recorded. An increase in temperature of the sensing pad was due to heat transfer from the heating pad through the PbSe nanowire. The nanowire dimensions were estimated from SEM images and the thermal conductivity was calculated using methods described in previous

reports[30,48]. The thermal conductivity of an individual PbSe nanowire was 0.8 $W \cdot m^{-1} \cdot K^{-1}$ at 300 K, and below 100 K the thermal conductivity dropped drastically, possibly due to phonon boundary scattering.

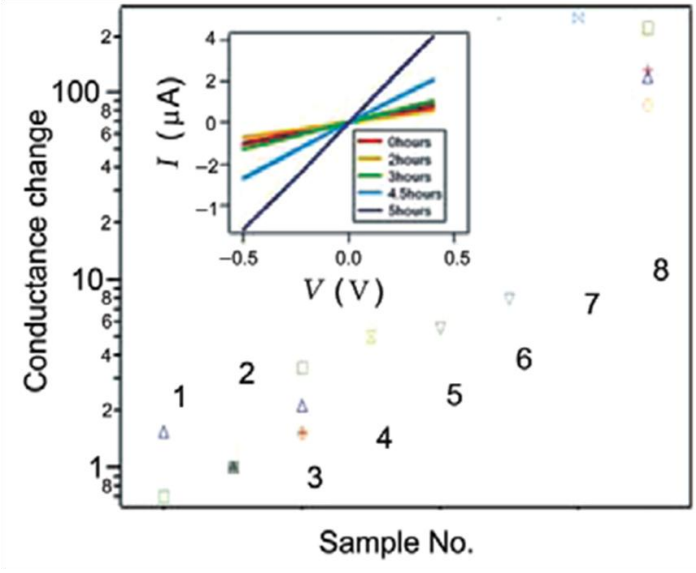

Figure 22 – Conductance Change with Annealing: Ratio of conductivity change under the following annealing conditions. Sample #1: before annealing, #2: 180°C, 2 hrs, #3: 180°C, 10 hrs, #4: 200°C, 0.5 hrs, #5: 200°C, 1 hr, #6: 200°C, 4 hrs, #7: 200°C, 7 hrs, #8: 250°C, 7 hrs. Inset: *I*–*V* curves of a single PbSe nanowire annealed at 200°C for different durations.

At 300 K, a *Z*T value of ~0.04 was estimated for single, as-made PbSe nanowires by combining the results of electrical, thermopower, and thermal conductivity measurements. One reason for this low value of *Z*T is that the charge carrier mobility of the nanowires is still two orders of magnitude lower than that achieved in the bulk[46,49]. This reduction in mobility could be a result of surface trap states and point defects, which can serve as scattering centers.

Thermal annealing has been shown to reduce nanowire defect density[50] and could possibly help improve the thermoelectric properties of the PbSe nanowires. Pyrex chips holding PbSe nanowire devices were therefore annealed at 180 to 250°C in a tube furnace under a nitrogen pressure of 1 Torr. Electrical properties were measured before and after annealing under different conditions. The inset in Figure 22, inset shows *I*-*V* curves for a PbSe nanowire annealed at 200 °C for various times. The color-coded *I*-*V* curves represent the nanowire after annealing times of 0, 2, 3, 4.5, and 5 hrs. A significant increase in electrical conductance was observed during the annealing process. After 5 hrs, the nanowire conductance increased to 14 times its value prior to annealing. Figure 22 summarizes the enhancement in electrical conductance under different annealing conditions. Essentially, by changing the annealing temperature and time, the electrical conductance could be tuned by up to three orders of magnitude. Thus, the thermoelectric properties of individual PbSe nanowires could be explored as a function of resistivity from 0.4 Ω·cm to 4×10^{-4} Ω·cm. TEM studies showed no noticeable change in crystallinity or morphology of the nanowire due to the annealing process.

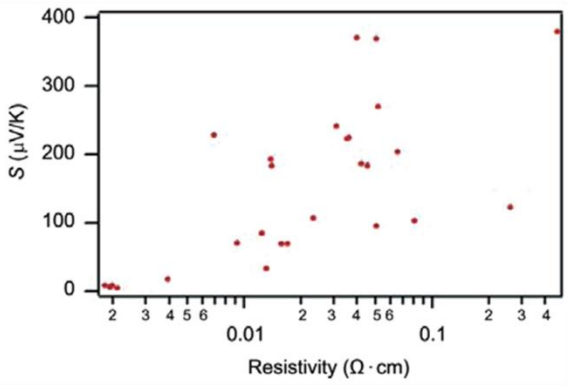

Figure 23 - Seebeck vs. Resistivity: Seebeck coefficient of annealed single nanowires as a function of their resistivity.

The thermopower of annealed PbSe nanowire devices as a function of nanowire

resistivity is summarized in Figure 23. The Seebeck coefficient was positive for all samples, indicating that holes were still responsible for charge transport in the annealed nanowires. The Seebeck coefficient decreased with decreasing resistivity, strongly suggesting that the hole concentration increased with annealing time and temperature. This increase in hole concentration could result from an increase in Pb vacancies during the annealing process.

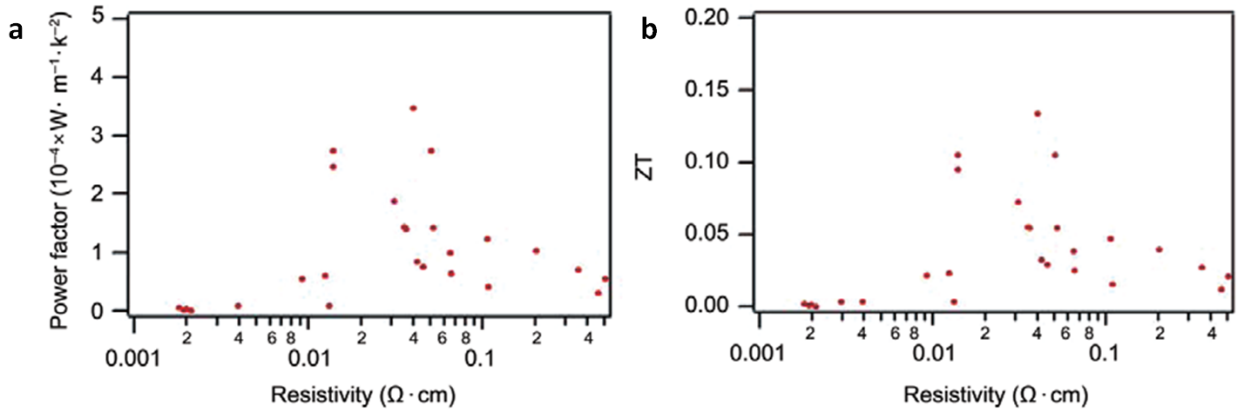

Figure 24 - Thermoelectric Properties: (a) Power factor of annealed nanowires as a function of their resistivity. (b) *Z*T of annealed nanowires as a function of their resistivity at 300 K.

The power factor ($S^2\sigma$) and *Z*T at 300 K as a function of resistivity are shown in Figure 24. As the resistivity decreased, the power factor and value of *Z*T increased until reaching a peak around 0.04 Ω·cm. The highest room temperature power factor and value of *Z*T observed in the measured devices were 3.5×10^{-4} W·m^{-1}·K^{-2} and 0.12, respectively. The maximum value of *Z*T achieved was three times that of the as-made nanowires.

2.5.d - Thermoelectric Properties of Solution-Synthesized PbSe Nanowires: Modifying the electrical conductivity and Seebeck coefficient via Gating

The carrier concentration of single PbSe nanowires could also be tuned by gating, affecting the electrical conductivity and Seebeck coefficient of the nanowires. The circuit shown in Figure 18 was also used for gating experiments. The as-synthesized nanowires were first dispersed in chloroform and cast by spin-coating onto a silicon substrate coated with a 600 nm SiN_x film. The procedure reported in the previous section was used to pattern the electrodes, again taking care to prevent thermal shock, mechanical stress, and oxidation. The thermoelectric properties of the PbSe nanowires could be directly modulated during measurement by applying a gate voltage to the underlying silicon substrate, similar to the carbon nanotube devices described previously[51,52].

Due to the air sensitivity and chemical instability of the PbSe nanowires[12] we have intentionally passivated the nanowire surface with a thin Al_2O_3 film. After device fabrication the nanowires were first annealed under 700 mTorr of N_2 at 200°C for up to 4 hrs. Atomic layer

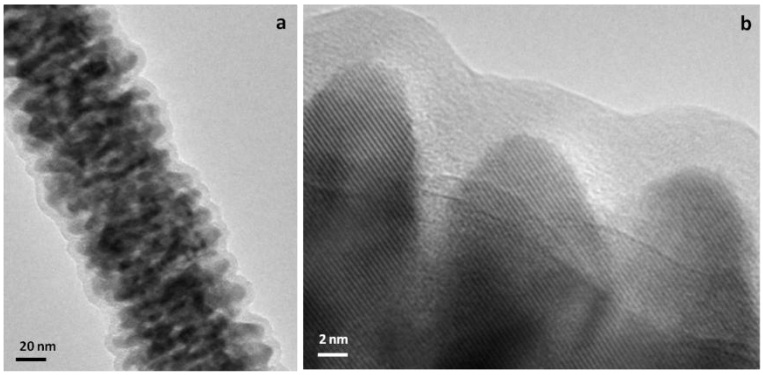

Figure 25 – PbSe nanowires passivated by Al_2O_3: (a) TEM image of a PbSe nanowire showing the conformal Al_2O_3 coating. (b) HRTEM image showing the 6 nm Al_2O_3 coating and preservation of the single-crystallinity within the nanowire.

effectively stabilized the air-sensitive PbSe nanowires. All previous electrical studies on PbSe nanostructures had to be performed under either inert atmosphere[6,12,54] or vacuum[32]. By using the Al_2O_3 coating, we found our individual PbSe nanowire devices could be tested in ambient conditions without noticeable change for more than half a year. This strategy provides a practical route for stabilizing lead chalcogenide nanostructures, allowing them to be used in a broader range of applications.

Figure 26 show typical electrical transport behavior of a single PbSe nanowire field-effect transistor before (a) and after (b) coating by ALD Al_2O_3. As shown in the insets, the current versus applied voltage (*I* -*V*) plots at different gate voltages (V_g) were all linear, indicating that Ohmic contacts were formed between the metal and nanowire in both cases. Typical values for the four-point resistance of individual nanowires were on the order of several hundred kΩs and showed minimal (<0.5%) contact resistance. Single PbSe nanowires were able to conduct currents up to 10 μA without failure, corresponding to a breakdown current density of approximately 5×10^5 A·cm^{-2}. These deposition (ALD) methods were then used to deposit the Al_2O_3 at 50 °C following previously reported procedures[53]. Figure 25 shows TEM and HRTEM images of PbSe nanowires coated with ALD-deposited Al_2O_3. This procedure readily produced a conformal ~6 nm coating of Al_2O_3 without altering the morphology, microstructure, or crystalline nature of the nanowires.

The low-temperature ALD method used to coat the PbSe nanowire devices with Al_2O_3

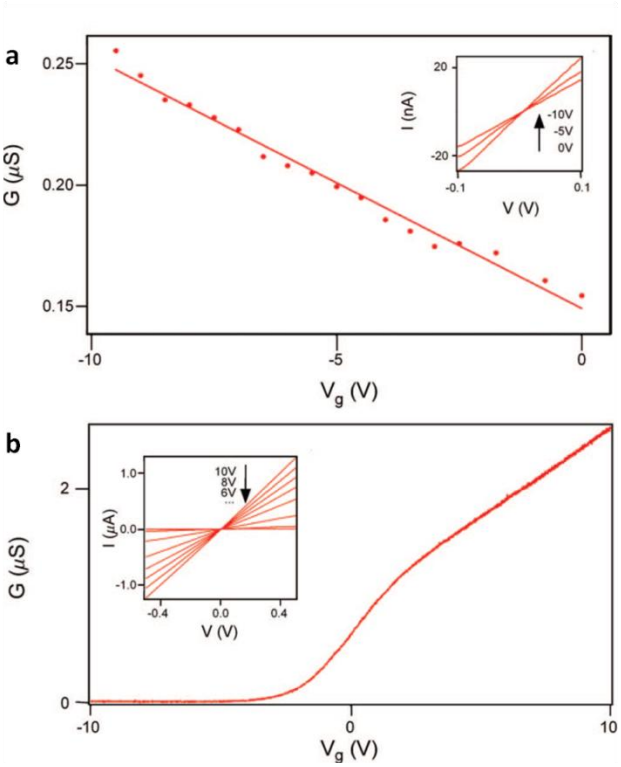

Figure 26 – Electrical Measurements on as-made and Al_2O_3-coated PbSe Nanowires: (a) Conductance of an as-synthesized single PbSe nanowire as a function of gate voltage (V_g). Inset: *I-V* behavior of the same PbSe nanowire taken at V_g = -10, -5, and 0 V. (b) Conductance of a single PbSe nanowire coated with Al_2O_3 as a function of V_g. Inset: *I-V* behavior of the same coated nanowire at V_g = 10, 8, 6, 4, 2, 0, and -2 V.

values, along with the TEM observations, indicate that these devices comprise high-quality, single crystalline nanowires with Ohmic contacts.

One significant difference in the electrical transport behavior before and after Al_2O_3 coating is the sign of the charge carriers responsible for conduction in the nanowires. As shown in part a (b) of Figure 26 the conductance of single nanowire transistors decreased (increased) with increasing V_g before (after) Al_2O_3 deposition. These opposite trends indicate a switch in the polarity of free charge carriers due to the Al_2O_3 coating; that is, PbSe nanowires were p-type before and n-type after coating. Considering the narrow band gap (280 meV)[55] and high reactivity of PbSe, changes in the electron density at the surface, either due to adsorbed species or chemical reactions, could readily affect the carrier density or polarity within the nanowire. For example, it was previously observed that treatment of PbSe nanoparticle films with hydrazine also changed the polarity of the majority charge carriers from p- to n-type[6,54]. Our ALD process could result in an Al_2O_3 film with a positively-charged surface[56], and we tentatively attribute the change in carrier type to the effective gating by the positively charged Al_2O_3 layer.

The mobility of the charge carriers in the nanowires, μ, can be extracted from their transconductance (dG/dV_g) and geometric factors derived from modeling the nanowire field-effect transistor using a cylinder-plane capacitor model[57,58]

$$\mu = \frac{dG}{dV_g} \ln\left(\frac{2h}{r}\right) \frac{L}{2\pi\varepsilon_0\varepsilon}$$

where h is the SiN_x thickness, r and L are the nanowire radius and length, and ε_0 is the vacuum permittivity and ε is the SiN_x relative dielectric constant. For two of the n-type PbSe nanowire devices, the drift mobilities were calculated to be 76 (Figure 26b) and 180 $cm^2 \cdot V^{-1} \cdot s^{-1}$. The charge carrier concentration was measured as 1.8×10^{18} cm^{-3}. The as-synthesized p-type nanowires, on the other hand, exhibited much lower mobilities of about 3 $cm^2 \cdot V^{-1} \cdot s^{-1}$. The data in Figure 26a yields a mobility of 2.7 $cm^2 \cdot V^{-1} \cdot s^{-1}$ and a carrier concentration of 6×10^{18} cm^{-3}. A possible cause of the enhancement of mobility in Al_2O_3-coated samples could be the passivation of both surface defects and charge trap states by the high quality ALD Al_2O_3 film. Although the highest mobility value measured is still an order of magnitude lower than observed values of the Hall mobility in bulk PbSe[49], it is by far the largest mobility reported for lead chalcogenide nanostructures[54]. Further improvements in sample preparation and processing could augment these values. Additionally, we note that the model used to calculate the drift mobility from the transconductance provides only a lower bound of the actual value[58]. Overall, atomic layer deposition of alumina resulted in air-stable PbSe nanowire devices with inversion of charge polarity and enhanced carrier mobility. Field-effect gating of such PbSe nanowire devices readily changed their conductance by 2 orders of magnitude (Figure 26b).

To measure the thermoelectric power (Seebeck coefficient) of individual Al_2O_3-coated nanowires, a current was passed through the heater shown in Figure 18 (electrode 1), creating a thermal gradient across the nanowire bridging the electrodes. The voltage measured across the two inner electrodes (3 and 4 in Figure 18) in the temperature gradient is the thermal

voltage (V_{therm}), from which the thermoelectric power, S, is calculated as $S = V_{therm}/\Delta T$. As shown in Figure 27a the measured V_{therm} values were plotted as a function of heating current, I_{heat}, applied to the heater. The parabolas correspond to V_{therm} measurements from the same nanowire under different applied V_g. The sign convention is such that negative V_{therm} values are measured for n-type samples due to the negative polarity of the majority charge carriers that transport heat, i.e., $V_{therm} < 0$ when electrode 3 has a higher voltage potential than electrode 4.

The negative values of V_{therm} are consistent with the charge carrier type determined by the transconductance measurements in Figure 26b. The temperature of the heater is proportional to the heating power and thus proportional to I_{heat}^2. V_{therm} as a function of I_{heat} was recorded in Figure 27a for different gate voltages (and hence different conductivities). The ΔT along the nanowire was measured between the same two electrodes used to obtain V_{therm} and was calculated using a calibration of the metal line four-point resistance at fixed global temperatures. This data were then used to calculate the Seebeck coefficient of the nanowire.

Significantly, we observed clear modulation of the Seebeck coefficient in these PbSe nanowires by field-effect gating. This is, to the best of our knowledge, the first time such field-effect modulation of the Seebeck coefficient is demonstrated at the single semiconductor nanowire level. The observed absolute value for thermoelectric power, S_{abs}, was measured as a function of the gate voltage (and hence PbSe nanowire conductivity) and the magnitude S_{abs} was observed to decrease with increasing sample conductivity, as shown in Figure 27b. Room temperature values for S_{abs} ranged from 64 to 193 $\mu V \cdot K^{-1}$ under high to low V_g, respectively. This represents direct field-effect modulation of the Seebeck coefficient by a factor of 3. The general expression for S is[59,60]

$$S = \frac{k_B}{e} \int \frac{E_F - E}{k_B T} \frac{\sigma(E)}{\sigma} dE \tag{1}$$

where k_B is the Boltzmann constant, e is the electron charge, E_F is the Fermi energy of the material, $\sigma(E)$ is the electrical conductivity at a given electron energy, E, and σ is the total conductivity. Assuming that only electrons contribute to the thermoelectric power and that E_F lies near the conduction band edge (E_c), the above equation can be written as

$$S = \frac{k_B}{e} \left(\frac{E_F - E_c}{k_B T} + A \right) \tag{2}$$

where A represents a scattering factor of the semiconductor[59,61]. Varying V_g changes the electrical conductivity effectively by modulating the electron density in the conduction band and, hence, E_F of the nanowire. Using the general expression of E_F and electron density, eq 2 can be simplified to

$$S = C_1 (\ln N_c - \ln n + A) \tag{3}$$

where C_1 is a fitting parameter, n is the carrier concentration, and N_c is the temperature-dependent effective density of states of the conduction band. Changes in the thermoelectric power via E_F modulation (and hence conductivity), as shown in Figure 27b, closely follow the relation in eq 3. Using the measured electron mobility of 76 $cm^2 \cdot V^{-1} \cdot s^{-1}$ and assuming an effective mass (m_e*) of ~0.05m_0[8], A is estimated to be 1.5. This result is consistent with the value of A in bulk PbSe[49,59], suggesting that electron transport in the nanowire does not differ significantly from that in a classical system.

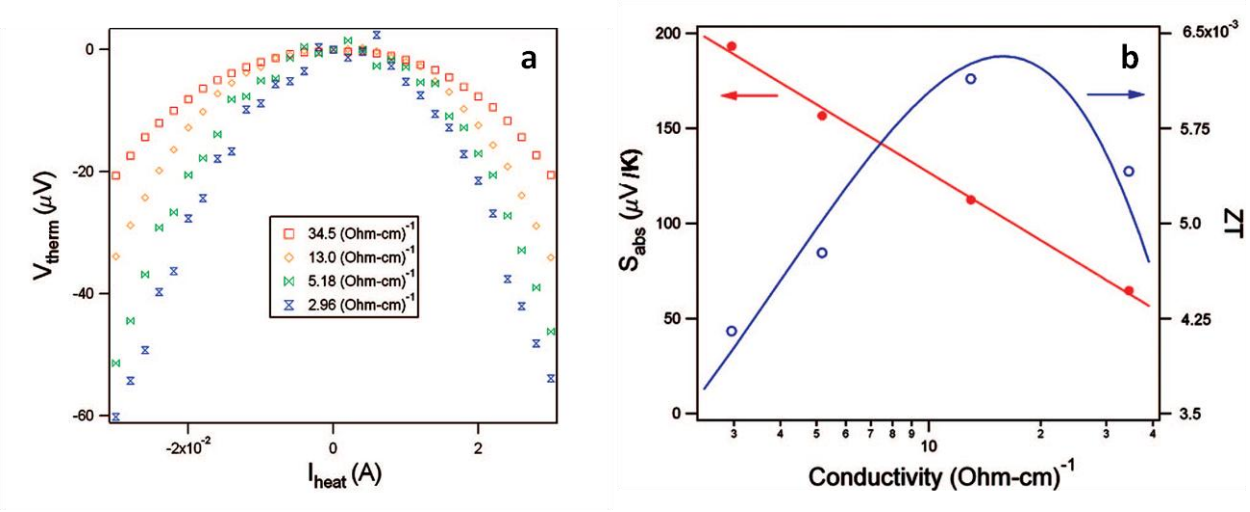

Figure 27 - Thermoelectric power and figure-of-merit of an individual Al_2O_3-coated PbSe nanowire taken at different gate voltages: (a) Thermal voltages of an Al_2O_3-coated PbSe nanowire as a function of heater current taken at various values of nanowire conductivity, as defined by the applied gate voltage. (b) Seebeck coefficient (red) and the estimated room temperature ZT (blue) as a function of the nanowire conductivity, defined by the applied gate voltage.

By combination of the results from the individual nanowire thermoelectric measurements, an estimation can be made for the figure of merit for single gated PbSe nanowires. Figure 27b also plots ZT as a function of electrical conductivity. It was found that there is a maximum in ZT, which occurs around 16 $(\Omega \cdot cm)^{-1}$. Room temperature ZT can be effectively tuned from 0.004 to 0.006, corresponding to changes in S by a factor of 3 and σ by an order of magnitude. More importantly, a net increase of the figure of merit by 50% is achieved through this simple field-effect gating strategy. These results represent the first demonstration of field-effect modulation of the thermoelectric figure of merit in a single semiconductor nanowire and could prove especially important in optimizing the thermoelectric properties of semiconductors where reproducible doping is difficult to achieve. The low figure of merit reported here is clearly the result of a drop in electron mobility from bulk values[31]. Such a reduction may be expected in quasi-one-dimensional materials since the surface-to-volume ratio increases considerably. Optimizing the surface passivation by improved synthetic techniques or surface treatments will undoubtedly improve the transport properties of PbSe nanowires and may yield lead chalcogenide nanowires with superior thermoelectric performance.

2.5.e – Solution-Synthesized PbSe Nanowires: Conclusions

To summarize, PbSe nanowires have been made by a solution-phase synthesis using the oriented attachment mechanism. The nanowire morphology and dimensions were tuned by changing the stabilizer and growth time. Nanowires with branched morphology were used for thermoelectric studies since their rough surfaces can lead to additional phonon scattering.

The thermoelectric properties of these branched PbSe nanowires were studied at the single nanowire level. Both field-effect transport and thermopower measurements showed that the as-made nanowires were p-type semiconductors with near degenerately doped charge carrier concentration. Compared to the bulk, the PbSe nanowires exhibited a similar Seebeck coefficient and a significant reduction in thermal conductivity in the temperature range 20 K to 300 K. Thermal annealing of the PbSe nanowires allowed their thermoelectric properties to be controllably tuned by increasing their carrier concentration or hole mobility. After optimal annealing, single PbSe nanowires exhibited a thermoelectric figure of merit of 0.12 at room temperature

After adding a thin coating of ALD Al_2O_3, the nanowires changed from n-type to p-type, possibility due to gating by a positively charged Al_2O_3 layer. The Al_2O_3 layer stabilized and passivated the surfaces of the nanowires, leading to an increase in air stability and carrier mobility. Using a field-effect gated device, we were able to tune the Seebeck coefficient of the single Al_2O_3-coated PbSe nanowires from 64 to 193 $\mu V \cdot K^{-1}$. This direct electrical field control of σ and S suggests a powerful strategy for optimizing ZT in thermoelectric devices. These results represent the first demonstration of field-effect modulation of the thermoelectric figure of merit in a single semiconductor nanowire. This novel strategy for thermoelectric property modulation could prove especially important in optimizing the thermoelectric properties of semiconductors where reproducible doping is difficult to achieve.

2.5.f – Solution-Synthesized PbSe Nanowires: Follow-up

After the completion of this work numerous advances have been made in the synthesis and thermoelectric efficiency of Pb*X* nanowires. A few notable results are described below.

Talapin et al.[62] and Mokari et al.[63] reported new synthetic procedures for the generation of core/shell and alloy Pb*X* nanowires. PbS and PbTe shells were added to the PbSe nanowires by heating a suspension of nanowires in the presence of Pb and S precursors. Alloys of PbSe and PbS could also be synthesized by using higher growth temperatures relative to that used for shell formation.

Talapin et al. directly aligned solution-synthesized PbSe nanowires across electrodes using a electric field[64]. Although this work was published in 2007 (several years before our work was completed), the alignment methods used in this study are interesting for future measurements. To align the nanowires a small droplet of the solution was first placed on top of the electrodes. By carefully tailoring the electric field and solvent evaporation rate

unidirectional alignment was achieved. The electrical conductivity of the hydrazine-treated 8 nm smooth PbSe nanowires was 100 $(\Omega \cdot cm)^{-1}$, which is similar to the value we obtained in our CVT PbSe nanowires, but 25 times lower than the highest conductivity value achieved for our branched PbSe nanowires prepared using a similar solution synthesis. One significant point about the hydrazine treatment is that is caused a change in polarity form p-type to n-type, similar to our PbSe nanowires after Al_2O_3 coating. The mobility of these nanowires was 9 $cm^2 \cdot V^{-1} \cdot S^{-1}$ which is 3 times greater than that of our un-passivated nanowires, but 20 times lower than that of our PbSe nanowires coated with ALD Al_2O_3. They also demonstrated on chip synthesis of PbSe nanowires via oriented attachment starting with PbSe nanocrystals and an electric field.

Earlier this year Wan et al. reported the Seebeck coefficient of p-type PbS, PbSe, and PbTe nanocube films[2]. The nanocubes were 200-300 nm (PbS), 50-120 nm (PbSe), and 30-60 nm (PbTe). The conductivity of their films (PbS: 0.748 $(\Omega \cdot cm)^{-1}$, PbSe: 1.324 $(\Omega \cdot cm)^{-1}$, PbTe: 0.278 $(\Omega \cdot cm)^{-1}$) was several orders of magnitude lower than the highest value achieved in our single PbSe and PbTe[65,66] nanowires but the electrical conductivity of the PbS nanocube films was similar to that of our CVT-synthesized single PbS nanowires. The Seebeck coefficients of the PbS, PbSe, and PbTe nanocube films were 154.5, 199.9, and 451.1 $\mu V \cdot K^{-1}$, respectively. While the Seebeck value for their PbSe nanocube films was only half of the highest value achieved in our solution-synthesized PbSe nanowires[65], their PbTe nanocube films achieved a Seebeck value approximately 1.7 times higher than that of bulk PbTe[67].

Yang et al. used a lithographically patterned nanowire electrodeposition (LPNE) method to synthesize polycrystalline PbTe nanowire arrays with dimensions of 60 x 200 nm x 200 μm[68]. As-synthesized the nanowires exhibited n-type conductivity. The nanowires had lower carrier concentrations (10^{18} cm^{-3}) compared to our CVT-synthesized p-type PbTe nanowires (10^{19} cm^{-3}). After annealing at 453 K the PbTe nanowires had a Seebeck coefficient of -479 $\mu V \cdot K^{-1}$ at 300 K. Despite the high Seebeck value the thermal annealing also caused a subsequent decrease in the electrical conductivity such that the power factor was lower after annealing. These wires had slightly higher mobililities than that measured in our CVT PbTe nanowires.

Tai et al. reported thermoelectric properties of nanowire films composed of pearl-shaped PbTe nanowires with diameters of 20-40 nm that were synthesized by hydrothermal methods[69]. These nanowires had electrical conductivities of 2.73 $(\Omega \cdot cm)^{-1}$ (50 times lower than our CVT nanowires) and a Seebeck coefficient of 307 $\mu V \cdot K^{-1}$. The same researchers also reported the thermoelectric properties of smooth nanowires with diameters around 30 nm[70]. These PbTe nanowires had lower electrical conductivities (1.33 $\Omega \cdot cm)^{-1}$) but significantly higher Seebeck values of 628 $\mu V \cdot K^{-1}$. The researchers attributed this large increase in thermopower to changes in the electronic density of states as a result of quantum confinement.

It is apparent from these results that steady progress is being made in the field of Pb*X* nanowire thermoelectrics. Significant enhancements have already been achieved enabling reduced thermal conductivities[66] and increased Seebeck coefficients[70]. Continued research promises to bring even more exciting results in the future.

2.6 – Notes

The images in the following figures were reprinted with permission from their respective publishers. Figures 8 – 12 were reprinted from reference [66], copyright 2007 Wiley. Figures 19-24 were reprinted from reference [65], copyright 2009 Springer. Figures 18, 26, and 27 were reprinted from reference [46], copyright 2009 American Chemical Society.

2.7 – References

1. Kittel, C., *Introduction to Solid State Physics*. 7 ed. 1996, New York: John Wiley & Sons, Inc.
2. Wan, B.Y., et al., *Room-temperature synthesis and seebeck effect of lead chalcogenide nanocubes.* Solid State Sciences, 2010. **12**(1): p. 123-127.
3. Schaller, R.D. and V.I. Klimov, *High efficiency carrier multiplication in PbSe nanocrystals: Implications for solar energy conversion.* Physical Review Letters, 2004. **92**(18): p. 186601.
4. Chen, G., et al., *Recent developments in thermoelectric materials.* International Materials Reviews, 2003. **48**(1): p. 45-66.
5. Sootsman, J.R., et al., *Strong reduction of thermal conductivity in nanostructured PbTe prepared by matrix encapsulation.* Chemistry of Materials, 2006. **18**(21): p. 4993-4995.
6. Wang, R.Y., et al., *Enhanced thermopower in PbSe nanocrystal quantum dot superlattices.* Nano Letters, 2008. **8**(8): p. 2283-2288.
7. Harman, T.C., et al., *Quantum dot superlattice thermoelectric materials and devices.* Science, 2002. **297**(5590): p. 2229-2232.
8. Lin, Y.M. and M.S. Dresselhaus, *Thermoelectric properties of superlattice nanowires.* Physical Review B, 2003. **68**(7): p. 075304.
9. Gao, F., et al., *Controlled synthesis of semiconductor PbS nanocrystals and nanowires inside mesoporous silica SBA-15 phase.* Nano Letters, 2001. **1**(12): p. 743-748.
10. Wu, C., et al., *Synthesis and optical properties of ordered 30 nm PbS nanowire arrays fabricated into sulfuric anodic alumina membrane.* Materials Letters, 2006. **60**(29-30): p. 3618-3621.
11. Liu, W.F., W.L. Cai, and L.Z. Yao, *Electrochemical deposition of well-ordered single-crystal PbTe nanowire Arrays.* Chemistry Letters, 2007. **36**(11): p. 1362-1363.
12. Cho, K.S., et al., *Designing PbSe nanowires and nanorings through oriented attachment of nanoparticles.* Journal of the American Chemical Society, 2005. **127**(19): p. 7140-7147.
13. Hull, K.L., et al., *Induced branching in confined PbSe nanowires.* Chemistry of Materials, 2005. **17**(17): p. 4416-4425.
14. Yang, Y., et al., *Synthesis of PbTe nanowire arrays using lithographically patterned nanowire electrodeposition.* Nano Letters, 2008. **8**(8): p. 2447-2451.
15. Lifshitz, E., et al., *Synthesis and characterization of PbSe quantum wires, multipods, quantum rods,and cubes.* Nano Letters, 2003. **3**(6): p. 857-862.
16. Zhang, C., et al., *Synthesis and evolution of PbS nanocrystals through a surfactant-assisted solvothermal route.* Journal of Physical Chemistry B, 2006. **110**(1): p. 184-189.

17. Xu, J., J.P. Ge, and Y.D. Li, *Solvothermal synthesis of monodisperse PbSe nanocrystals.* Journal of Physical Chemistry B, 2006. **110**(6): p. 2497-2501.
18. Zhang, L.Z., et al., *A general in situ hydrothermal rolling-up formation of one-dimensional, single-crystalline lead telluride nanostructures.* Small, 2005. **1**(3): p. 349-354.
19. Dong, L.H., et al., *Surfactant-assisted fabrication PbS nanorods, nanobelts, nanovelvet-flowers and dendritic nanostructures at lower temperature in aqueous solution.* Journal of Colloid and Interface Science, 2006. **301**(2): p. 503-510.
20. Liu, Y.F., et al., *A complex-based soft template route to PbSe nanowires.* European Journal of Inorganic Chemistry, 2003(4): p. 644-647.
21. Ge, J.P., et al., *Orthogonal PbS nanowire arrays and networks and their Raman scattering behavior.* Chemistry-a European Journal, 2005. **11**(6): p. 1889-1894.
22. Law, M., J. Goldberger, and P.D. Yang, *Semiconductor nanowires and nanotubes.* Annual Review of Materials Research, 2004. **34**: p. 83-122.
23. Kuykendall, T., et al., *Complete composition tunability of InGaN nanowires using a combinatorial approach.* Nature Materials, 2007. **6**(12): p. 951-956.
24. Ravich, Y.I., B.A. Efimova, and I.A. Smirnov, *Semiconducting Lead Chalcogenides, Monographs in Semiconductor Physics*, ed. L.S. Stil'bans. Vol. 5. 1970, New York: Plenum.
25. Afzaal, M. and P. O'Brien, *Silica coated PbS nanowires.* Journal of Materials Chemistry, 2006. **16**(12): p. 1113-1115.
26. Zhang, H.X., J.P. Ge, and Y.D. Li, *High-temperature growth of silica sheathed Bi2S3 semiconductor nanowires.* Chemical Vapor Deposition, 2005. **11**(3): p. 147-152.
27. Chiritescu, C., et al., *Ultralow thermal conductivity in disordered, layered WSe2 crystals.* Science, 2007. **315**(5810): p. 351-353.
28. Goldberger, J., et al., *ZnO nanowire transistors.* Journal of Physical Chemistry B, 2005. **109**(1): p. 9-14.
29. Vashaee, D., et al., *Electrostatics of nanowire transistors with triangular cross sections.* Journal of Applied Physics, 2006. **99**(5): p. 054310.
30. Li, D.Y., et al., *Thermal conductivity of individual silicon nanowires.* Applied Physics Letters, 2003. **83**(14): p. 2934-2936.
31. Greig, D., *Thermoelectricity and Thermal Conductivity in the Lead Sulfide Group of Semiconductors.* Physical Review, 1960. **120**(2): p. 358-365.
32. Zhu, J., et al., *Hyperbranched lead selenide nanowire networks.* Nano Letters, 2007. **7**(4): p. 1095-1099.
33. Bierman, M.J., Y.K.A. Lau, and S. Jin, *Hyperbranched PbS and PbSe nanowires and the effect of hydrogen gas on their synthesis.* Nano Letters, 2007. **7**(9): p. 2907-2912.
34. Lau, Y.K.A., et al., *Epitaxial growth of hierarchical PbS nanowires.* Journal of Materials Chemistry, 2009. **19**(7): p. 934-940.
35. Bierman, M.J., et al., *Dislocation-driven nanowire growth and Eshelby twist.* Science, 2008. **320**(5879): p. 1060-1063.
36. Zhu, J., et al., *Formation of chiral branched nanowires by the Eshelby Twist.* Nature Nanotechnology, 2008. **3**(8): p. 477-481.

37. Lau, Y.K.A., et al., *Formation of PbS Nanowire Pine Trees Driven by Screw Dislocations.* Journal of the American Chemical Society, 2009. **131**(45): p. 16461-16471.
38. Morin, S.A., et al., *Mechanism and Kinetics of Spontaneous Nanotube Growth Driven by Screw Dislocations.* Science, 2010. **328**(5977): p. 476-480.
39. Jang, S.Y., et al., *Transport properties of single-crystalline n-type semiconducting PbTe nanowires.* Nanotechnology, 2009. **20**(41): p. 415204.
40. Harman, T.C., D.L. Spears, and M.J. Manfra, *High thermoelectric figures of merit in PbTe quantum wells.* Journal of Electronic Materials, 1996. **25**(7): p. 1121-1127.
41. Roh, J.W., et al., *Size-dependent thermal conductivity of individual single-crystalline PbTe nanowires.* Applied Physics Letters, 2010. **96**(10): p. 103101.
42. Klokkenburg, M., et al., *Dipolar structures in colloidal dispersions of PbSe and CdSe quantum dots.* Nano Letters, 2007. **7**(9): p. 2931-2936.
43. Yong, K.T., et al., *Control of the morphology and size of PbS nanowires using gold nanoparticles.* Chemistry of Materials, 2006. **18**(25): p. 5965-5972.
44. Lu, W.G., et al., *Perfect orientation ordered in-situ one-dimensional self-assembly of Mn-doped PbSe nanocrystals.* Journal of the American Chemical Society, 2004. **126**(45): p. 14816-14821.
45. Hochbaum, A.I., et al., *Enhanced thermoelectric performance of rough silicon nanowires.* Nature, 2008. **451**(7175): p. 163-167.
46. Liang, W.J., et al., *Field-Effect Modulation of Seebeck Coefficient in Single PbSe Nanowires.* Nano Letters, 2009. **9**(4): p. 1689-1693.
47. Abrams, H. and R.N. Tauber, *Thermoelectric Power of Single-Crystal P-Type Pbse.* Journal of Applied Physics, 1969. **40**(9): p. 3868-3870.
48. Shi, L., et al., *Measuring thermal and thermoelectric properties of one-dimensional nanostructures using a microfabricated device (vol 125, pg 881, 2003).* Journal of Heat Transfer-Transactions of the Asme, 2003. **125**(6): p. 1209-1209.
49. Allgaier, R.S. and W.W. Scanlon, *Mobility of Electrons and Holes in Pbs, Pbse, and Pbte between Room Temperature and 4.2-Degrees-K.* Physical Review, 1958. **111**(4): p. 1029-1037.
50. Tang, Y.H., et al., *A simple route to annihilate defects in silicon nanowires.* Chemical Physics Letters, 2000. **328**(4-6): p. 346-349.
51. Small, J.P., K.M. Perez, and P. Kim, *Modulation of thermoelectric power of individual carbon nanotubes.* Physical Review Letters, 2003. **91**(25): p. 256801.
52. Llaguno, M.C., et al., *Observation of thermopower oscillations in the Coulomb blockade regime in a semiconducting carbon nanotube.* Nano Letters, 2004. **4**(1): p. 45-49.
53. Groner, M.D., et al., *Low-temperature Al2O3 atomic layer deposition.* Chemistry of Materials, 2004. **16**(4): p. 639-645.
54. Talapin, D.V. and C.B. Murray, *PbSe nanocrystal solids for n- and p-channel thin film field-effect transistors.* Science, 2005. **310**(5745): p. 86-89.
55. Lin, Y.M. and M.S. Dresselhaus, *Thermoelectric properties of superlattice nanowires.* Physical Review B, 2003. **68**(7): p. 075304.
56. Kosmulski, M., in *Encyclopedia of Surface and Colloidal Science*, A.T. Hubbard, Editor. 2002, Marcel Dekker: New York. p. 1627-1636.

57. Cui, Y., et al., *Doping and electrical transport in silicon nanowires.* Journal of Physical Chemistry B, 2000. **104**(22): p. 5213-5216.
58. Khanal, D.R. and J. Wu, *Gate coupling and charge distribution in nanowire field effect transistors.* Nano Letters, 2007. **7**(9): p. 2778-2783.
59. Fritzsch.H, *General Expression for Thermoelectric Power.* Solid State Communications, 1971. **9**(21): p. 1813-1815.
60. Pernstich, K.P., B. Rossner, and B. Batlogg, *Field-effect-modulated Seebeck coefficient in organic semiconductors.* Nature Materials, 2008. **7**(4): p. 321-325.
61. Brandt, M.S., et al., *Thermopower investigation of n- and p-type GaN.* Physical Review B, 1998. **58**(12): p. 7786-7791.
62. Talapin, D.V., et al., *Synthesis of colloidal PbSe/PbS core-shell nanowires and PbS/Au nanowire-nanocrystal heterostructures.* Journal of Physical Chemistry C, 2007. **111**(38): p. 14049-14054.
63. Mokari, T., et al., *Synthesis of lead chalcogenide alloy and core-shell nanowires.* Angewandte Chemie-International Edition, 2008. **47**(30): p. 5605-5608.
64. Talapin, D.V., et al., *Alignment, electronic properties, doping, and on-chip growth of colloidal PbSe nanowires.* Journal of Physical Chemistry C, 2007. **111**(35): p. 13244-13249.
65. Liang, W.J., et al., *Thermoelectric Properties of p-Type PbSe Nanowires.* Nano Research, 2009. **2**(5): p. 394-399.
66. Fardy, M., et al., *Synthesis and thermoelectrical characterization of lead chalcogenide nanowires.* Advanced Materials, 2007. **19**(19): p. 3047-3051.
67. Heremans, J.P., C.M. Thrush, and D.T. Morelli, *Thermopower enhancement in lead telluride nanostructures.* Physical Review B, 2004. **70**(11): p. 115334
68. Yang, Y.A., et al., *High-Throughput Measurement of the Seebeck Coefficient and the Electrical Conductivity of Lithographically Patterned Polycrystalline PbTe Nanowires.* Journal of Physical Chemistry Letters, 2010. **1**(20): p. 3004-3011.
69. Tai, G.A., W.L. Guo, and Z.H. Zhang, *Hydrothermal synthesis and thermoelectric transport properties of uniform single-crystalline pearl-necklace-shaped PbTe nanowires (vol 8, pg 2910, 2008).* Crystal Growth & Design, 2008. **8**(10): p. 3878-3878.
70. Tai, G., B. Zhou, and W.L. Guo, *Structural characterization and thermoelectric transport properties of uniform single-crystalline lead telluride nanowires.* Journal of Physical Chemistry C, 2008. **112**(30): p. 11314-11318.

Chapter 3:
$M_2O_3(ZnO)_n$ (*M* = In, Ga, Fe) Nanowires

3.1 – Introduction to $M_2O_3(ZnO)_n$ Superlattice Materials

Superlattices contain periodic compositional and structural features, typically on the nanometer scale. Early work discovered that $In_2O_3(ZnO)_n$ superlattice structures arise when ZnO is alloyed with high amounts of In, forming layers of InO_2^- octahedra interspersed between wurtzite layers of doped ZnO (002) with near-perfect periodicity[1,2]. Later work found that the superlattice-forming materials could be generalized to $M_2O_3(ZnO)_n$, where *M* is In, Ga, Fe, and other tri-valent metals, or mixtures such as InGa or InFe[3,4].

The structure of these superlattices has been under intense study since their discovery by Kasper[5] in the 1960's. ZnO is a polar crystal such that in the [001] direction, one end of the crystal is capped by Zn while the opposite end is capped by oxygen. For the remainder of this discussion the Zn side will be referred to as the head while the oxygen side will be referred to as the tail. The O atoms on the edges of the InO_2^- octahedral inclusion layers are each bonded to three In atoms and one metal atom within the $MZn_nO_{(n+1)}^+$ layer[6]. This creates an inversion domain boundary (IDB) in the wurtzite lattice since the Zn-O bonds on either side of the octahedral layer point with the O atoms toward the In layer (tail-to-tail configuration).

The presence of the IDB at the octahedral layer means that the polarity of the ZnO must revert somewhere within the wurtzite $MZn_nO_{(n+1)}^+$ layers to produce the necessary tail-to-tail polarity at the adjacent InO_2^- layer. There are several proposed mechanisms by which the polarity can be reverted[1,6-8]. Yan et al. reported the presence of mirror domain boundaries within the ZnO slabs of their IZO films[1]. An additional layer of In atoms within the $MZn_nO_{(n+1)}^+$ slabs may also act as an IDB. The *M* and Zn atoms within the $MZn_nO_{(n+1)}^+$ layer occupy the tetrahedral or trigonal bipyramidal sites[2,9], and those with 5-fold coordination may be ordered in either flat layers or zigzag layers[6,8,10]. Using density functional theory (DFT) calculations Yan et al. and Da Silva et al. compared the relative energies of these two structures and found that the zigzag modulated structure is more stable for a number of reasons. Firstly, in the zigzag layer, O has an energetically favorable tetrahedral coordination, while in the flat layer O has a coordination of three[8]. Also, the occupation of the trigonal bipyramidal sites within the wurtzite lattice can cause local lattice distortions and strain within the $MZn_nO_{(n+1)}^+$ slabs. This strain can be reduced by localizing the atoms with trigonal bipyramidal coordination to one boundary. The zigzag layer was found to most effectively reduce this strain[6,8]

The unique structure of these $M_2O_3(ZnO)_n$ materials has led to an array of interesting properties that are exciting for a variety of applications. Some of the most promising

applications are thermoelectrics and photoelectrochemical water splitting, which will be discussed in the following sections.

3.2 – Thermoelectric Applications of $M_2O_3(ZnO)_n$ Superlattices

Traditional thermoelectric materials, such as the lead chalcogenides discussed in the previous chapter, cannot be used in high temperature (T>1000°C) applications, especially industrial applications, such as steel production, due to instability and oxidation issues. In fact, PbTe melts at 924°C. Some metal oxide semiconductors, on the other hand, possess high temperature stability. For example, ZnO doesn't decompose until 1975°C. Thus, the development of oxide semiconductors for thermoelectric applications is important for the capture of waste heat in high temperature processes. Unfortunately most metal oxide materials, including ZnO have a very low figure of merit (ZT on order of 10^{-3} for ZnO[11]). While high-temperature ZT values are important in oxide materials, the discussion in this section will focus on the thermoelectric properties at temperatures close to 300 K. Since single-nanowire measurement techniques (as reported in Chapter 2) are limited to lower temperatures (T>300 K), these lower temperature values are more relevant to our results.

While ZnO can exhibit a relatively high intrinsic electrical conductivity due to formation of oxygen vacancies acting as donor states, the introduction of slight amounts of Al, In, or Ga can further increase the conductivity when substituted for Zn[12]. Previous reports have shown an enhancement in the ZT of doped ZnO[11,13]. Tsubota et al. achieved at ZT of approximately 0.02 at 300 K with 5.0% doping of Al[13]. While the doping enabled an increase in the power factor (due to an increase in electrical conductivity) the relatively high thermal conductivity of 35 $W \cdot m^{-1} \cdot K^{-1}$ made it difficult to achieve a high thermoelectric efficiency[11,13]. More recently, Ohtaki et al. achieved a ZT of ~0.04 at 300 K for dually doped ZnO with the composition $ZnAl_{0.02}Ga_{0.03}O$[14].

Superlattice structures can lead to decreases in thermal conductivity by effectively scattering phonons. The family of $M_2O_3(ZnO)_n$ superlattice materials are especially promising for thermoelectric applications since they offer both a high level of doping as well as numerous interfaces to scatter phonons. In 1996 Ohta et al. reported the thermoelectric properties of $In_2O_3(ZnO)_n$[15]. As was the case for doped ZnO, compared to un-doped ZnO, the $In_2O_3(ZnO)_m$ exhibited an increase in the electrical conductivity and a decrease in the Seebeck coefficient. However, as opposed to the doped ZnO, with the introduction of the superlattice structure the thermal conductivity of $In_2O_3(ZnO)_n$ materials decreased with increasing n to around 3.4 $W \cdot m^{-1} \cdot K^{-1}$ at 500 K for n=9. This resulted in a ZT of ~0.01 at 500 K for bulk $In_2O_3(ZnO)_9$. Unfortunately, despite the drastic decrease in thermal conductivity, this efficiency is lower than that of the doped ZnO due to a lower electrical conductivity and Seebeck coefficient. Since this first report, several other studies have been published on the thermoelectric properties of ZnO-based superlattices. One notable report is that from Kaga et al. in 2004 on highly textured Ca-doped $In_2O_3(ZnO)_n$[16]. With 2.5% Ca doping they were able to achieve at ZT of ~0.05 at 550 K.

As was discussed in Chapter 1, nanowires can often exhibit enhanced thermoelectric efficiencies as a result of a decrease in thermal conductivity and the possible introduction of quantum confinement. The combination of a superlattice structure and a single crystal nanowire could generate the ideal phonon-scattering and charge-transporting structure, and hence a better thermoelectric material.

3.3 – Photoelectrochemical Water Splitting Applications of $M_2O_3(ZnO)_n$ Superlattices

$M_2O_3(ZnO)_n$ superlattices are also potential materials for photoelectrochemical water spitting applications. Since their optical properties are similar to that of ZnO, it is likely that they have the same or similar band alignments, giving them the proper band positions for both water oxidation and H^+ reduction. Pure ZnO cannot be used for water splitting since it is unstable under water splitting conditions. In fact, ZnO is unstable in aqueous solutions no matter whether or not it is being illuminated. With the addition of the In-O octahedral inclusions, however, it is possible that the stability may be improved. Also, the high level of doping within the superlattice materials may lead to superior electrical properties for water splitting.

In 1998 Kudo et al. reported H_2 and O_2 production under visible light irradiation using an $In_2O_3(ZnO)_n$ photocatalyst[17]. Although the H_2 an O_2 evolution was in the presence of sacrificial reagents, it presented $In_2O_3(ZnO)_n$ as a promising material for overall water splitting. Another important thing to note is that the $In_2O_3(ZnO)_n$ samples generated H_2 and O_2 in aqueous solutions without any apparent degradation in photocatalytic activity for 13 hours. This indicates that the superlattice materials do indeed have superior stability compared to the parent ZnO. Kudo et al. also reported a large shift in the band gap of $In_2O_3(ZnO)_n$ compared to ZnO with energies as low as 2.6 eV for n=3. By pushing the bandgap towards smaller, visible wavelengths, it's possible to harness more of the sun's energy, enabling higher water splitting efficiencies.

It would be especially interesting to test the water splitting properties of $M_2O_3(ZnO)_n$ nanowires. Nanowires can act as high-surface-area platforms for solar water splitting, leading to better charge separation. The combination of the nanowire morphology with improved stability and enhanced visible absorption presents $M_2O_3(ZnO)_n$ nanowires as attractive materials for photoelectrochemical water splitting.

3.4 – $M_2O_3(ZnO)_n$ Superlattice Nanowires

In 2004 Jie et al. reported the first synthesis of $In_2O_3(ZnO)_n$ superlattice nanowires[18]. The spacing between In-O octahedral layers was not constant, so these nanowires are more accurately described as polytypoids rather than superlattices. The $In_2O_3(ZnO)_n$ (average n = 18) nanowires were synthesized by chemical vapor transport of ZnO, In_2O_3, and Co_2O_3 powders

using the VLS mechanism. Most of the nanowires grown by this process were In-doped ZnO while only 20-40% exhibited a superlattice structure. The In-O octahedral layers in the superlattice nanowires were always perpendicular to the [001] direction, but both longitudinal and transverse superlattices were formed by accessing nanowires with different growth directions. In addition to the In-O octahedral layers, zigzag modulated structures were observed. As a result of the In doping, the nanowire substrates exhibited a red-shifted PL. However, due to the inhomogeneity in the nanowire substrates it was difficult to attribute this optical property to a specific structure.

Similar synthetic procedures have been reported by other groups[19-21]. In contrast to the first report, these synthetic procedures achieved superlattice yields of around 90% making global characterization techniques more indicative of the superlattice properties. Most of the $In_2O_3(ZnO)_n$ nanowires showed a red shift in the PL[20,21]. Also, while ZnO nanowires usually have a PL peak in the visible due to oxygen defects, the superlattice nanowires showed no such emission[19-21].

$InGaO_3(ZnO)_3$ and $InGaO_3(ZnO)_5$ nanowires with perfect superlattice structures were synthesized by CVT in 2009 by Li et al[22]. As a result of the true superlattice structure these nanowires showed a monoclinic (*n*=odd) XRD pattern rather than the wurtzite ZnO pattern observed in the previously reported $In_2O_3(ZnO)_n$ nanowires. Hsu et al. also reported the synthesis of ZnO nanowires doped with Ga[23]. Although the XRD patterns of the nanowires show some percentage of the $ZnGa_2O_4$ spinel structure, a TEM image of one of the nanowires looks very similar to that of other $M_2O_3(ZnO)_m$ superlattices with presence of stacking faults and inversion domain boundaries. It's likely that some sections of the nanowires were $Ga_2O_3(ZnO)_m$ while other sections were $ZnGa_2O_4$. When the level of *M* doping gets close to 60% there is a very fine line between the superlattice structure and the spinel structure. Earlier this year Huang et al. published the first report of $InAlO_3(ZnO)_n$ superlattice nanowires[24] expanding the library of confirmed $M_2O_3(ZnO)_n$ superlattice nanowires to include $In_2O_3(ZnO)_n$, $InGaO_3(ZnO)_n$, and $InAlO_3(ZnO)_n$.

3.5 – $M_2O_3(ZnO)_n$ Nanowires Synthesized by Solid-State Diffusion (I)

Although, the previous CVT methods were successful in generating superlattice nanowires, it remains difficult to achieve rational control over material properties, such as nanowire diameter and dopant concentration, in addition to maintaining a high yield of superlattice wires. It's likely that the nanowires could also be synthesized by a conversion approach. Since the $M_2O_3(ZnO)_n$ structure is the thermodynamic structure for *M*-doped ZnO at certain temperatures and compositions, it should be possible to introduce the dopants into the parent ZnO lattice using a solid state diffusion approach, effectively converting pure ZnO into the $M_2O_3(ZnO)_n$ superlattice.

3.5.a - Synthesis of $M_2O_3(ZnO)_n$ Nanowires by Solid-State Diffusion (I)

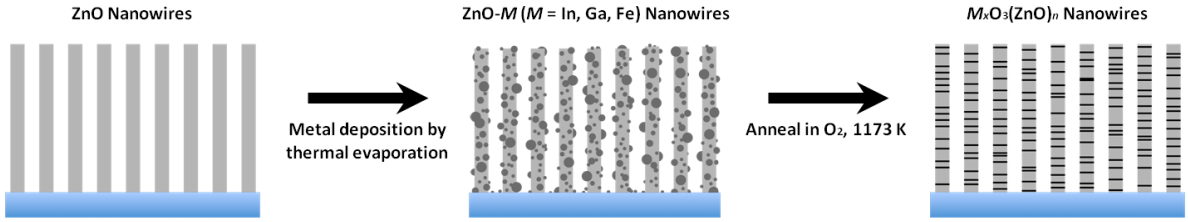

Figure 28 - $M_2O_3(ZnO)_n$ Thermal Evaporation Synthesis Schematic: Schematic illustration of the solid-state diffusion synthesis of $M_2O_3(ZnO)_n$ alloy nanowires via thermal evaporation methods

Utilizing a three-step, solid-state diffusion process shown schematically in Figure 28, we present a novel conversion method for producing $M_2O_3(ZnO)_n$ alloy nanowires that allows for a high level of control in manipulating material composition, structure, and properties.

First, ZnO nanowires were grown on double-polished *a*-plane (110) sapphire substrates by a Au-catalyzed CVT process[25]. Sapphire substrates were diced into 2 mm x 2 mm pieces and thoroughly clean by sonication in acetone for 1 hour. A thin layer of Au (~3 nm) was sputtered onto the substrates and the substrates were annealed in air at 1223 K for 1 min to melt the Au thin film, causing it to bead up into small Au nanoparticles. ZnO and C (1:1 ratio by weight) powders were mixed using a motor and pestle and loaded into a small alumina boat. One Au-coated sapphire substrate was placed on the downstream end of the boat on top of the ZnO/C precursor. The boat was inserted 4 cm inside a 0.5-inch diameter quartz tube and this tube was placed inside a 1-inch diameter quartz tube. The tubes were loaded into a tube furnace such that the front of the alumina boat was downstream from the center of the furnace (Figure 29). The tube was sealed with ultra-torr fittings and purged with a flow of 6.8 sccm of 10% O_2 balance Ar and 76 sccm Ar. The furnace was rapidly heated to 1173 K and kept there for a growth time of 15 min. Typical nanowires had diameters of 80-130 nm and lengths of 10-15 µm and grew along the [002] direction.

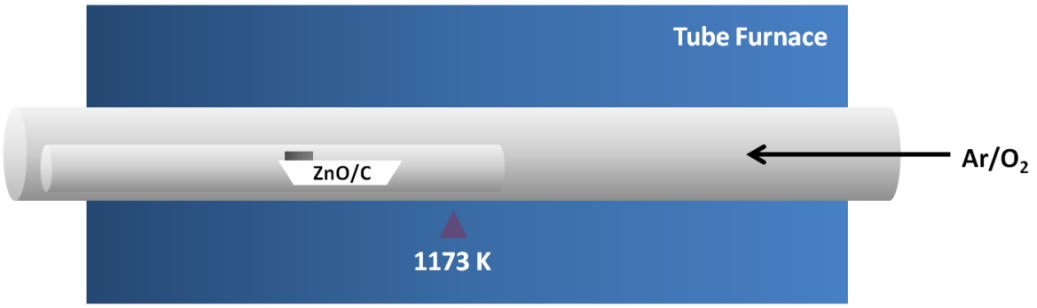

Figure 29 – ZnO Nanowire Synthetic Setup: Schematic Illustration of the setup used for the synthesis of ZnO nanowires

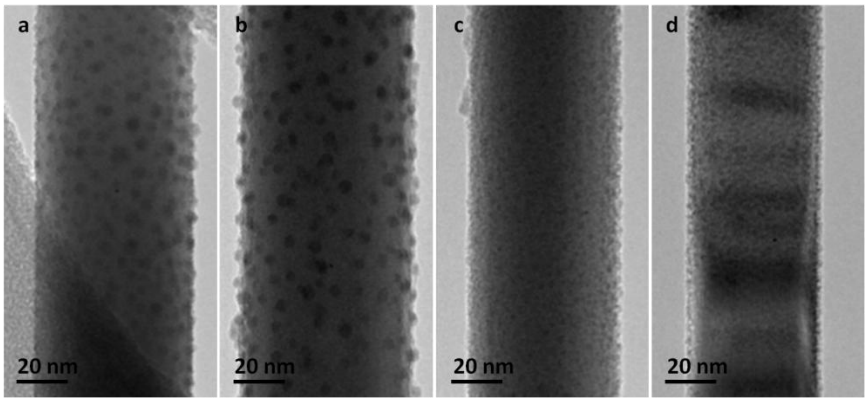

Figure 30 – Metal Coated Nanowires: ZnO nanowires coated with (a) 5 nm of In and 5 nm of Ga, (b) 10 nm of In, (c) 10 nm of Ga, and (d) 5 nm of In and 5 nm of Fe.

Next, the as-grown [002]-oriented ZnO nanowire arrays were coated with mixtures of In, Ga, and Fe using a home-built thermal evaporation system. The thickness of evaporated metal was measured by a quartz crystal monitor. By monitoring the thickness of the deposited metal it was possible to generate reproducible alloy concentrations and control metal ratios in mixed depositions. TEM images taken of the nanowires after metal deposition show a coating of metal nanoparticles on the surfaces of the nanowires (Figure 30). The metal-coated ZnO nanowire substrates were loaded into the center of a 1-inch diameter quartz tube and heated in a tube furnace under a pure O_2 atmosphere at 1173 K for 12-96 hours to form arrays of polytypoid alloy nanowires. The superlattice structure remained no matter how long the nanowires were annealed, indicating that the structure is thermally stable. For metal loadings greater than 20 nm, samples were prepared using successive coating/annealing cycles. This method has been applied successfully to synthesize nanowires of IZO, IGZO, gallium zinc oxide (GZO, $Ga_2O_3(ZnO)_n$), and indium iron zinc oxide (IFZO, $In_{2-x}Fe_xO_3(ZnO)_n$). In this work, samples are referred to by the thickness of the metal coating, rather than the chemical formula, due to the natural distribution of nanowire diameter (affecting concentration) and the polytypoid nature of the nanowires.

3.5.b - Structural Analysis of $M_2O_3(ZnO)_n$ Nanowires (I)

The $M_2O_3(ZnO)_n$ nanowires were carefully examined to elucidate their structures. While general characterization (XRD, SEM, EDS, TEM) was performed on each $M_2O_3(ZnO)_n$ nanowire system, it's expected that all the systems have similar structures. For simplicity, the IGZO nanowire system was chosen for in-depth studies and is the main focus of the structural characterization presented in this work.

Figure 31 shows XRD patterns taken from IGZO nanowires prepared using varying amounts of In and Ga metal deposition. Ths XRD patterns were collected using a Bruker D8 Advance diffractometer with Cu k_α irradiation. The strong 002 peak in the IGZO pattern indicates that the nanowire array maintained a vertical orientation after the conversion. No In_2O_3 or Ga_2O_3 peaks were observed in the IGZO sample made using 10 nm of In and 10 nm of Ga (10/10) deposition, but the weak unidentified peaks in the 40/40 IGZO sample may belong to an alloy of indium and gallium oxide. In the IGZO nanowire alloys, there is little shift from the position of the ZnO nanowire diffraction peaks, but peak broadening towards smaller angles

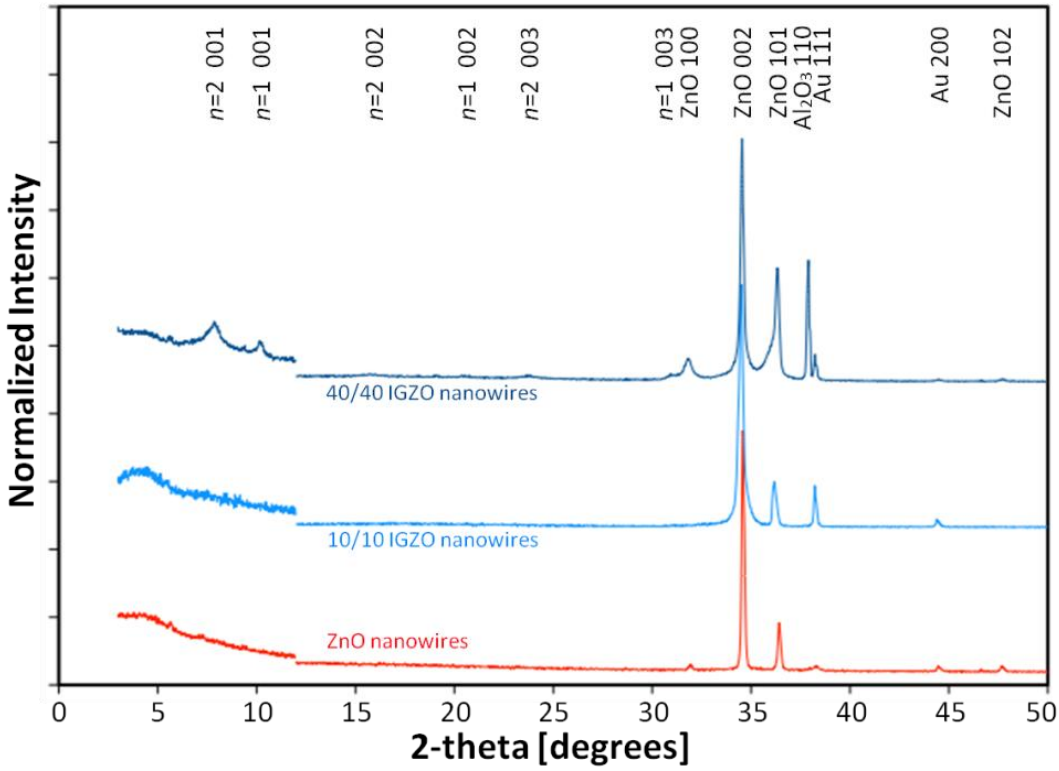

Figure 31 – XRD Patterns of IGZO Nanowires: XRD patterns (Cu k_α irradiation) of ZnO nanowires (bottom) and IGZO nanowires prepared with 10/10 (middle) and 40/40 nm (top) of In and Ga metal deposition. Longer acquisition times were used below 12° for better signal to noise and thus were normalized separately from the rest of the pattern.

is observed, suggesting the formation of non-uniform alloys. New peaks appear in the low-angle region (<10°) for the 40/40 IGZO sample, corresponding to spacings of 0.86 and 1.12 nm, which are in good agreement with the predicted lattice constants for $M_2O_3(ZnO)_n$ with n=1 and n=2[6]. In addition, we observe higher-order peaks for n=1 and n=2 in the 15-32° range.

The solid-state diffusion process used to generate the polytypoid $M_2O_3(ZnO)_n$ nanowires maintains the original morphology of the nanowire array and no etching is observed, as seen in the SEM images taken before (Figure 32a) and after (Figure 32b) alloy formation. SEM images were collected using a JEOL JSM 6340F field-emission SEM operating at 5 kV. The $M_2O_3(ZnO)_n$ nanowires made in this study typically have diameters around 80-130 nm and lengths of 10-15 µm, as determined by the dimensions of the starting ZnO nanowires[25].

TEM images of 10/10 IGZO nanowires (Figure 33 a-c) show a modulation in contrast along their longitudinal axis, which can be attributed to a superlattice structure. According to previous reports, the superlattice structure consists of planes of InO_2^-octahedra separated by slabs of wurtzite $MZn_nO_{(n+1)}^+$ (M = In, Ga)[2]. EDS confirms the presence of In, Ga, and Zn in the IGZO nanowires (Figure 33d), with an In:Ga atomic ratio of approximately 1:1. The relative amounts of In and Ga compared to Zn varies depending on the diameter of the starting ZnO nanowire. The TEM images in this study were taken using the following TEMs: a Tecnai G2 S-Twin TEM operating at 200 kV, a Technai F20 UT TEM operating at 200 kV, a Philips CM200/FEG TEM operating at 200 kV and a JEOL JEM-2100 LaB_6 TEM operating at 200 kV. Elemental

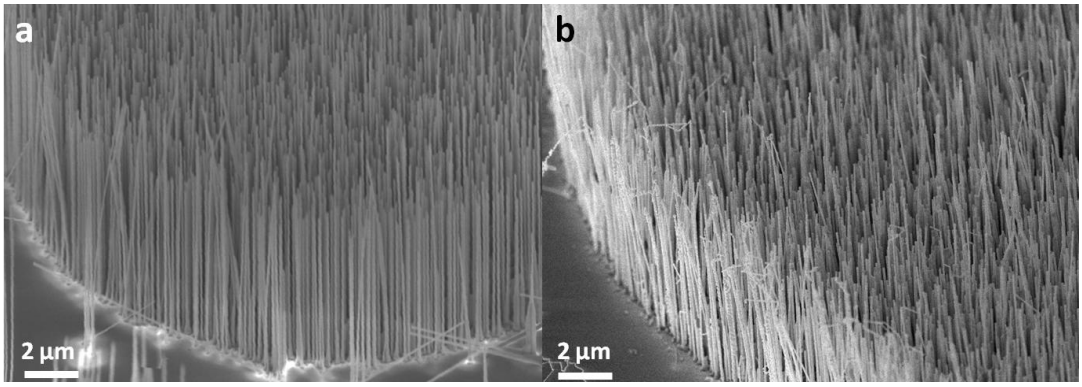

Figure 32 – SEM images of ZnO and IGZO nanowire arrays: SEM images of arrays of (a) as-grown ZnO nanowires and (b) IGZO nanowires prepared with 5/5 nm In/Ga deposition

analysis was performed on a Hitachi H-7650 TEM operating at 120 kV equipped with an EDAX EDS.

Similar superlattice structures were observed in the IZO, GZO, and IFZO nanowire systems (Figure 34). Compared to the other systems, the IGZO nanowires display the highest inclusion and dopant density and are considered to be the most promising material for thermoelectric applications.

To confirm the structure of our nanowires, Z-contrast scanning transmission electron microscopy (STEM) imaging was done using the transmission electron aberration-corrected microscope (TEAM) 0.5, which consists of a modified FEI Titan 80-300 microscope equipped with a special high-brightness Schottky-field emission electron source, a gun monochromator, a high-resolution GIF Tridiem energy-filter, and two CEOS hexapole-type spherical aberration correctors, all of which enable 50 pm resolution. The TEAM 0.5 has a HAADF STEM detector and was operated at 300 kV. In Z-contrast images, the intensity is approximately proportional to the mean square of the atomic number of the constituent atoms. Thus, using Z-contrast

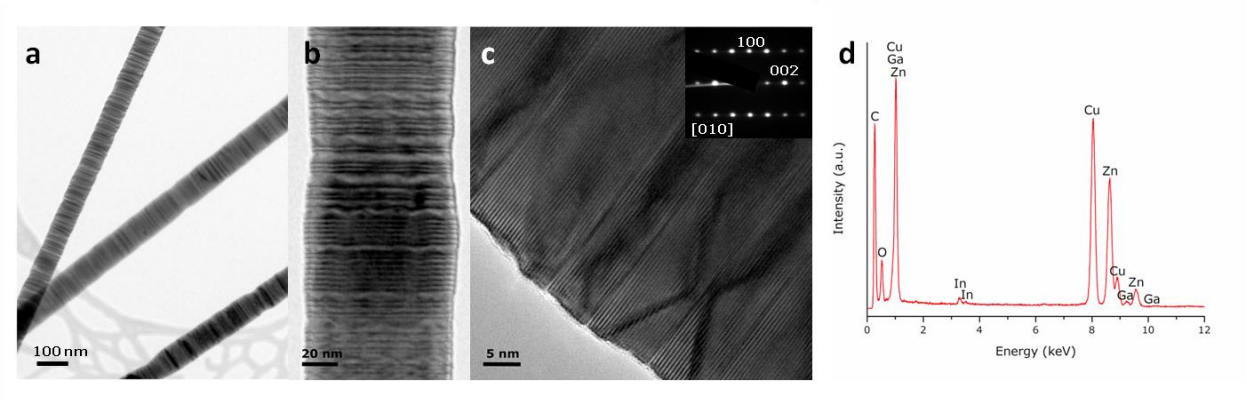

Figure 33 – TEM and EDS of IGZO Nanowires: TEM images (a,b,c) and EDS spectrum (d) of IGZO nanowires prepared by coating ZnO nanowires with 10 nm of In and 10 nm of Ga and annealing at 1173 K in oxygen for 12 hours. The In:Ga ratios were approximately 1:1 by EDS in all the nanowires. For example, in one of the 110 nm 10/10 IGZO nanowires, the atomic percentages of In, Ga, and Zn were 6.3, 6.0, and 87.7, respectively.

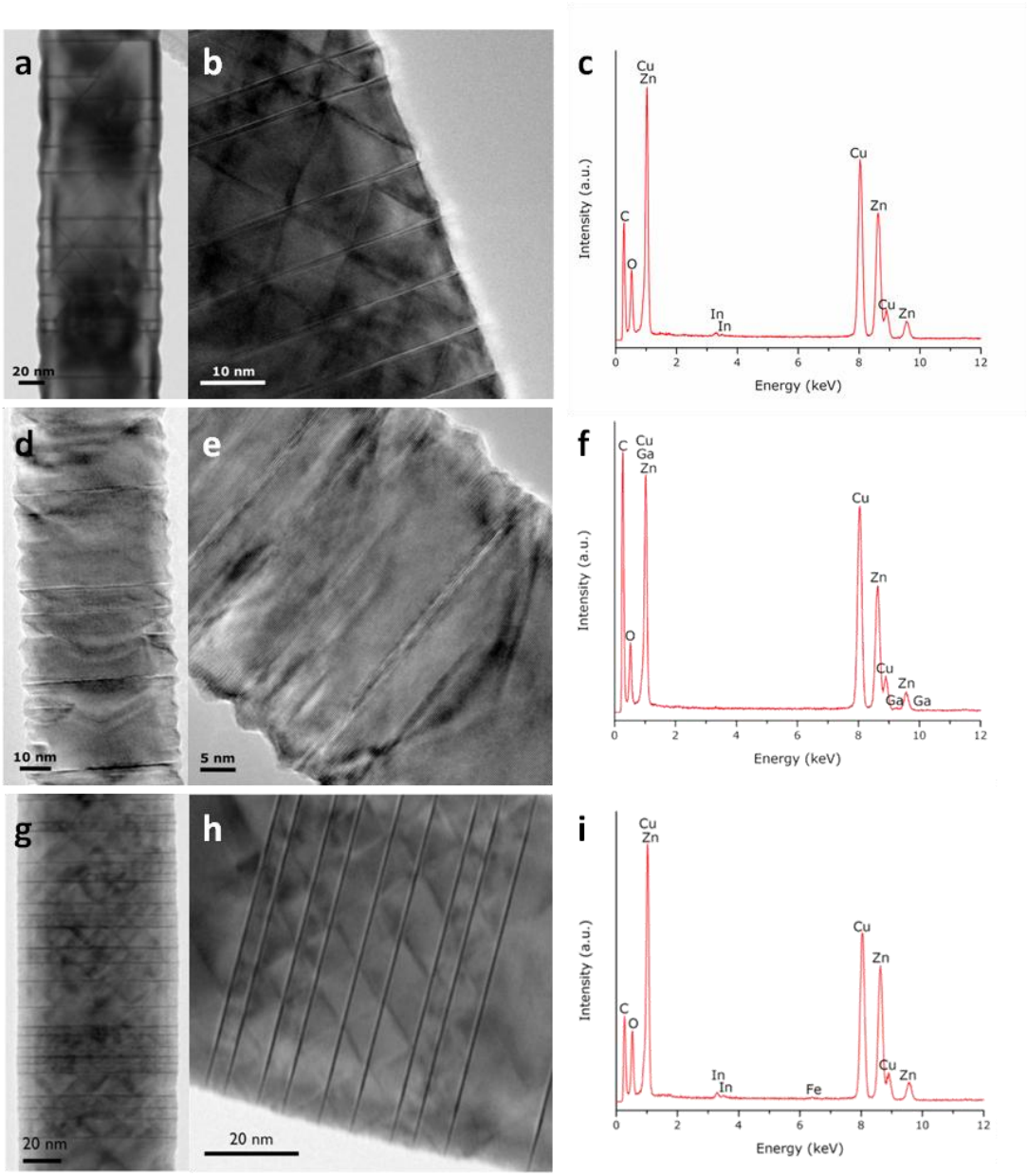

Figure 34 – TEM and EDS of IZO, GZO, and IFZO Nanowires: TEM images and EDS spectra of (a-c) IZO nanowires prepared with 15 nm of In, (d-f) GZO nanowires prepared with 10 nm of Ga, and (g-i) IFZO nanowires prepared with 5 nm of In and 5 nm of Fe. All nanowires were annealed at 1173 K in oxygen for 12 hours. TEM images indicate the presence of octahedral layers and zigzag structures.

imaging, the position of In (Z = 49) can be unambiguously determined, but Ga (Z = 31) and Zn (Z = 30) cannot be distinguished from one another since their atomic numbers differ by only one. Oxygen cannot be imaged due to its relatively small atomic number. Figure 35a is a Z-contrast image of a 10/10 IGZO nanowire clearly showing the presence of In-enriched layers (brightest lines) oriented perpendicular to the [002] direction. As observed in the high-resolution (HR)-STEM image in Figure 35b, the In atoms sit on individual planes and are separated by wurtzite $M\mathrm{Zn}_n\mathrm{O}_{(n+1)}^{+}$ slabs of varying thickness. Only single layers of In atoms were observed in the

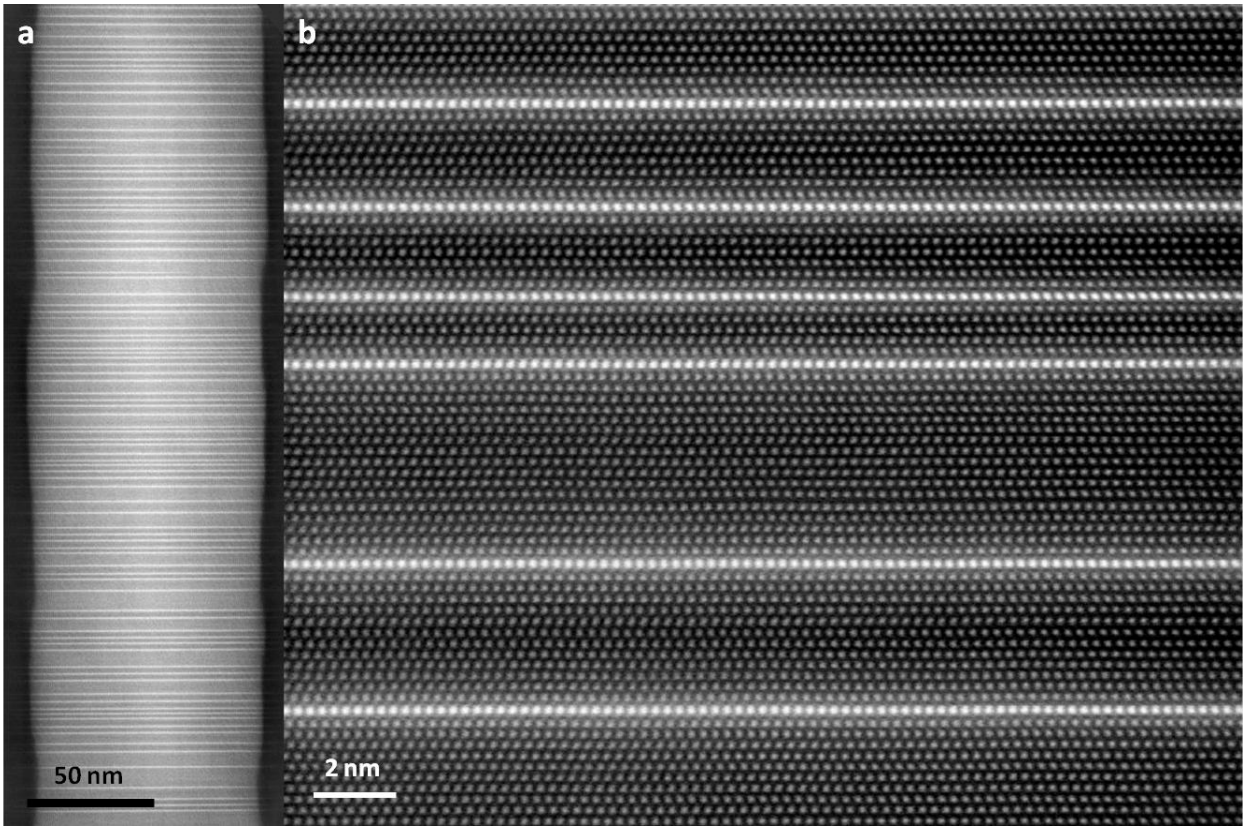

Figure 35 – Z-contrast STEM Images of IGZO Nanowires: (a) Z-contrast STEM image of a 10/10 IGZO nanowire. The Z contrast in the image clearly shows that In atoms are preferentially located within layers oriented perpendicularly to the nanowire growth direction. (b) HRSTEM image of an IGZO nanowire showing individual MO_2^- layers sandwiched between multiple $MZn_nO_{(n+1)}^+$ layers.

10/10 IGZO nanowires, consistent with the layers being composed of octahedrally-coordinated InO_2^-, which has been shown to be the most stable configuration for In within the superlattice structure[6].

An EDS map was taken on an IGZO nanowire using a using a JEOL JEM-2100-F field emission analytical TEM operating at 200 kV with a HAADF STEM detector and an Oxford EDS. The elemental maps (Figure 36) show a concentration of In within the octahedral inclusions. While Ga is more evenly spread across the nanowire there is also an enrichment of Ga within the octahedral layer indicating that their true composition is $In_{1-x}Ga_xO_2^-$. As expected, the Zn map shows a lack of Zn in the octahedral inclusions and the O is evenly spread around the nanowire.

Upon examination of the HR-STEM images, it is apparent that the MO_2^- inclusion layer is also associated with a stacking fault, which together with the IDB produces an AaBbAaB**bAc**CaAcCaA (capital and lowercase letters correspond to metal and oxygen atoms, respectively) stacking sequence in which the wurtzite lattice on one side of the In/Ga layer is translated by ⅓<100> (Figure 37). The location of the octahedral MO_2^- within the stacking sequence is denoted by the bold **bAc**.

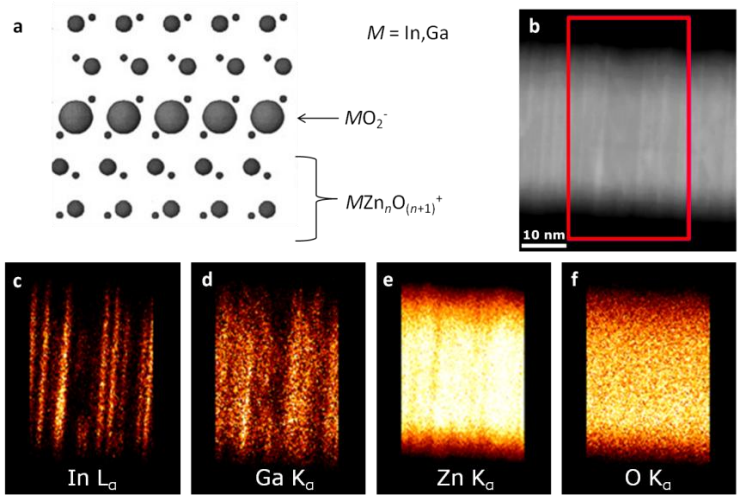

Figure 36 - Elemental mapping on an IGZO nanowire: (a) Structure model showing the octahedral inclusion and wutzite ZnO slabs in the superlattice structure. (b) STEM image of an IGZO nanowire and the corresponding EDS element maps for (c) In, (d) Ga, (e) Zn, and (f) O.

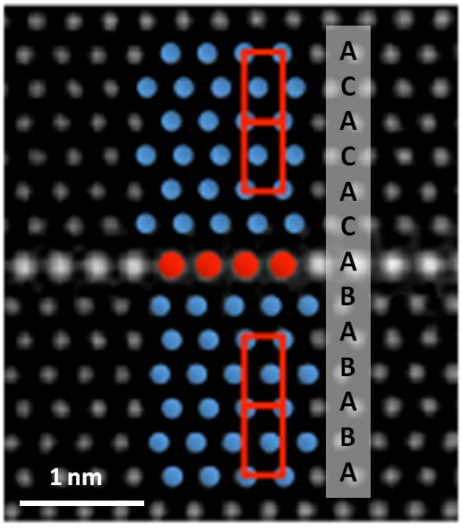

Figure 37 – Stacking Fault: HRSTEM image highlighting the change in stacking sequence across a MO_2^- layer.

Zigzags were seen in all four types of alloys synthesized in this study (Figures 33 and 34), but were not apparent in those alloys with small *n*. Also, since the trigonal bipyramidal sites may be occupied by In, Ga, or Zn atoms in the IGZO nanowires, the zigzags appear faint in the Z-contrast images and in some cases are not discernable. A previous report observed that zigzags are only present in superlattices with $n>6$[9]. The lattice strain caused by a flat layer of trigonal bipyramidally coordinated In/Ga atoms decreases as the thickness of the $MZn_nO_{(n+1)}^+$ slabs decreases, so the energy difference between the flat and zigzag configurations decreases with decreasing *n*[6]. Therefore, it is conceivable that the polarity of the $MZn_nO_{(n+1)}^+$ layers with small *n* may be reversed via a flat layer of trigonal bipyramidal atoms.

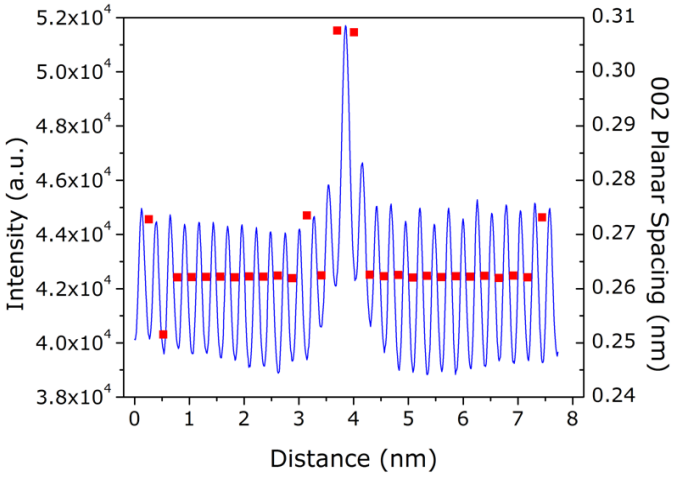

Figure 38 – *d* spacings: Intensity line profile and *d* spacing across a MO_2^- layer taken from a HRSTEM image. On either side of the inclusion, the *d* spacing shows an expansion of ~17% relative to that of pure ZnO.

In agreement with XRD, the *d* spacings in the $MZn_nO_{(n+1)}^+$ layers (Figure 38) are unchanged from (002) in pure ZnO (0.26_2 nm), but the octahedral MO_2^- planes force a local 17% increase in the *d* spacing (0.30_7 nm) on either side of the inclusion layers (subscripts denote numbers beyond the significant figures). The *d* spacings were determined by taking an intensity line profile across an In/Ga inclusion in a HRSTEM image and measuring the distance between peaks. This change in *d*-spacing on either side of

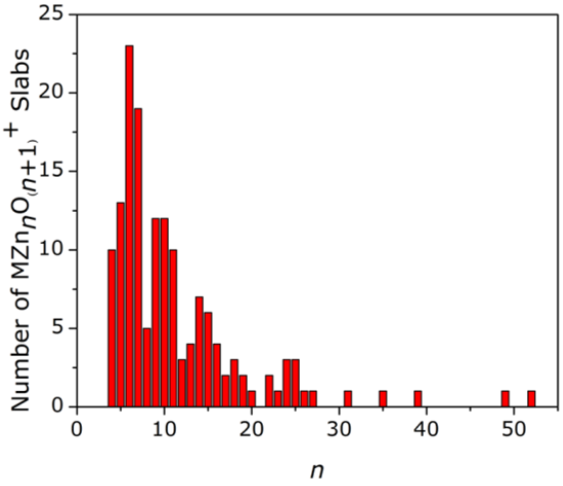

Figure 39 – *n* values: Frequency of different *n* values of the $MZn_nO_{(n+1)}^+$ layers measured from HRSTEM images of several 10/10 IGZO nanowires.

the In/Ga inclusions corresponds with that reported by Yan et al. and Jie et al. on IZO[1,26]. This significant increase in *d* spacing around the inclusion layer is associated with a large amount of lattice strain.

To approximate an *n* value for the 10/10 IGZO nanowires, the number of atomic layers in each $MZn_nO_{(n+1)}^+$ slab was counted for several nanowires (Figure 39). The average *n* is 11, but the most frequent is 6. Some *n* values, such as *n* = 8, are only represented by a small number of $MZn_nO_{(n+1)}^+$ slabs. The reason for this is presently unknown and requires further study. *n* can be related to the spacing (ℓ) between MO_2^- layers by the following equation:

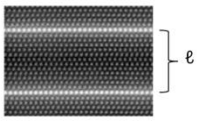

$$\ell\ (\text{nm}) = 0.61_4 + 0.26_2\ n$$

where 0.61_4 nm corresponds to twice the distance of the *d* spacing immediately adjacent to the MO_2^- octahedral layers and 0.26_2 nm corresponds to the (002) planar spacing within the $MZn_nO_{(n+1)}^+$ slabs. Using this equation, the average spacing between MO_2^- octahedral layers in the 10/10 IGZO nanowires is 3.50 nm and the most frequent is 2.19 nm.

The amount of metal deposition was varied to determine its effect on MO_2^- layer density (Figure 41, a-d). The surface of the 40/40 IGZO nanowire shown in Figure 41d appears rough due to the presence of oxide particles left over after the solid-state diffusion process. However, most IGZO nanowires in the sample did not show surface particles. Line intensity profiles drawn perpendicular to the MO_2^- inclusions were used to generate power spectra (Figure 41, e-h) from the nanowires shown in Figure 41, a-d. The power spectra show the most common frequencies (1/ℓ) within the nanowires, providing information regarding the MO_2^- layer spacings and the periodicity of the spacings. As the thickness of metal deposition is increased the most common frequencies shift to higher 1/ℓ (smaller ℓ) indicating that the distance between MO_2^- layers decreases with increased metal deposition. The periodicity also increases with metal deposition, which can be seen in the

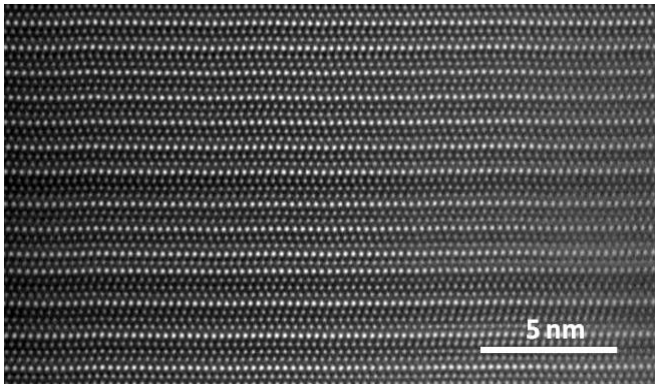

Figure 40 - 40/40 IGZO nanowires: Z-contrast STEM image showing a high density of inclusions layers with spacings corresponding to n=2 and n=1.

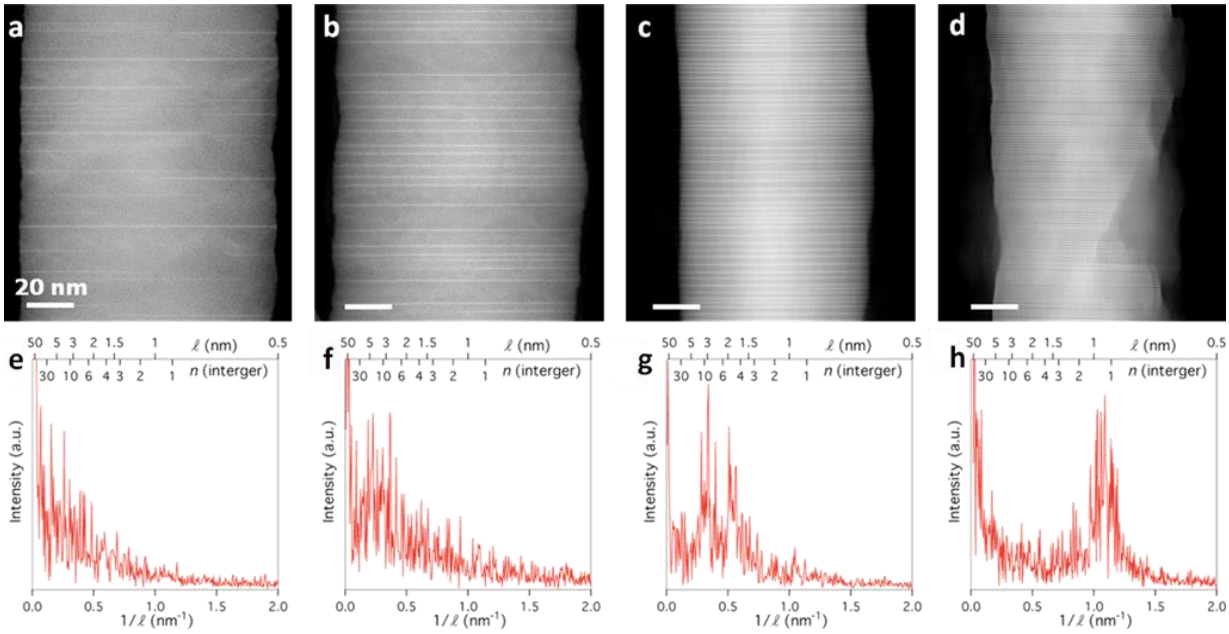

Figure 41 - Atomic-level control: (a-d) Z-contrast STEM images of IGZO nanowires prepared with 10, 20, 40, and 80 nm of metal (1:1 In:Ga by film thickness), respectively. (e-h) Power spectra generated using line intensity profiles drawn along the length of the nanowires showing the frequency of reciprocal distance between MO_2^- layers for (a-d). The distance between MO_2^- layers decreases with increasing thickness of metal deposition. The periodicity of the MO_2^- layer spacings also improves.

emergence of distinct peaks, such as in Figure 41g and 41h. The frequencies obtained from the 10/10 power spectrum match the *n* values that were directly counted in Figure 39. As seen in Figure 41h, the majority of MO_2^- layers in the 40/40 IGZO are separated by 2 or 3 layers of $MZn_nO_{(n+1)}^+$, which is supported by the low-angle XRD pattern (Figure 31) and the HRSTEM image taken from a nanowire in the same 40/40 IGZO nanowire sample (Figure 40). It is evident from these power spectra that both *n* and the superlattice periodicity can be controllably tuned by adjusting the amount of metal deposition.

3.5.c - Mechanism of Superlattice Formation in $M_2O_3(ZnO)_n$ Nanowires (I)

The ability to control the MO_2^- inclusion density is a direct result of the solid-state diffusion process by which the polytypoid nanowires are produced. The diffusion rates of In, Ga, and Zn within ZnO are extremely high at the 1173 K annealing temperature, with values of 6.62×10^{-12}, 1.09×10^{-14}, and 1.13×10^{-12} $cm^2 \cdot s^{-1}$, respectively[27,28]. DFT calculations show that Zn atoms diffuse through ZnO using Zn vacancies[29]. Based on their activation energies for diffusion, In and Ga are also thought to diffuse through Zn vacancies, though some controversy exists regarding their true activation energies[27,30,31]. Since In and Ga are substitutional

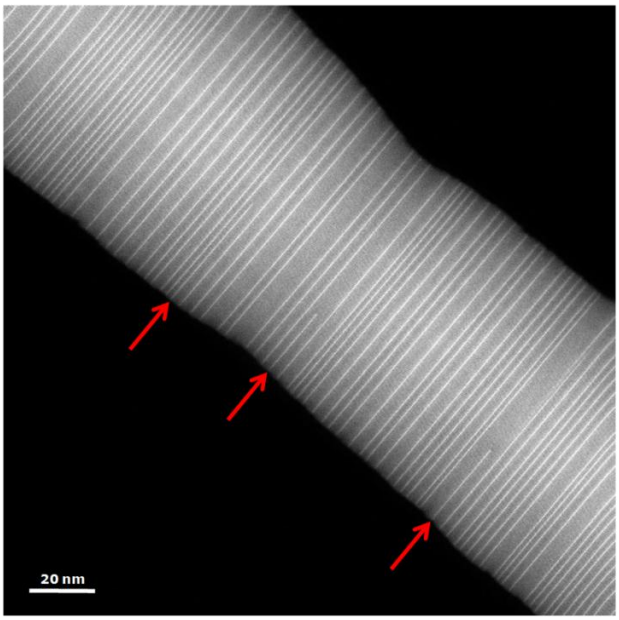

Figure 32 – Diameter fluctuations and partial octahedral layers: Z-contrast STEM image of a 10/10 IGZO nanowire showing diameter fluctuations with inclusion density. The arrows indicate the presence of partial inclusions, all of which are connected to one side of the nanowire.

dopants, Zn atoms must diffuse out when the In and Ga atoms diffuse in. The Zn atoms diffuse to the surface of the nanowire, leading to a modulation in the diameter (Figure 42). In areas of higher inclusion density, the diameter of the nanowire is slightly thicker (more In and Ga diffused in, more Zn diffused out) compared to areas of lower inclusion density.

Once the In and Ga diffuse into the nanowire, they strain the wurtzite lattice of

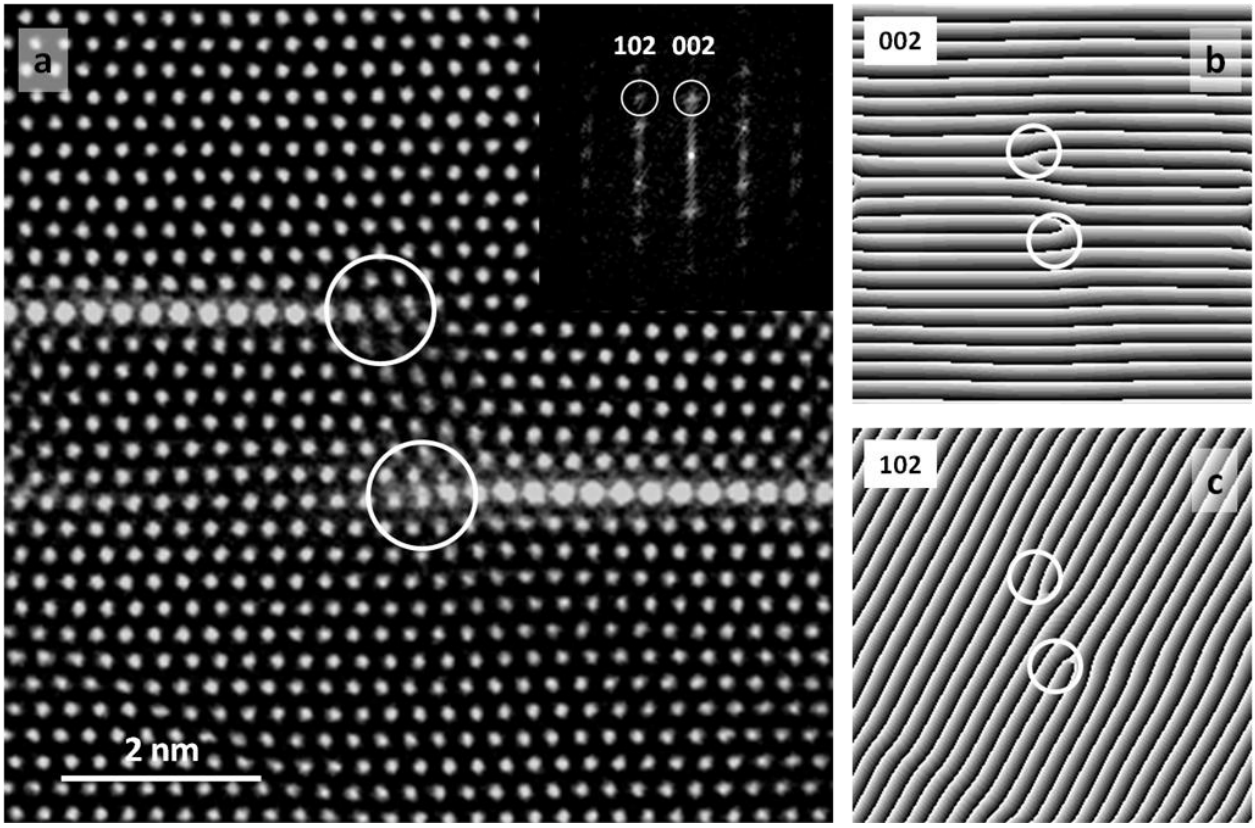

Figure 43 – Edge Dislocations at Partial Layers: (a) HRSTEM image of IGZO oriented on the [010] zone axis with two incomplete MO_2^- layers and the corresponding FFT (inset). Moiré images takes along the (b) 002 and (c) 102 reflections clearly showing the presence of edge dislocations at the end of each incomplete MO_2^- layer

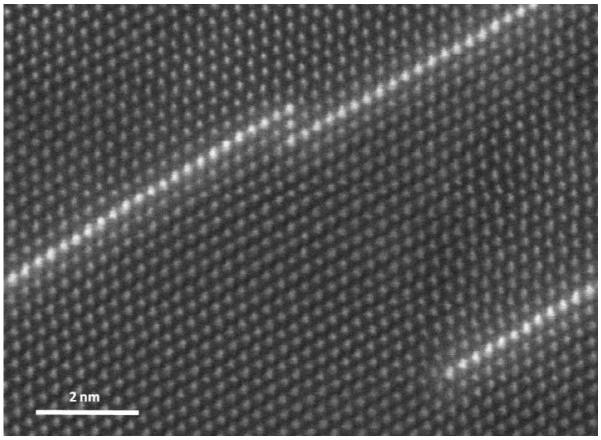

Figure 44 - Partial inclusions meeting in the middle: Z-contrast HRSTEM image of IGZO showing three partial inclusions. The two partial inclusions at the top of the image appear to be merging together via edge dislocation climb to create a single complete inclusion layer

the pure ZnO, deforming the structure, and eventually relaxing the strain by creating octahedral In/Ga inclusions and trigonal bipyramidal layers. Defects such as edge dislocations, stacking faults, and inversion domain boundaries are known to attract impurities and can assist in the formation of impurity inclusions[32]. In some of the nanowires synthesized in this study, especially those made with lower amounts of In and Ga, partial In/Ga inclusions were observed (Figure 41a-c). The ends of these partial inclusions are usually associated with edge dislocations with the dislocation line lying at the leading edge of the MO_2^- plane[33]. Edge dislocations can be seen in Figure 43a in the HRSTEM image of two partial inclusions. Moiré images taken along the 002 and 102 reflections clearly show the presence of the edge dislocations. Another interesting observation is that the partial inclusions are always connected to one surface of the nanowire (Figure 42), indicating that the growth of the inclusion starts at the surface and proceeds across the diameter of the nanowire until it either reaches the opposite side or connects with an inclusion growing from the opposite side (Figure 44).

If the inclusions are growing through a defect-assisted process and the inclusion formation begins at the nanowire surface, then the edge dislocation must somehow nucleate near the surface. One possible scenario is that the edge dislocations are formed on the nanowire surface via heterogeneous nucleation, which occurs with the help of defects such as impurity atoms. Since In has a larger radius compared to Zn, the dissolution of In within the wurtzite lattice will create strain. The presence of dislocations within the lattice can relax some of this strain if the In atoms diffuse towards the dislocations and eventually occupy those lattice positions below the edge dislocations where the lattice is already expanded. The edge dislocation basically creates a "hole" in which the larger In atoms can sit. Due to the high diffusion rate of In within the ZnO lattice, the In atoms can rapidly concentrate at the sites of edge dislocations. Since the In atoms have a mutual attraction they can crystallize into another phase (octahedrally

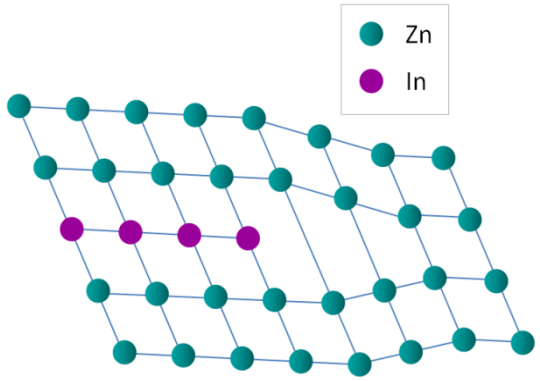

Figure 45 – Defect-assisted Inclusion Growth: Model showing the edge dislocation and associated expanded lattice which is believed to promote growth of the MO_2^- octahedral inclusions.

coordinated MO_2^-) which will flow in one direction towards the dislocation. The growth of the inclusion will continue along the dislocation until the concentration of In within the lattice decreases to the point at which equilibrium is reached. In the lower concentration samples, more partial inclusions can be observed, likely resulting from insufficient quantities of In atoms necessary to complete the inclusions. In the 40/40 samples with higher concentrations of In, no partial inclusions were observed.

3.5.d - Thermoelectric Properties of $In_{2-x}Ga_xO_3(ZnO)_n$ Nanowires (I)

Previous work on nanowire thermoelectrics suggests that the phononic contribution to thermal transport can be significantly reduced through size reduction and surface engineering[34,35]. Therefore, the combination of a superlattice structure and a single-crystalline nanowire could lead to a better phonon-scattering and charge-transporting structure, and hence a better thermoelectric material[36]. The thermoelectric measurements in this work focus on IGZO nanowires prepared from combined 5 nm In and 5 nm Ga coatings on ZnO nanowires.

3.5.d.i - Electrical Properties of IGZO Nanowires

The presence of the MO_2^- inclusions alters both the thermal and electrical properties in the converted polytypoid nanowires. While ZnO can exhibit a relatively high intrinsic electrical conductivity due to formation of oxygen vacancies acting as donor states, the introduction of slight amounts of Al, In, or Ga can further increase the conductivity when substituted for Zn[12]. Considering all the $M_2O_3(ZnO)_n$ nanowires synthesized in this study, the high inclusion density and significant dopant level present in the IGZO nanowires makes them the ideal candidate for thermoelectric enhancement, and thus, IGZO nanowires were used for all transport studies. Electrical devices were made by either drop-casting or micro-manipulating nanowires onto a Si chip with 200 nm of thermal oxide on the surface. The nanowires were top-contacted using metallic contacts defined by standard photolithography techniques. Ti/Au was used as the contact and Ohmic contact was achieved after rapid thermal annealing.

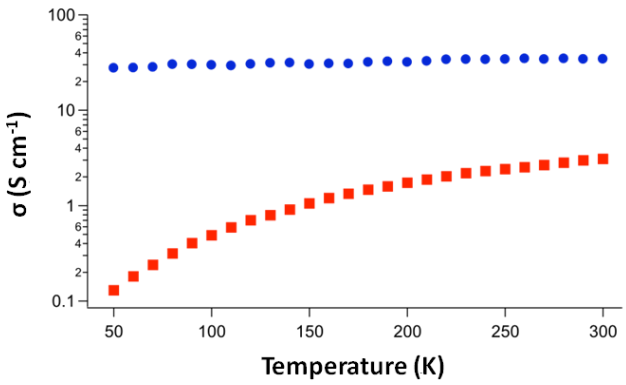

Figure 46 – IGZO Electrical Conductivity: Electrical conductivity as a function of temperature for a 120-nm diameter 5/5 IGZO nanowire (blue circles) and a 110-nm diameter ZnO nanowire (red squares).

The increased electrical conductivity observed at room temperature in the IGZO nanowires when compared to the ZnO nanowires is consistent with that of a slightly doped

semiconductor (Figure 46). However, considering the relatively large amount of In and Ga incorporation (greater than 2% atomic of each metal atom from EDS), the observed increase in conductivity is smaller than the metallic-like value of conduction that is expected. While the In and Ga impurities can act as electrical dopants in ZnO when substituted for tetrahedrally-coordinated Zn, In and Ga also sit in the trigonal bipyramidal sites, helping to preserve electroneutrality and reducing the number of generated carriers. Moreover, the MO_2^- inclusions can act as barriers to oxygen diffusion leading to decreased conductivity by suppressing the formation of oxygen vacancies[37]. Interestingly, the linear temperature-dependent resistance of IGZO, as seen in Figure 46, is not typical behavior for a slightly doped semiconductor (of which pure ZnO nanowires are an example) nor of a degenerately doped semiconductor (which should give metallic behavior). This deviation from the classical semiconducting behavior indicates a departure from the typical thermally-activated mechanism. The octahedral layers could be acting as potential barriers to electron diffusion, leading to alternative transport mechanisms such as pseudo variable-range hopping or percolation conduction[38].

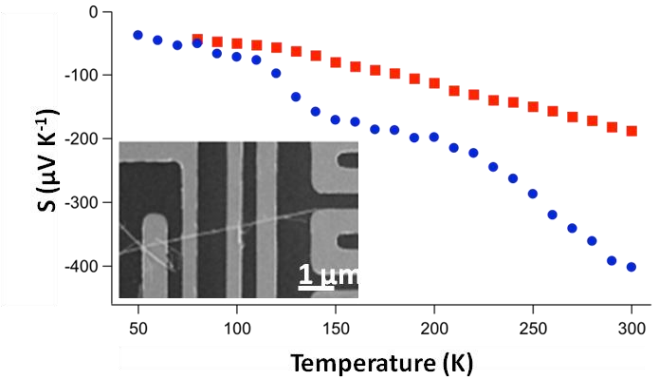

Figure 47 – IGZO Seebeck Coefficient: Seebeck as a function of temperature for a 120-nm diameter 5/5 IGZO nanowire (blue circles) and a 110-nm diameter ZnO nanowire (red squares). Measurements were made on the same nanowires used for electrical conductivity. Inset shows a SEM of an individual nanowire in a four-point FET/Seebeck device.

The presence of the inclusion layers also has an effect on the induced Seebeck voltage, as seen in Figure 47. Seebeck coefficients were determined by measuring the thermal voltage induced by passing current through a heating coil near the nanowire. The contacts where used as resistive thermometers to measure the temperature difference across the nanowire. At 300 K, the Seebeck coefficient grew in magnitude from –188 $\mu V \cdot K^{-1}$ in ZnO nanowires to –402 $\mu V \cdot K^{-1}$ in IGZO nanowires. Similar Seebeck values were observed in each of the many ZnO and IGZO nanowire samples measured, respectively. The observed increase in Seebeck coefficient may be an effect of the potential barriers, which could act as low-energy electron filters[39]. When a temperature gradient is applied, charges diffuse to states of lower chemical potential. While most of these states are on the colder side, unoccupied states on the hotter side allow for charge diffusion in the opposing direction, thereby limiting the overall potential that can develop for a given temperature gradient. Charges that participate in back diffusion are referred to as “cold electrons” (for n-type semiconductors) since they posses lower carrier energy. However, potential barriers with appropriate energy levels can act as low energy charge filters by preferentially affecting their mobility[40]. By limiting the amount of back diffusion, a larger potential can develop, resulting in an increased Seebeck coefficient.

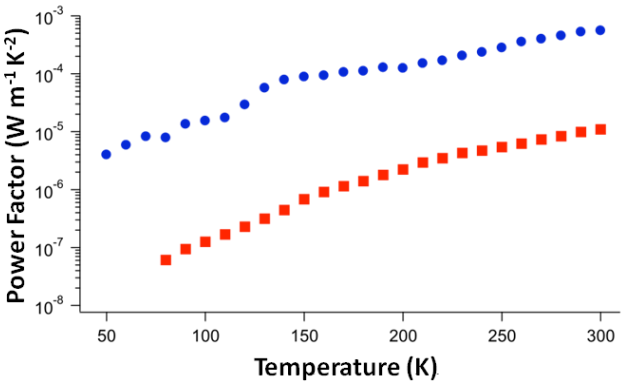

Figure 48 – IGZO Power Factor: Power factor as a function of temperature. The electrical conductivity and Seebeck values were taken from the same nanowires (Figures 46,47).

Aside from filtering, the possibility exists that electronic quantum confinement caused by closely spaced inclusion layers contributes to the rise in Seebeck values[41,42]. Since ℓ values of less than 2.34 nm (exciton Bohr radius of ZnO) were observed, thermopower enhancement might be due to slight changes in the density of states near the Fermi level[43]. While difficult to quantify at this time, the random nature of the single crystalline, polytypoid nanowires perhaps plays a role in these and other transport phenomena. Further theoretical and experimental investigations are required in order to paint a clearer picture of this nanowire system.

Regardless of the source of enhancement, by converting the ZnO nanowires into IGZO, the resulting power factor ($S^2\sigma$) changed by a factor of 58 to 0.6 $mW \cdot m^{-1} \cdot K^{-2}$(Figure 48). While this value is lower than the reported power factor of nominally Al-doped ZnO[44], it is ~6 times larger than the power factor of bulk IZO materials[45]. The complete thermoelectric properties for bulk IGZO have not been reported in a single study, so while the comparison between IGZO nanowires and bulk IGZO is more relevant, the transport properties within this work are primarily given relative to the similarly structured bulk IZO.

3.5d.ii - Carrier mobility enhancement in IGZO Nanowires

To ensure that the observed Seebeck enhancement is not due to mere increases in impurity scattering, FET mobilities were measured on the same nanowires from which the electrical conductivity and Seebeck coefficient were determined (Figure 49). Both carrier concentration and mobility enhancements were observed when compared to the pure ZnO nanowires. This indicates that the carrier concentration, and not the mobility, is the limiting factor in the electrical conductivity, contrary to what may have been suspected based on the defects that accompany each MO_2^- layer. Furthermore, 177 $cm^2 \cdot V^{-1} \cdot s^{-1}$ at 300 K is more than twice the field effect mobility value

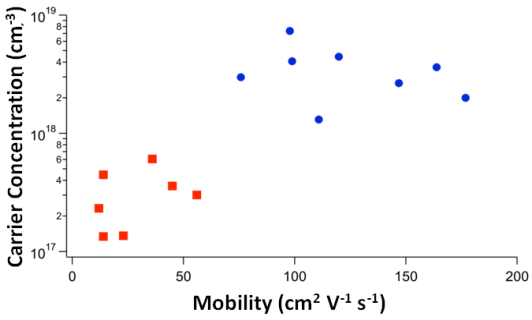

Figure 49 - IGZO Mobility: Single-nanowire measurements of carrier concentration as a function of mobility, as measured from the FET geometry. No diameter dependence was observed for ZnO or IGZO nanowires in the range of 75–130 nm.

previously measured in single crystalline IGZO thin films[37]. The nature of the mobility enhancement in the polytypoid IGZO nanowires over IGZO thin films is not fully understood. However, the enhancement over the single crystalline ZnO nanowires may be explained by the induced strain at the MO_2^- layer interfaces. It is well established that piezoresistive materials, both crystalline and amorphous, demonstrate mobility changes with the application of stress[46,47]. As seen in Figure 38, the 17% difference in the *d* spacing at the octahedral/wurtzite interface produces a significant amount of strain. Although the inclusions are perpendicular to the transport direction, the mobility could be enhanced by possible strain-induced changes to the electronic band structure. Further theoretical and experimental work is necessary to determine the extent to which strain plays a role in this polytypoid system.

3.5.d.iii - Thermal Conductivity Reduction in IGZO Nanowires

Not only do the nanostructured features influence electronic transport, they also act as important phonon scattering interfaces, thereby limiting the lattice thermal conductivity[48]. Thermal transport in individual nanowires was accomplished using pre-fabricated MEMS devices, upon which single nanowires were physically manipulated using thin tungsten probe tips. Full descriptions of the measurement scheme can be found elsewhere[49]. Compared to literature values for bulk ZnO (100 $W \cdot m^{-1} \cdot K^{-1}$), ZnO nanowires demonstrate up to five-fold reduction of thermal conductivity at room temperature (Figure 50b)[50]. An estimation of the average phonon mean free path as a function of temperature shows that the limiting factor is the nanowire diameter until the 150–200 K range, where other scattering mechanisms, such as impurity and umklapp scattering, begin to limit the conductivity. As seen in Figure 50b, the linear segment of the ZnO nanowire plot begins to plateau around that temperature range. The IGZO nanowires, on the other hand, show no such plateau, indicating that the MO_2^- layers, and not to the nanowire diameter, are limiting the average phonon mean free path throughout the

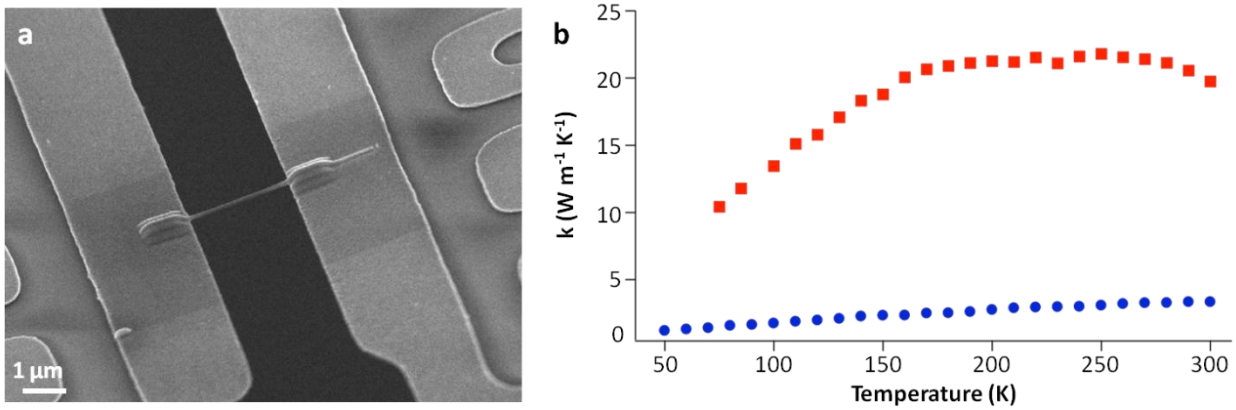

Figure 50 – Thermal Conductivity of IGZO: (a) SEM of an individual IGZO nanowire bridging two suspended membranes on a prefabricated MEMS device used for thermal conductivity measurements. (b) Thermal conductivity as a function of temperature for both a 120-nm 5/5 IGZO nanowire and a 90-nm ZnO nanowire.

measured temperature range. At 300 K, IGZO nanowires exhibit a thermal conductivity of 3.3 $W \cdot m^{-1} \cdot K^{-1}$, which is only slightly lower than what has been observed for IZO in the bulk (3.5 $W \cdot m^{-1} \cdot K^{-1}$, n=3,4)[51]. However, since bulk IZO has both higher inclusion density and periodicity, it is surprising that the more disordered 5/5 IGZO nanowires exhibit comparable thermal transport properties. While higher inclusion densities are expected to limit the average phonon mean free path, the disordered nature of the polytypoid IGZO structure combined with the nanowire geometry similarly affects the overall thermal energy propagation, as seen in other systems[52].

3.5.d.iv – Thermoelectric Figure of Merit of IGZO Nanowires

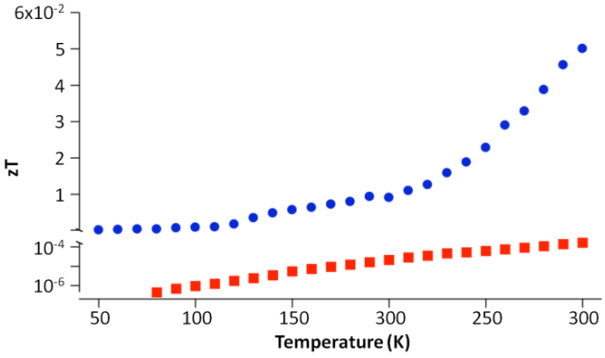

Figure 51 – Figure of Merit of IGZO Nanowires: Figure of merit, ZT, of IGZO nanowires compared with ZnO nanowires showing an enhancement of 2.5 orders of magnitude.

As a direct result of the polytypoid structure, ZT was increased from 1.7×10^{-4} for ZnO nanowires to 0.055 for the IGZO nanowires at 300 K, an enhancement of 2.5 orders of magnitude (Figure 51)[51,53]. Such ZT values represent a factor of ~10 enhancement when compared to the similarly structured bulk IZO superlattice samples. However, since oxide-based thermoelectric modules are typically employed at elevated temperatures (700-1000 K), further studies within the relevant temperature range are required.

3.5.e – Optical Properties of $In_{2-x}Ga_xO_3(ZnO)_n$ Nanowires (I)

The optical properties of the IGZO nanowires were investigated to check their viability for other applications such as photoelectrochemical water splitting. The absorbance was measured using a 300 W Xe lamp illumination source and an integrating sphere coupled to a spectrometer. By using the integrating sphere it was possible to measure the absorbance and eliminate any scattering effects. The absorbance of the IGZO nanowires (Figure 52a) is similar to that reported previously for IZO nanowires[21] but is significantly different from that reported for the bulk IZO samples

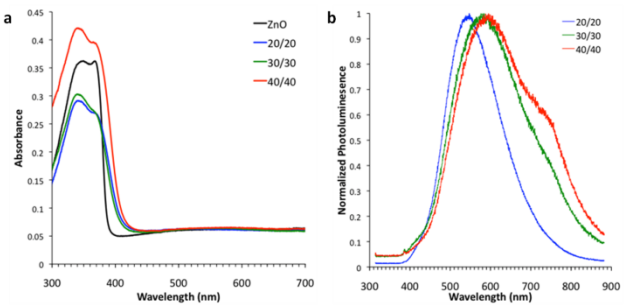

Figure 52 – Absorbance and Photoluminescence of IGZO Nanowires: (a) Absorbance and (b) photoluminescence of IGZO nanowires prepared with varying amounts of metal deposition.

used for water splitting[17]. There is a slight tail in the visible region with no apparent shift of the band edge. The drop-off in absorbance around 350 nm is an artifact due to the loss of intensity of the illumination source in the UV region. The photoluminescence (PL): C of the IGZO nanowires was analyzed using the 325 nm line of a continuous wave HeCd laser. The laser excitation was focused onto the nanowire sample with a beam diameter of ~50μm. The emission was collected through a microscope objective and routed to a spectrometer using an optical fiber. Unfortunately, the IGZO PL (Figure 52b) was not from band edge emission but rather was entirely from defect emission, which is contrary to previous reports[19-21]. This is likely a result of the high temperature O_2 anneal that was used during the conversion process, which could introduce a high density of oxygen interstitials. In order for these nanowire materials to achieve a high efficiency for optical applications, such a PEC water splitting, it will be necessary to reduce the oxygen interstitials which can act as trap states for charge recombination.

3.5.f – $M_2O_3(ZnO)_n$ Nanowires Synthesized by Solid-State Diffusion (I): Conclusions

In summary, $M_2O_3(ZnO)_n$ (M = In, Ga, Fe) polytypoid nanowires were converted from pure ZnO nanowires using a facile diffusion scheme. This solid-state diffusion process can be used to produce a wide range of ZnO alloys with controllable alloy concentration and inclusion layer density. The inclusion growth is believed to originate from the surface and propagate though the nanowire by a defect-assisted process. Single-nanowire measurements on IGZO show that both the power factor and thermal resistivity were enhanced due to the nanostructured features inherent to this thermally stable system. In addition, compared to bulk IZO and other doped ZnO, IGZO nanowires show a marked improvement in ZT at room temperature. From this study it is apparent that better control of nanometer-scale features could be the key to developing next-generation thermoelectric materials.

3.6 – $M_2O_3(ZnO)_n$ Nanowires Synthesized by Alternative Solid-State Diffusion Methods

The conversion of ZnO nanowires into $M_2O_3(ZnO)_n$ nanowires using solid-state diffusion introduces a new and exciting technique for the generation of superlattice nanowires. The simplicity of the conversion opens the door to a variety of synthetic methods that may enable improved optical properties as well as more “green” preparation of the nanowires. Some alternative syntheses will be presented in the following sections.

3.6.a - $M_2O_3(ZnO)_n$ Nanowires Synthesized by Solid-State Diffusion (II)

If the $M_2O_3(ZnO)_n$ nanowires are to be used for water splitting applications, it is important that they be of high optical quality. In the previous section we showed that the $M_2O_3(ZnO)_n$ nanowires converted under an O_2 environment exhibit defect-dominated photoluminescence. The total lack of band edge photoluminescence and the large defect peak indicate the presence of a high density of trap states, likely the result of oxygen interstitials introduced during the high temperature O_2 anneal. Therefore, it would be preferable to avoid this O_2 anneal by modification of the synthetic procedure. In addition, metal evaporation by thermal evaporation is somewhat directional leading to an inhomogeneous deposition of metal nanoparticles along the length of the nanowires. The inhomogeneous deposition can cause a gradual decrease in superlattice inclusion density moving from the nanowire tip to the base. This complication may be avoided by using a vapor-phase metal precursor rather than a solid metal precursor deposited on the nanowires.

3.6.a.i – Synthesis of $M_2O_3(ZnO)_n$ Nanowires Synthesized by Solid-State Diffusion (II)

Previously $M_2O_3(ZnO)_n$ superlattice nanowires were synthesized by first depositing the desired metal onto the surfaces of the ZnO nanowires using thermal evaporation. These ZnO/M core/shell nanowires were then annealed at high temperature in O_2 to form the superlattice structures. An alternative synthesis has been developed to combine these steps into one step using vaporized precursors (Figure 53). This vapor method sidesteps the O_2 anneal and promotes better homogeneity of superlattice inclusions along the length of the nanowires.

First, ZnO nanowires were grown by CVT methods as described in section 3.5.a. The desired metal precursors, either pure Ga or an alloy of In and Ga, were loaded into a small alumina boat and inserted inside a 1-inch quartz tube. The quartz tube was placed in a horizontal tube furnace such that the metal precursor boat was directly at the center of the furnace. ZnO nanowire substrates were loaded into the tube downstream of the alumina boat at distances of 4 to 12 cm from the center of the furnace. The tube was purged with 150 sccm

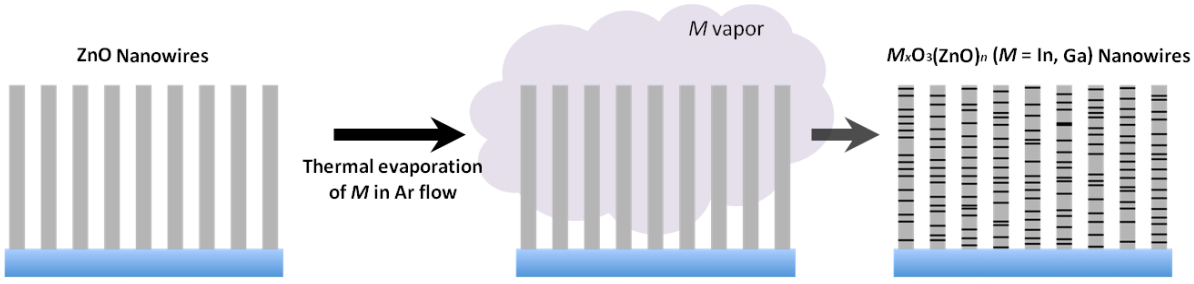

Figure 53 - $M_2O_3(ZnO)_n$ Vapor Synthesis Schematic: Schematic illustration of the solid-state diffusion synthesis of $M_2O_3(ZnO)_n$ alloy nanowires via vapor methods

of Ar for 30 min and then rapidly heated to 973 K. The furnace was held at 973 K for 30-60 min and then cooled to room temperature. Depending on the substrate position, furnace temperature, and conversion time, doped ZnO, $M_2O_3(ZnO)_n$ superlattices, or ZnM_2O_4 nanowires were produced.

3.6.a.ii – Structural Analysis of $M_2O_3(ZnO)_n$ Nanowires (II)

XRD patterns (Figure 54a) of the GZO nanowires after conversion under Ga vapor show a pattern similar to that of pure ZnO, which corresponds to our previous results on IGZO nanowires. This indicates that the nanowires maintain a wurtzite-type crystal structure. It is important to note that no peaks corresponding to an orthorhombic structure were observed. SEM images (Figure 54b) of the converted nanowires indicate that the nanowire morphology was maintained through the conversion process.

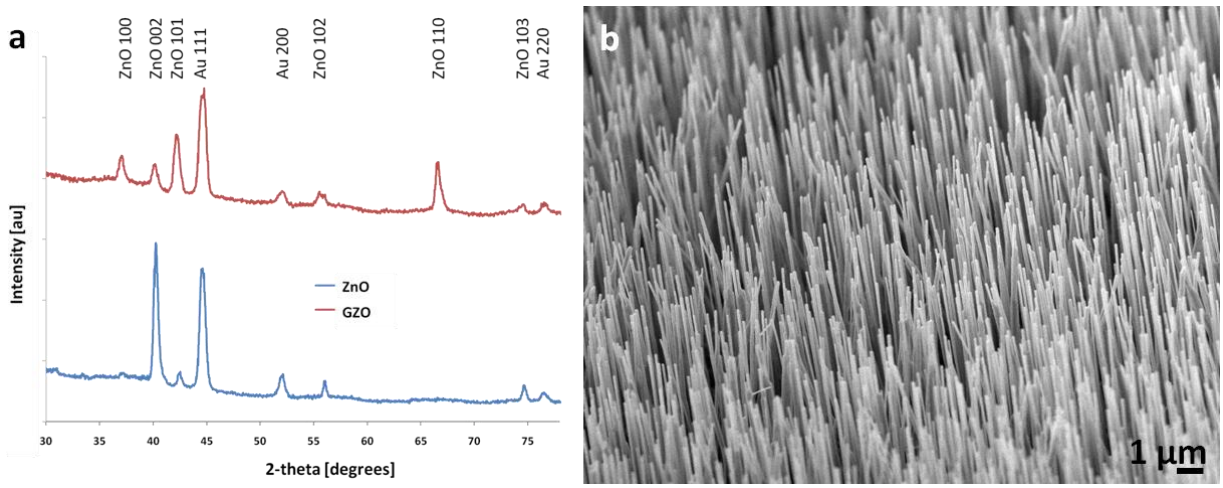

Figure 54 – XRD pattern and SEM image of GZO nanowires prepared with a vaporized Ga source. (a) XRD pattern showing a wurtzite pattern for the GZO nanowires, and (b) SEM image of GZO nanowires indicating that the nanowire morphology is maintained.

Based on TEM images (Figure 55), the superlattice structure of the GZO nanowires is similar to that of the IGZO nanowires from the previous section. This result is different from the orthorhombic structure reported by other groups on GZO bulk materials using single-crystal X-ray diffraction and TEM analysis[54-56]. This change in the structure of GZO compared to the $LuFeO_3(ZnO)_n$-type structure of IZO and IGZO was tentatively attributed to the smaller ionic radius of Ga (compared to In), which could make it unsuitable for octahedral coordination[57]. However, based on the EDS map (Figure 36) taken of the IGZO nanowires in the previous section, it appears that Ga can occupy the octahedral sites of the lattice. TEM analysis of the bulk GZO materials found that the structure consisted of Ga-O layers separated by Ga/Zn-O blocks[54]. While this is a similar configuration as that of IGZO, the difference is that in this case all the metal atoms are tetrahedrally coordinated. The Ga/Zn-O blocks resemble a wurtzite structure, and the c-axis of these wurtzite sections is at a 30° angle compared to the c-axis of

the orthorhombic structure, and the c-axes of adjacent Ga/Zn-O blocks are 60° from one another. Thus, along the orthorhombic c-axis there is a zigzag shape with the tops and bottoms of the V's corresponding to the M-O layers. However, as opposed to the zigzags observed in IGZO, these zigzags are parallel to the c-axis (orthorhombic) such that the M-O layers cross the zigzags at each apex. DFT calculations by Da Silva et al. on $Ga_2O_3(ZnO)_6$ found that the lowest energy configuration was an orthorhombic structure in which groups of gallium agglomerates and twin boundaries act to revert the polarity within the lattice[58]. However, they found that the metal cations were not all tetrahedrally coordinated, but rather that some of the Ga cations had a trigonal bipyramidal coordination.

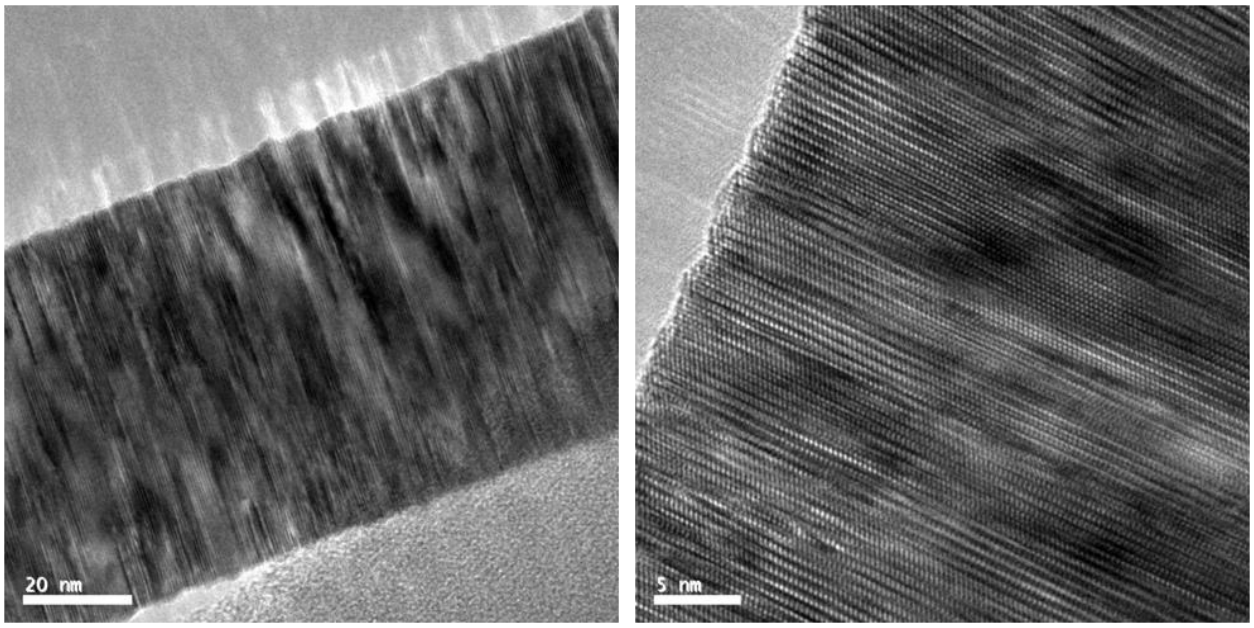

Figure 55 – TEM images of GZO nanowires converted under Ga vapors: (a) Low-magnification TEM image showing superlattice inclusions perpendicular to the [001] growth direction of the ZnO nanowire. (b) High-magnification TEM image of the same nanowire showing a structure similar to that reported for IGZO.

Figure 55 shows low and high-magnification TEM images of a GZO nanowire prepared using a vaporized Ga source. The structure appears very different from that of the bulk GZO material[54] and very similar to that of the IGZO nanowires reported in the previous section. This structure was also observed in those GZO nanowires prepared using the first reported synthetic method, though the GZO nanowires prepared with a vapor Ga source can achieve significantly higher inclusion densities. The Ga composition of these nanowires was as high as 38% by TEM EDS. As shown in Figure 54a, these GZO nanowires had XRD patterns corresponding to that of wurtzite ZnO rather than that of an orthorhombic structure. Also, there are no apparent zigzags running perpendicular to the inclusions as observed in the reported bulk GZO samples. Instead, there are inclusions perpendicular to the c-axis of the wurtzite structure of the nanowires and apparent stacking faults at each inclusion layer, similar to that of the IGZO nanowires. Unfortunately, due to the similarity in atomic numbers of Ga

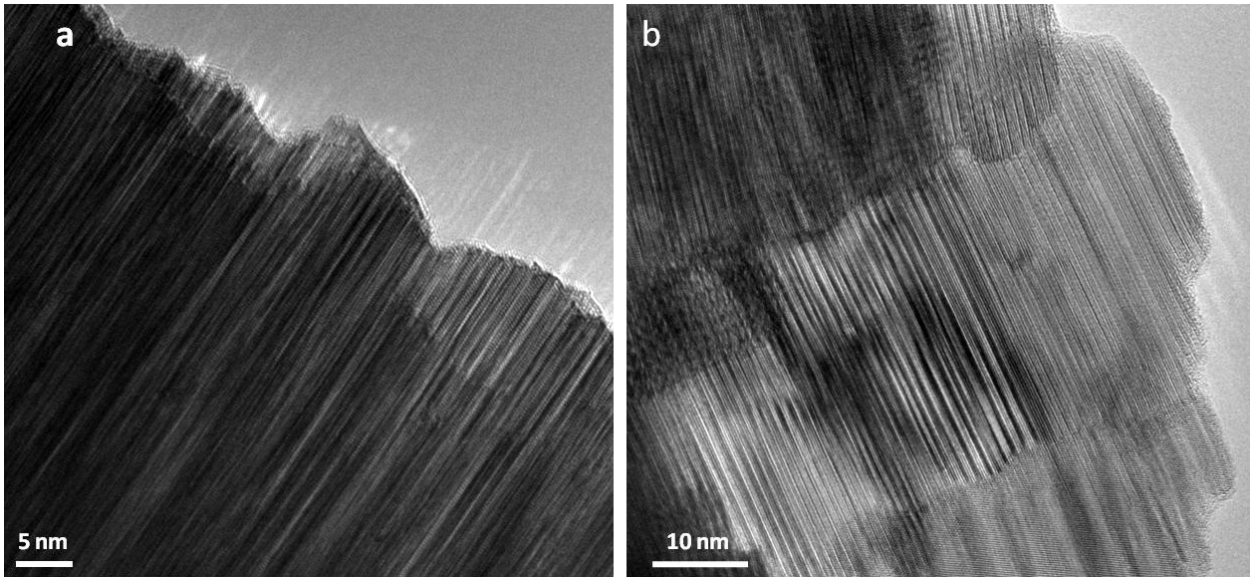

Figure 56 – TEM images of IGZO nanowires prepared using In and Ga metal vapor: TEM images showing the high inclusion density that is easily attained using the vapor method.

and Zn, Z-contrast STEM imaging is not useful in elucidating the structure of these nanowires. More in-depth TEM analysis is required to get better picture of their true structure.

The IGZO nanowires prepared by this method exhibit the same structures as those reported in the previous section. However, using this method is was very easy to achieve high inclusion densities. By TEM EDS, the composition of the nanowires shown in Figure 56b is 57.4% Zn, 21.6% Ga, and 21.0% In.

3.6.a.iii – Optical Properties of $M_2O_3(ZnO)_n$ Nanowires (II)

To remove any possible effects from films deposited around the bases of the nanowires, all PL measurements were done on single or groups of 2-3 nanowires. The nanowires were placed on lacey carbon TEM grids for measurement. PL was taken of a blank TEM grid and the signal was negligible compared to that of the PL from the nanowire samples. The optical properties of the nanowires prepared using the

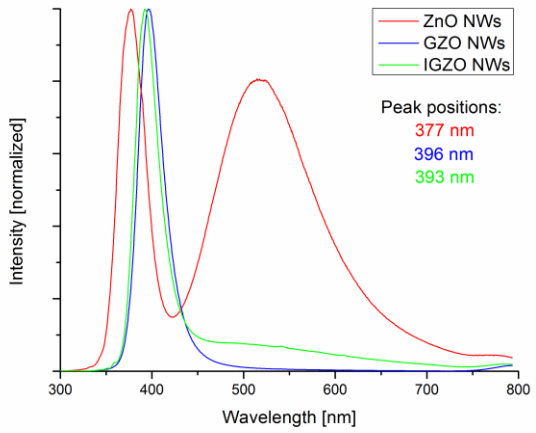

Figure 57 – PL of ZnO, GZO, and IGZO Nanowires: PL of ZnO (band edge peak: 377nm), GZO (396 nm), and IGZO (393 nm). The GZO and IGZO nanowires were prepared by annealing ZnO nanowires under metal vapor.

metal vapor method were significantly improved over those nanowires prepared using the high-temperature O_2 anneal. As shown in Figure 57 the GZO and IGZO nanowires prepared by this method show almost 100% band edge PL as opposed to the 100% defect emission observed in the previous samples. Another interesting thing to note is that the ZnO nanowires used in the conversion process generally showed a large defect peak around 500 nm, but after the conversion the defect peak was completely removed. There was a slight red shift in the PL of both the GZO and IGZO nanowires. In the five GZO nanowires samples measured, the band edge peak position was between 390 – 396 nm as opposed to the 377 nm peak of the pure ZnO nanowires. The IGZO nanowire samples showed band edge emission between 381 and 393 nm.

3.6.a.iv – $M_2O_3(ZnO)_n$ Nanowires Synthesized by Solid-State Diffusion (II): Conclusions

Compared to the first synthetic technique reported in section 3.4.a the vapor technique requires less steps, is considerably faster, and enables a significantly higher inclusion density without the need to add additional deposition and annealing procedures. In addition, preliminary results indicate that the inclusion density can be easily tuned by simply varying the annealing temperature, the annealing time, and the substrate position within the furnace. This high level of tunability makes it possible to synthesize doped ZnO, superlattice, and spinnel metal oxide nanowires by merely tweaking the experimental conditions. Initial experiments also suggest that the superlattice inclusion density is more uniform along the length of the nanowires compared to the previous method. However, additional experiments are necessary to study both the tunability and homogeneity of the inclusion density. One possible downfall of this technique is that it's not clear whether other superlattice compositions can be synthesized using this method since it may be limited to those metals with higher vapor pressures.

The significant enhancement of band edge emission achieved using this alternative synthetic technique opens the door for additional applications such as photoelectrochemical water splitting. The absence of the large defect peak indicates that the density of oxygen defects is considerably lower which should lead to less recombination and possibly higher efficiencies compared to the previously reported nanowires. Superlattice nanowires for photoelectrochemical water splitting will be the subject of future research within the Yang group.

3.6.b – $M_2O_3(ZnO)_n$ Nanowires Synthesized by Solid-State Diffusion (III)

When preparing materials for clean, renewable energy applications it is important to consider the environmental effects associated with the synthesis itself. A majority of the semiconductors currently used for solar and thermoelectric applications (e.g. Si, CdTe, and Bi_2Te_3) are synthesized using toxic precursors and/or have large energy costs associated with

low-pressure or high temperature processes. Aqueous solution-phase syntheses avoid these harmful precursors and energy costs making them especially attractive for the "green" preparation of semiconductors. In addition, liquid-based processes are generally favored over vapor-based processes in manufacturing. Thus, it would be ideal if $M_2O_3(ZnO)_n$ nanowires could be prepared using solution-phase chemistries.

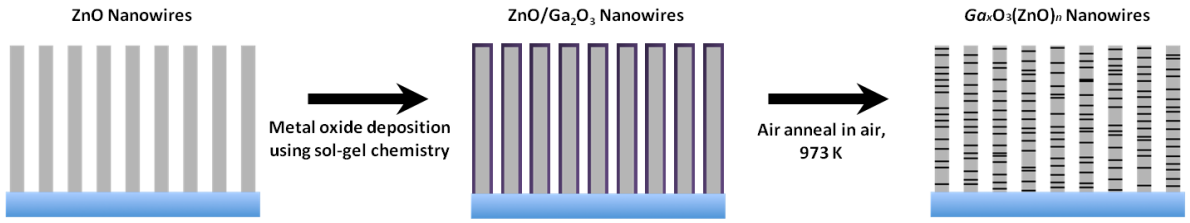

Figure 58 - $M_2O_3(ZnO)_n$ Sol-gel Synthesis Schematic: Schematic illustration of the solid-state diffusion synthesis of $M_2O_3(ZnO)_n$ alloy nanowires via sol-gel methods

3.6.b.i – Synthesis of $M_2O_3(ZnO)_n$ Nanowires by Solid-State Diffusion (III)

The high temperature O_2 anneal used to prepare $M_2O_3(ZnO)_n$ nanowires via the method presented in section 3.4.a leads to an immediate oxidation of the metal nanoparticles used for the conversion process. This indicates that the conversion can be accomplished using metal oxide precursors. Sol-gel techniques, which involve the deposition of solution phase precursors followed by a low-temperature air anneal, are commonly used to generate metal-oxide materials. Using ZnO nanowires synthesized by hydrothermal methods and sol-gel Ga_2O_3 as a metal precursor, a primarily solution-based $M_2O_3(ZnO)_n$ nanowire synthesis was achieved by depositing a thin layer of Ga_2O_3 on the surfaces of the ZnO nanowires and annealing in air (Figure 58).

The ZnO nanowires arrays used for this synthesis were grown by aqueous solution-phase methods to make the preparation of the $M_2O_3(ZnO)_n$ nanowires as "green" as possible[59]. The nanowires were grown on Si substrates using a layer of ZnO nanoparticle seeds. The

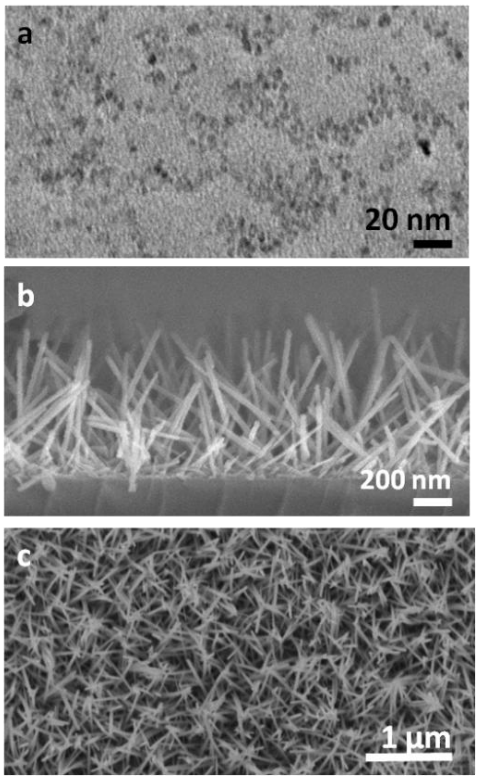

Figure 59 – ZnO Nanowire Synthesis: (a) TEM image of the ZnO nanoparticles used to seed the ZnO nanowire growth, (b)cross-sectional SEM image of the ZnO nanowire arrays showing ~600 nm long nanowires aligned within 45° of vertical, and (c) top-down view of the same nanowire array.

ZnO nanoparticles were synthesized using a previously reported procedure[60]. Briefly, 0.274 g zinc acetate dihydrate were dissolved in 125 mL of anhydrous ethanol and heated to 333 K under stirring. A second solution of 0.078 g of NaOH in ethanol was added drop-wise to the zinc acetate solution over a period of 2 hours resulting in the formation of ZnO nanoparticles a few nanometers in diameter (Figure 59a). The nanoparticles were stored in the growth solution at 293 K, stabilizing them for a period of at least 1 year. A clean 4-inch Si wafer was scored into 17 mm x 17 mm pieces such that after the ZnO nanowire synthesis the pieces could be easily broken apart. The ZnO nanoparticle solution was poured over the Si wafer and dried with a stream of N_2. The ZnO nanoparticle deposition was repeated for a total of 3 times to create a homogeneous film of nanoparticles. After preparation of the ZnO nanoparticle seed layer, the wafer was suspended upside down in a crystallizing dish.

The ZnO growth solution was prepared using 1 L of distilled H_2O, 7.44 g zinc nitrate hexahydrate, 3.51 g of hexamethylenetetramine, and 4.00 g of polyethyleneimine (low molecular weight, branched). This solution was stirred at 300 rpm and heated to 368 K for approximately 15 min or until the solution turned a bright yellow color. During the solution preparation a large amount of ZnO precipitates formed in the solution. To remove the precipitates the solution was filtered through a 0.2 µm filter. The finished solution was poured over the seeded wafer in the crystallizing dish.

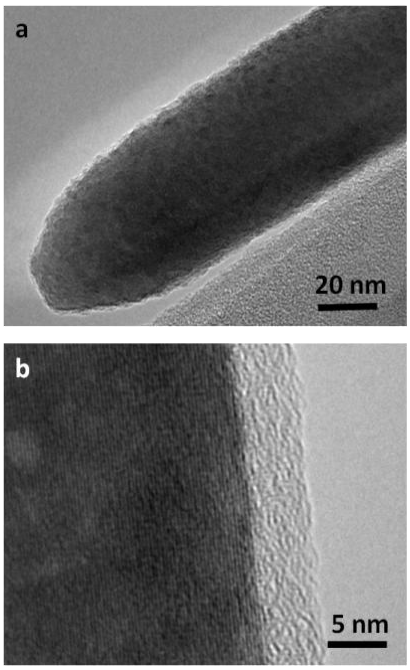

Figure 60 – TEM of ZnO/ Ga_2O_3 Nanowires: TEM images of ZnO nanowires coated with Ga_2O_3 after annealing at 573 K.

For the nanowire growth, the solution was heated to 368 K for 2 hours. The wafer was immediately removed and thoroughly washed with water before drying it with a stream of N_2. The wafer was then gently broken into 17x17 mm pieces using the score marks on the back of the wafer. The as-grown nanowires had diameters of 50-70 nm and lengths of approximately 600 nm and the nanowires were oriented within about 45° of vertical.

Next, the Ga_2O_3 sol-gel solution was prepared using a procedure reported by Kokubun et al[61]. A solution of 2.0 g gallium isopropoxide (Alfa Aesar), 19.5 mL anhydrous 2-methoxymethanol, and 0.5 mL of monoethanolamine (Sigma) were prepared in an air-tight flask inside a glovebox. The flask was transferred out of the glovebox and hooked to a schlenk line where it was heated at 333 K for 1 hour under N_2 flow.

50 µL of the Ga_2O_3 sol-gel solution was spun-cast onto a ZnO nanowire substrate and the substrate was dried by heating in air at 363 K for 10 min and then at 573 K for 20 min. One deposition resulted in a layer of amorphous Ga_2O_3 approximately 6 nm thick (Figure 60). The deposition could be repeated to increase the thickness of the Ga_2O_3 shell. However, due to the low viscosity of the Ga_2O_3 sol-gel solution, much of the solution went to the bottom of the substrate rather than sticking to the surface of the nanowires, resulting in a gradual build-up of a Ga_2O_3 film at the base of the nanowires. Once the desired Ga_2O_3 film thickness was

deposited, the nanowires were annealed in air to produce GZO superlattice and $ZnGa_2O_4$ nanowires.

3.6.b.ii – Structural Analysis of $M_2O_3(ZnO)_n$ Nanowires (III)

The annealing temperature was critical in determining the final composition of the nanowires. The composition of the nanowires was followed using XRD (Figure 61). Below 600°C all the nanowires exhibited XRD diffraction patterns characteristic of ZnO. Starting at 600°C peaks corresponding to the spinel crystal structure of $ZnGa_2O_4$ started to appear. At 900°C the Ga_2O_3 started to crystallize and the ZnO nanowires started to degrade. Although it was not clear at the time these experiments were performed, it's likely that many of the samples contained superlattice nanowires. As seen in Figures 31 and 54, polytypoid superlattice nanowires exhibit diffraction patterns similar to pure ZnO.

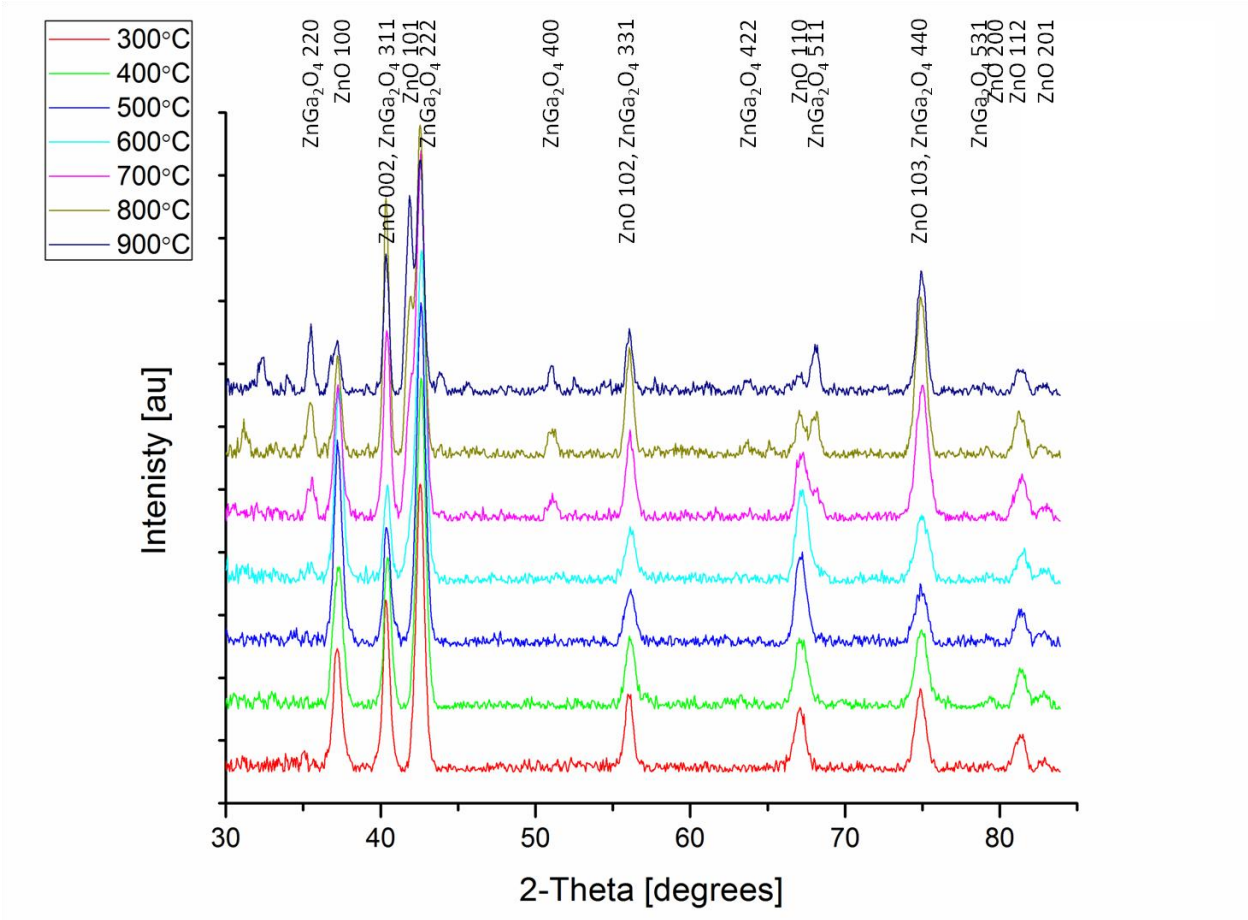

Figure 61 – XRD patterns of ZnO/Ga_2O_3 nanowires after annealing for 1 hour at various temperatures: XRD patterns showing a change in structure with increasing annealing temperature. The pattern gradually changes from that of a pure wurtzite structure to a mixture of wurtzite and spinnel ($ZnGa_2O_4$) at 600°C, to a mixture of wurtzite, spinel, and β-Ga_2O_3 at 900°C. The unlabeled peaks belong to Ga_2O_3.

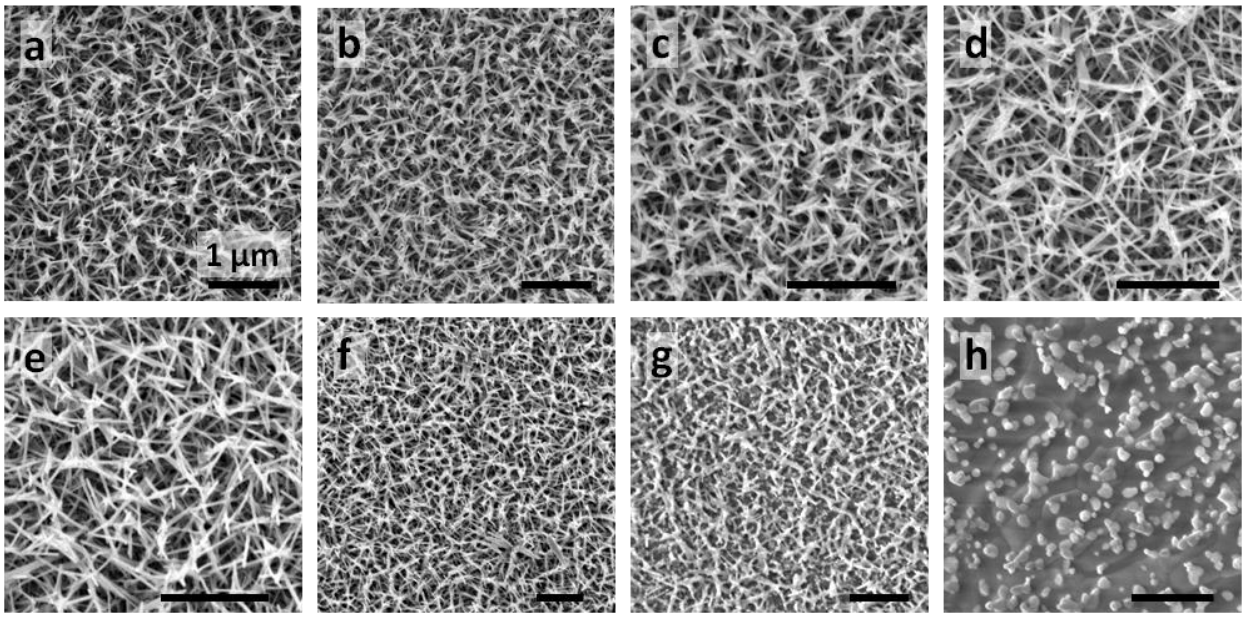

Figure 62 – SEM images of ZnO/Ga_2O_3 nanowire arrays annealed at different temperatures: SEM images of ZnO/ Ga_2O_3 nanowires annealed in air for 1 hour at (a) 300°C, (b)400°C, (c)500°C, (d)600°C , (e)700°C , (f)800°C , (g)900°C, and (h)1050°C.

SEM images of the samples show retention of the nanowire morphology up to 800°C (Figure 62). At 900°C, where crystalline β-Ga_2O_3 starts to form, there is an obvious degradation of the ZnO, and at 1050°C there is a complete loss of the nanowire morphology. The original goal of this research project was to synthesize $ZnGa_2O_4$ by conversion chemistries. Since the XRD pattern shows the introduction of $ZnGa_2O_4$ peaks at 700°C, 700°C was chosen for further experiments.

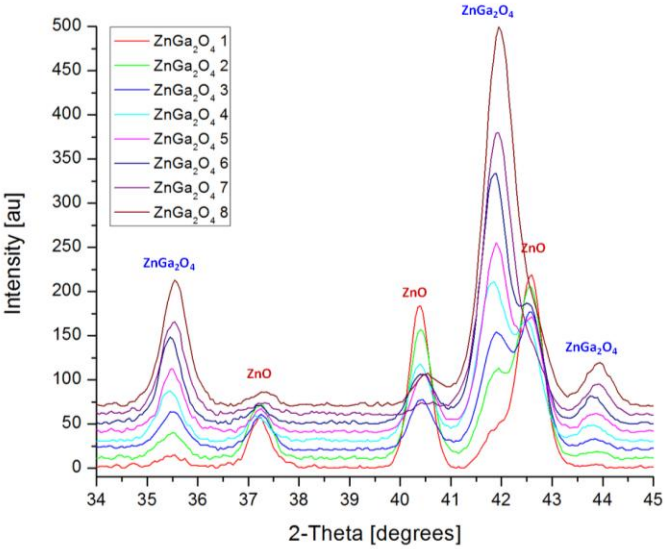

Figure 63 – XRD patterns of annealed ZnO/Ga_2O_3 nanowires with different amounts of Ga_2O_3 deposition: XRD patterns of annealed nanowires with 1-8 Ga_2O_3 depositions showing a gradual change from a wurtzite ZnO-like structure to a spinel $ZnGa_2O_4$ structure.

In addition to using temperature to control the conversion, the amount of Ga_2O_3 is also important. To generate the spinel structure, the correct ratio of Zn:Ga (1:2) must exist. Thus, if the amount of Ga_2O_3 is too small the conversion will be incomplete. This can be seen in the XRD patterns in Figure 63. For these nanowire samples, sol-gel Ga_2O_3 was deposited up to 8 times before annealing the samples in air for 1 hour at 700°C. As the amount of Ga_2O_3 is increased there is a gradual change from wurtzite to $ZnGa_2O_4$ spinnel. Unfortunately, with higher amounts of

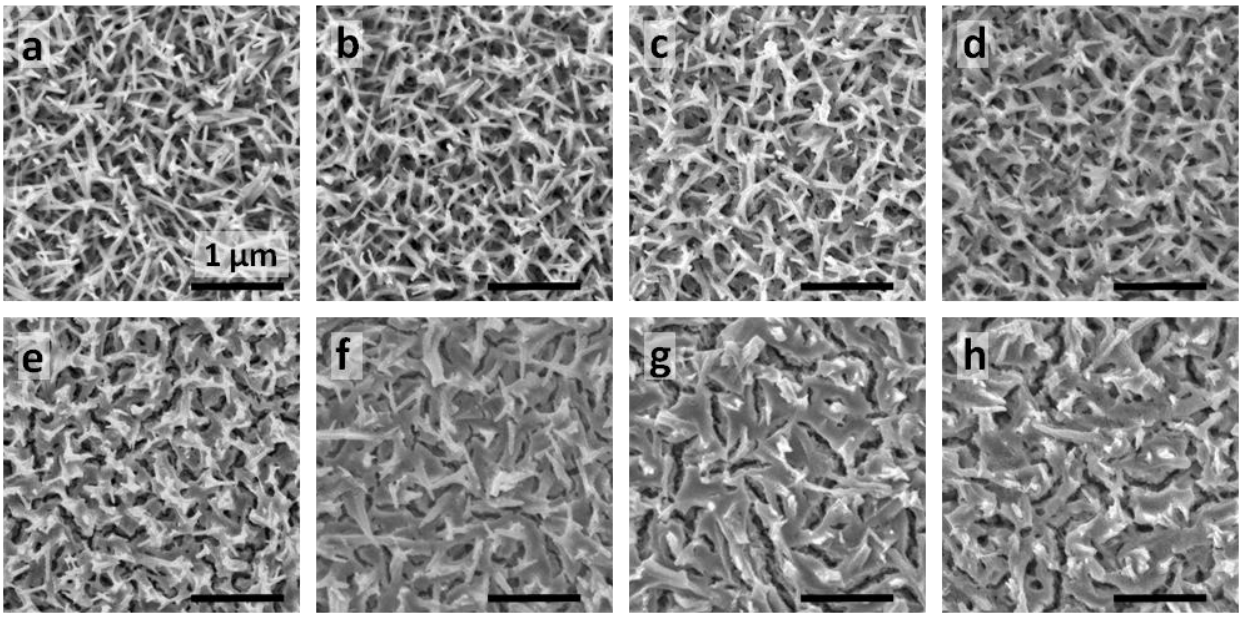

Figure 64 – SEM images of ZnO/Ga_2O_3 nanowire arrays annealed at 700°C with different amounts of Ga_2O_3 deposition: SEM images of annealed nanowires with (a) 1, (b)2, (c)3, (d)4, (e)5, (f)6, (g)7, and (h)8 Ga_2O_3 depositions.

Ga_2O deposition there is also a loss of nanowire morphology (Figure 64).

Although, this conversion method was not especially successful for the generation of $ZnGa_2O_4$ nanowires, serendipitously, it turned out to be successful in generating $Ga_2O_3(ZnO)_n$ nanowires. The superlattice morphology can be seen in the nanowires with lesser amounts of Ga_2O_3 deposition (Figure 65). It would be interesting to return to these experiments and see if the inclusion density could be tuned using different synthetic conditions, such as annealing time, temperature, and amount of Ga_2O_3 deposition. Also, since it's possible to make a wide range of metal oxides by sol-gel techniques, it's likely that other types of superlattices could be generated by this method.

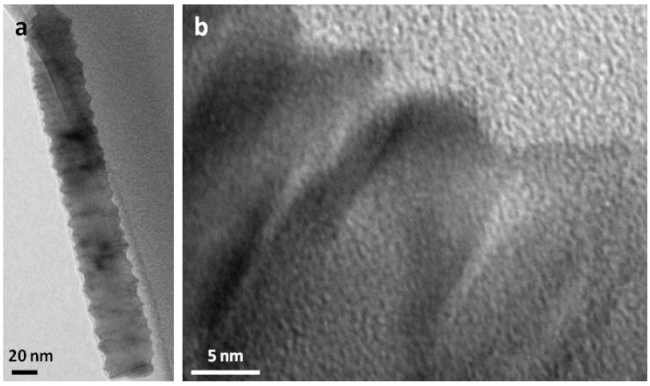

Figure 65 – TEM images of GZO nanowires prepared by sol-gel deposition of Ga_2O_3 on ZnO: (a) Low-magnification, and (b) high-magnification images of GZO nanowires prepared using 3 depositions of Ga_2O_3 and 1 hour of air annealing at 700°C.

3.6.b.iii –$M_2O_3(ZnO)_n$ Nanowires Synthesized by Solid-State Diffusion (III): Conclusions

The preparation of GZO nanowires by sol-gel deposition of Ga_2O_3 is attractive since the majority of the synthesis is accomplished using solution-based processes. Additionally, the aqueous synthesis of ZnO nanowires lends this method towards a more environmentally friendly preparation of GZO nanowires. Additional experiments are necessary to determine the tunability of this method as well as whether or not this method may be applied to other metals in the $M_2O_3(ZnO)_n$ system.

3.7 – $M_2O_3(ZnO)_n$ Nanowires: Conclusions

$M_2O_3(ZnO)_n$ nanowires have been synthesized by three different methods. Synthesis by the first method was accomplished using metal nanoparticles deposited on the surfaces of the nanowires and a 900°C anneal in O_2. This method was successful in making IZO, IGZO, GZO, and IFZO nanowires and could possibly be extended to additional systems. Thermoelectric measurements found that the IGZO nanowires had an order of magnitude enhancement of the figure of merit compared to bulk IZO samples. Unfortunately, the PL of these samples was dominated by defect emission which is unfavorable for other applications, such as PEC water splitting. The second synthetic method achieved significantly better optical properties by cutting the high temperature O_2 anneal. Instead, GZO and IGZO nanowires were synthesized by annealing ZnO nanowires in metal vapors. The nanowires prepared by this method exhibited almost 100% band edge emission in their PL spectra. This indicates a low-density of oxygen defects within the nanowires. The third synthetic method used a primarily solution-based preparation of GZO nanowires, which is attractive for commercial manufacturing.

The unique structure and composition of these $M_2O_3(ZnO)_n$ nanowires opens the door to a variety of applications, such as thermoelectrics and photoelectrochemical water splitting. Future research on these materials should focus on the effects of the structure and composition on electrical and thermal transport properties, as well as optical properties. This may enable further enhancements in energy conversion efficiencies. In addition, many questions still remain regarding the precise nature of the structure of these materials. Further TEM analysis and diffraction experiments will be helpful in elucidating the exact locations and coordination environments of the *M* atoms within the superlattice, as well as exactly what conditions must be present within the material to general these structures.

3.8 – References

1. Yan, Y., et al., *Polytypoid structures in annealed In_2O_3-ZnO films.* Applied Physics Letters, 1998. **73**(18): p. 2585-2587.
2. Kimizuka, N., M. Isobe, and M. Nakamura, *Syntheses and single-crystal data of homologous compounds, $In_2O_3(ZnO)_m$ (m = 3, 4, and 5), $InGaO_3(ZnO)_3$, and $Ga_2O_3(ZnO)_m$*

(m = 7, 8, 9, and 16) in the In_2O_3–$ZnGa_2O_4$–ZnO system. Journal of Solid State Chemistry, 1995. **116**(1): p. 170-178.
3. Horlin, T., G. Svensson, and E. Olsson, *Extended defect structures in zinc oxide doped with iron and indium.* Journal of Materials Chemistry, 1998. **8**(11): p. 2465-2473.
4. Li, C.F., et al., *Antiphase modulated structure of $Fe_2O_3(ZnO)_{15}$ studied by high-resolution electron microscopy.* Journal of Solid State Chemistry, 1999. **142**(1): p. 174-179.
5. Kasper, V.H., Anorg. Allg, Chem., 1967. **349**: p. 113.
6. Da Silva, J.L.F., Y.F. Yan, and S.H. Wei, *Rules of structure formation for the homologous $InMO_3(ZnO)_n$ compounds.* Physical Review Letters, 2008. **100**(25): p. 255501.
7. Ding, Y., X.Y. Kong, and Z.L. Wang, *Doping and planar defects in the formation of single-crystal ZnO nanorings.* Physical Review B, 2004. **70**(23): p. 235408.
8. Yan, Y., et al., *Atomic structure of In_2O_3–ZnO systems.* Applied Physics Letters, 2007. **90**(26): p. 261904.
9. Li, C., et al., *A modulated structure of $In_2O_3(ZnO)_m$ as revealed by high-resolution electron microscopy.* Journal of Electron Microscopy, 1997. **46**(2): p. 119-127.
10. Isobe, M., et al., *Structures of $LuFeO_3(ZnO)_m$ (m=1, 4, 5 and 6).* Acta Crystallographica Section C, 1994. **50**(3): p. 332-336.
11. Cheng, H., et al., *Characterization of Al-doped ZnO thermoelectric materials prepared by RF plasma powder processing and hot press sintering.* Ceramics International, 2009. **35**(8): p. 3067-3072.
12. Yuan, G.-D., et al., *Tunable n-type conductivity and transport properties of Ga-doped ZnO nanowire arrays.* Advanced Materials, 2008. **20**(1): p. 168-173.
13. Tsubota, T., et al., *Thermoelectric properties of Al-doped ZnO as a promising oxide material for high-temperature thermoelectric conversion.* Journal of Materials Chemistry, 1997. **7**(1): p. 85-90.
14. Ohtaki, M., K. Araki, and K. Yamamoto, *High Thermoelectric Performance of Dually Doped ZnO Ceramics.* Journal of Electronic Materials, 2009. **38**(7): p. 1234-1238.
15. Ohta, H., W.S. Seo, and K. Koumoto, *Thermoelectric properties of homologous compounds in the ZnO-In2O3 system.* Journal of the American Ceramic Society, 1996. **79**(8): p. 2193-2196.
16. Kaga, H., R. Asahi, and T. Tani, *Thermoelectric properties of highly textured Ca-doped (ZnO)(m)In2O3 ceramics.* Japanese Journal of Applied Physics Part 1-Regular Papers Short Notes & Review Papers, 2004. **43**(10): p. 7133-7136.
17. Kudo, A. and I. Mikami, *New In2O3(ZnO)(m) photocatalysts with laminal structure for visible light-induced H-2 or O-2 evolution from aqueous solutions containing sacrificial reagents.* Chemistry Letters, 1998. **27**(10): p. 1027-1028.
18. Jie, J.S., et al., *Synthesis and characterization of ZnO : In nanowires with superlattice structure.* Journal of Physical Chemistry B, 2004. **108**(44): p. 17027-17031.
19. Wu, L.L., et al., *Synthesis and optical properties of ZnO nanowires with a modulated structure.* Journal of Physics D-Applied Physics, 2008. **41**(19): p. 195406.
20. Zhang, X.T., et al., *Crystal Structure of In2O3(ZnO)(m) Superlattice Wires and Their Photoluminescence Properties.* Crystal Growth & Design, 2009. **9**(1): p. 364-367.

21. Na, C.W., S.Y. Bae, and J. Park, *Short-period superlattice structure of Sn-doped In2O3(ZnO)(4) and In2O3(ZnO)(5) nanowires.* Journal of Physical Chemistry B, 2005. **109**(26): p. 12785-12790.
22. Li, D.P., et al., *Synthesis and Photoluminescence of InGaO3(ZnO)(m) Nanowires with Perfect Superlattice Structure.* Journal of Physical Chemistry C, 2009. **113**(52): p. 21512-21515.
23. Hsu, C.L., et al., *Influence of the formation of the second phase in ZnO/Ga nanowire systems.* Journal of the Electrochemical Society, 2006. **153**(4): p. G333-G336.
24. Huang, D.L., L.L. Wu, and X.T. Zhang, *Size-Dependent InAlO3(ZnO)(m) Nanowires with a Perfect Superlattice Structure.* Journal of Physical Chemistry C, 2010. **114**(27): p. 11783-11786.
25. Huang, M.H., et al., *Room-temperature ultraviolet nanowire nanolasers.* Science, 2001. **292**(5523): p. 1897-1899.
26. Jie, J.S., et al., *Synthesis and characterization of ZnO:In nanowires with superlattice structure.* Journal of Physical Chemistry B, 2004. **108**(44): p. 17027-17031.
27. Thomas, D.G., *The diffusion and precipitation of indium in zinc oxide.* Journal of Physics and Chemistry of Solids, 1959. **9**(1): p. 31-42.
28. Broser, I., et al., *Physics of II-VI and I-VII Compounds, Semimagnetic Semiconductors*. Landolt-Börnstein: Numerical Data and Functional Relationships in Science and Technology. Vol. 17. 1982, New York: Springer-Verlag.
29. Erhart, P. and K. Albe, *Diffusion of zinc vacancies and interstitials in zinc oxide.* Applied Physics Letters, 2006. **88**(20): p. 201918-3.
30. Nakagawa, T., et al., *Analysis of indium diffusion profiles based on the Fermi-level effect in single-crystal zinc oxide.* Japanese Journal of Applied Physics, 2008. **47**(10): p. 7848.
31. Nakagawa, T., et al., *Diffusion model of gallium in single-crystal ZnO proposed from analysis of concentration-dependent profiles based on the Fermi-level effect.* Japanese Journal of Applied Physics, 2007. **46**(7A): p. 4099.
32. Popovici, G., et al., *Impurity contamination of GaN epitaxial films from the sapphire, SiC and ZnO substrates.* Applied Physics Letters, 1997. **71**(23): p. 3385-3387.
33. Li, C., et al., *Relation between In ion ordering and crystal structure variation in homologous compounds $InMO_3(ZnO)_m$ (M=Al and In; m=integer).* Micron, 2000. **31**(5): p. 543-550.
34. Hochbaum, A.I., et al., *Enhanced thermoelectric performance of rough silicon nanowires.* Nature, 2008. **451**(7175): p. 163-167.
35. Li, D., et al., *Thermal conductivity of Si/SiGe superlattice nanowires.* Applied Physics Letters, 2003. **83**(15): p. 3186-3188.
36. Lin, Y. and M. Dresselhaus, *Thermoelectric properties of superlattice nanowires.* Phys. Rev. B, 2003. **68**(7): p. 075304.
37. Nomura, K., et al., *Thin-film transistor fabricated in single-crystalline transparent oxide semiconductor.* Science, 2003. **300**(5623): p. 1269-1272.
38. Nomura, K., et al., *Carrier transport in transparent oxide semiconductor with intrinsic structural randomness probed using single-crystalline $InGaO_3(ZnO)_5$ films.* Applied Physics Letters, 2004. **85**(11): p. 1993-1995.

39. Shakouri, A., et al., *Thermoelectric effects in submicron heterostructure barriers.* Microscale Therm Eng, 1998. **2**(1): p. 37-47.
40. Whitlow, L.W. and T. Hirano, *Superlattice applications to thermoelectricity.* Journal of Applied Physics, 1995. **78**(9): p. 5460-5466.
41. Hicks, L.D. and M.S. Dresselhaus, *Thermoelectric figure of merit of a one-dimensional conductor.* Physical Review B, 1993. **47**(24): p. 16631.
42. Ohta, H., R. Huang, and Y. Ikuhara, *Large enhancement of the thermoelectric Seebeck coefficient for amorphous oxide semiconductor superlattices with extremely thin conductive layers.* Phys Status Solidi-R, 2008. **2**(3): p. 105-107.
43. Senger, R. and K. Bajaj, *Optical properties of confined polaronic excitons in spherical ionic quantum dots.* Phys. Rev. B, 2003. **68**(4): p. 045313.
44. Tsubota, T., et al., *Thermoelectric properties of Al-doped ZnO as a promising oxide material for high-temperature thermoelectric conversion.* J Mater Chem, 1997. **7**(1): p. 85-90.
45. Malochkin, O., W.S. Se, and K. Koumoto, *Thermoelectric properties of $(ZnO)_5In_2O_3$ single crystal grown by a flux method.* Japanese Journal of Applied Physics Part 2-Letters, 2004. **43**(2A): p. L194-L196.
46. Gleskova, H., et al., *Field-effect mobility of amorphous silicon thin-film transistors under strain.* Journal of Non-Crystalline Solids, 2004. **338-340**: p. 732-735.
47. Alahmed, Z. and H. Fu, *Polar semiconductor ZnO under inplane tensile strain.* Physical Review B, 2008. **77**(4): p. 045213.
48. Chen, G., A. Narayanaswamy, and C. Dames, *Engineering nanoscale phonon and photon transport for direct energy conversion.* Superlattice Microst, 2004. **35**(3-6): p. 161-172.
49. Shi, L., et al., *Measuring thermal and thermoelectric properties of one-dimensional nanostructures using a microfabricated device.* Journal of Heat Transfer, 2003. **125**(5): p. 881-888.
50. Ozgur, U., et al., *Thermal conductivity of bulk ZnO after different thermal treatments.* J Electron Mater, 2006. **35**(4): p. 550-555.
51. Kaga, H., R. Asahi, and T. Tani, *Thermoelectric properties of highly textured Ca-doped $(ZnO)_mIn_2O_3$ ceramics.* Japanese Journal of Applied Physics, 2004. **43**(Copyright (C) 2004 The Japan Society of Applied Physics): p. 7133.
52. Chiritescu, C., et al., *Ultralow thermal conductivity in disordered, layered WSe2 crystals.* Science, 2007. **315**(5810): p. 351-353.
53. Fang, L., et al., *Thermoelectric and magnetothermoelectric properties of In-doped nano-ZnO thin films prepared by RF magnetron sputtering.* Journal of Superconductivity and Novel Magnetism, 2010. **23**(6): p. 889-892.
54. Li, C.F., et al., *Structure analysis of new homologous compounds Ga2O3(ZnO)(m) (m = integer) by high-resolution analytical transmission electron microscopy.* Acta Crystallographica Section B-Structural Science, 1999. **55**: p. 355-362.
55. Kimizuka, N., M. Isobe, and M. Nakamura, *Syntheses and Single-Crystal Data of Homologous Compounds, In2o3(Zno)(M) (M=3, 4, and 5), Ingao3(Zno)(3), and Ga2o3(Zno)(M) (M=7, 8, 9, and 16) in the In2o3-Znga2o4-Zno System.* Journal of Solid State Chemistry, 1995. **116**(1): p. 170-178.

56. Michiue, Y., N. Kimizuka, and Y. Kanke, *Structure of Ga2O3(ZnO)(6): a member of the homologous series Ga2O3(ZnO)(m).* Acta Crystallographica Section B-Structural Science, 2008. **64**: p. 521-526.
57. Nakamura, M., et al., *The Phase-Relations in the In2o3-Al2zno4-Zno System at 1350-Degrees-C.* Journal of Solid State Chemistry, 1993. **105**(2): p. 535-549.
58. Da Silva, J.L.F., A. Walsh, and S.H. Wei, *Theoretical investigation of atomic and electronic structures of Ga2O3(ZnO)(6).* Physical Review B, 2009. **80**(21): p. 214118.
59. Greene, L.E., et al., *Low-temperature wafer-scale production of ZnO nanowire arrays.* Angewandte Chemie-International Edition, 2003. **42**(26): p. 3031-3034.
60. Haase, M., H. Weller, and A. Henglein, *Photochemistry and Radiation-Chemistry of Colloidal Semiconductors .23. Electron Storage on Zno Particles and Size Quantization.* Journal of Physical Chemistry, 1988. **92**(2): p. 482-487.
61. Kokubun, Y., et al., *Sol-gel prepared beta-Ga2O3 thin films for ultraviolet photodetectors.* Applied Physics Letters, 2007. **90**(3): p. 031912.

Chapter 4:

$(Ga_{1-x}Zn_x)(N_{1-x}O_x)$ and $(In_{1-x-y}Ga_yZn_x)(N_{1-x}O_x)$ Nanotubes

4.1 – Introduction to Oxynitride Materials

Over the last several years that has been an explosion of research in the field of oxynitride materials, especially from Kazunari Domen's group at the University of Tokyo. The development of these oxynitrides has mainly focused on the discovery of new materials for photoelectrochemical water splitting. As discussed in 1.3.b there are several criteria that a semiconductor must meet in order to achieve efficient water splitting: 1) bandgap around 2.0 eV, 2) conduction band minimum (CBM) more negative than the H^+ to H_2 reduction potential, 3) valence band maximum (VBM) more positive than the H_2O to O_2 oxidation potential, 4) stability under photoelectrochemical conditions, and 5) efficient charge separation. Over the years a variety of metal oxides having metals with either a d^0 or a d^{10} configuration, including TiO_2[1,2], $BaTa_2O_6$[3], $NaTaO_3$:La[4], and $ZnGaO_4$[5], have been investigated as photocatalysts. Unfortunately they all share the common characteristic that their valence bands are composed of O2p orbitals which are located ~3V positive of the H^+/H_2 reduction potential[6]. Thus, if d^0 or d^{10} oxides are to be used for overall water splitting their bandgaps must be at least 3 eV, rendering them unable to absorb visible light. However, Domen's group found that oxynitrides, which are generally formed by the nitridation of the constituent oxide materials, exhibit reduced band gaps as a result of the addition of N2p character to the valence band[6].

One of the most exciting materials developed in Domen's group is the solid solution of GaN and ZnO, or $(Ga_{1-x}Zn_x)(N_{1-x}O_x)$ (denoted GaN:ZnO)[7]. DFT calculations by Wei et al. and Maeda et al. found that the top of the valence band consists of N2p orbitals and to a lesser extent, Zn3d and O2p orbitals[8,9]. The p-d repulsion between the N2p and Zn3d causes the VBM to shift upwards. However, the bottom of the conduction band, which consists of hybridized Ga 4s and 4p orbitals, remains in its original position, negative of the H^+/H_2 reduction potential. By varying the ZnO composition of the GaN:ZnO, the band gap can be tuned from 3.4 to 2.43 eV[10].

Since GaN and ZnO both crystallize in the wurtzite structure and have similar lattice constants, it's not surprising that they could form a solid solution. This was confirmed experimentally by several different methods. XRD patterns taken of the GaN:ZnO show wurtzite peaks with lattice constants intermediate between pure ZnO and GaN. The peaks shift with changing composition indicating that the GaN:ZnO is a solid solution rather than simply a physical mixture of GaN and ZnO[11]. Rietveld analysis of neutron diffraction patterns taken of

the GaN:ZnO further confirmed that O directly replaces N within the lattice[12]. Inductively coupled plasma optical emission spectroscopy (ICP-OES) was used to determine the elemental makeup of the GaN:ZnO and showed a 1:1 correlation between Ga and N as well as Zn and O confirming the $(Ga_{1-x}Zn_x)(N_{1-x}O_x)$ formula[12]. Additional analysis by TEM revealed that the particulates were well crystallized and individual particulates showed single-crystal electron diffraction patterns[13]. Based on this extensive analysis it can be concluded that GaN:ZnO materials are very attractive for photoelectrochemical water splitting applications.

4.2 – Photoelectrochemical Water Splitting with $(Ga_{1-x}Zn_x)(N_{1-x}O_x)$

The first report on overall photoelectrochemical water splitting by a single material under visible light was reported by Maeda et al in 2005[7]. The photocatalyst was GaN:ZnO decorated with RuO_2 cocatalysts. Unfortunately, the apparent quantum efficiency in the 300-480 nm range was only 0.14%. However, in 2006, the RuO_2 H^+ reduction cocatalyst was replaced with a $Rh_{2-y}Cr_yO_3$ cocatalyst, increasing the apparent quantum efficiency to 2.5% in the 420-440 range[10]. More recently, a post calcination step was used to improve the crystallinity of the GaN:ZnO, bumping the apparent quantum efficiency to 5.9%[14]. This remains as the highest reported quantum efficiency for overall visible-light-driven water splitting by a single photocatalyst.

An in-depth analysis of the GaN:ZnO preparation conditions and the subsequent H_2 and O_2 production found that the degree of crystallization was extremely important in determining the water splitting activity[13]. Generally, GaN:ZnO is prepared by mixing ZnO and Ga_2O_3 powders and heating them under NH_3 flow. Maeda et al. found that the activity increased with increasing nitridation time (and increasing crystallinity), up to about 15 hours, after which the activity decreased due to the formation of Zn vacancies on the surface. The vacancies can act as recombination centers, limiting the water splitting activity. The final GaN:ZnO particle morphology was also important. When the final particles were smooth and more regular in shape they exhibited higher activities. The assumption is that particles with rougher surfaces and irregular shapes also contain more surface trap states and thus more recombination centers. Maeda et al. found that the particle size of the starting ZnO powder has a large effect on the water splitting activity since intimate contact between the ZnO and Ga_2O_3 precursors were necessary to achieve a homogenous sample[13]. In addition, higher ratios of ZnO in the starting material was found to promote crystallization of the GaN:ZnO. Despite the significant improvements made to the GaN:ZnO by optimizing the preparation conditions, over 90% of the photogenerated carriers within the material recombined before participating in the water splitting reaction[13].

Based on the observations by Maeda et al[13], it's clear that several key issues need to be addressed if further improvements are to be made in the GaN:ZnO system. First, the material should be single-crystalline with the lowest density of defects possible. The material should also be homogenous, which appears to be facilitated by intimate contact between the

precursors. Currently, GaN:ZnO with x=0.18 produces the highest water splitting efficiency[14], despite the visible absorption being considerably lower that the x=0.42 samples. Unfortunately the poorer crystallinity of the x=0.42 samples contributes to a larger percentage of recombination in the photogenerated charges. In addition to improving the crystallinity, recombination can be suppressed by reducing the distance that photogenerated charges must travel before they reach the surface. As discussed in section 1.3.b, this can be accomplished using nanostructured materials with high surface area. The high surface area could also promote more intimate contact between precursors to produce a more homogenous final product. Thus, the development of a synthesis for single-crystalline, defect-free GaN:ZnO nanomaterials with low bandgaps is of particular interest.

4.3 – Synthesis of GaN Nanotubes

Single-crystal nanotubes are especially attractive for photoelectrochemical water splitting applications. Oriented nanotubes have long optical path lengths and extremely high surface areas, enabling complete light absorption and promoting good charge separation. Numerous reports exist on the synthesis of inorganic nanotubes[15,16] and single-crystal GaN nanotubes in particular[17-21]. In 2003 Goldberger et al. reported the first synthesis of single-crystal GaN nanotube arrays by an epitaxial casting method[22]. The GaN nanotubes were synthesized by starting with a ZnO nanowire array template and coating it with GaN using metal organic chemical vapor deposition (MOCVD). Finally, the ZnO cores were removed by heating the core/shell nanowires in a H_2 atmosphere, leaving behind the GaN shells. Due to interfacial diffusion between the ZnO and GaN the final GaN nanotubes contained a small amount of Zn and O impurities. However, most of the ZnO could be removed by prolonged heating in NH_3. Using a more complicated deposition procedure requiring 5 separate depositions of GaN, Thapa et al. synthesized GaN nanotubes without Zn or O impurities[23]. The color of their nanotubes was white instead of the yellow, indicating a more defect-free GaN.

Based on these previous reports, it's clear that Zn and O are readily introduced into GaN nanotubes grown by epitaxial casting on ZnO nanowires. Despite the great care that was taken by these researchers to remove the ZnO, the incorporation of ZnO into GaN to generate $(Ga_{1-x}Zn_x)(N_{1-x}O_x)$ nanotubes is interesting as a possible new water splitting material.

4.4 – $(Ga_{1-x}Zn_x)(N_{1-x}O_x)$ Nanotubes

GaN:ZnO currently holds the record for the highest efficiency of simultaneous H_2 and O_2 production at λ>420 nm[14]. Therefore, further improvements, no matter how marginal, would be exciting. The synthesis of GaN:ZnO nanotubes by an epitaxial casting method could produce single crystal nanotubes with high uniformity, good crystallinity, and high surface area, facilitating efficient charge separation and high activity for overall photoelectrochemical water splitting.

4.4.a – Synthesis of $(Ga_{1-x}Zn_x)(N_{1-x}O_x)$ Nanotubes

GaN:ZnO nanotubes have been synthesized by two slightly different procedures. The first procedure (Method 1) is used to generate GaN:ZnO nanotube arrays with electrical continuity to the back contact for the purpose of photocurrent measurements. The second procedure (Method 2) can generate larger amounts of GaN:ZnO nanotubes to be used for water splitting measurements via GC detection of H_2 and O_2.

4.4.a.i – $(Ga_{1-x}Zn_x)(N_{1-x}O_x)$ Nanotube Synthesis – Method 1

GaN:ZnO nanotubes were prepared using an epitaxial casting method, similar to that reported by Goldberger et al[22]. The general procedure is shown in Figure 66. ZnO nanowire arrays were coated with GaN using metal organic vapor deposition (MOCVD) and then the ZnO

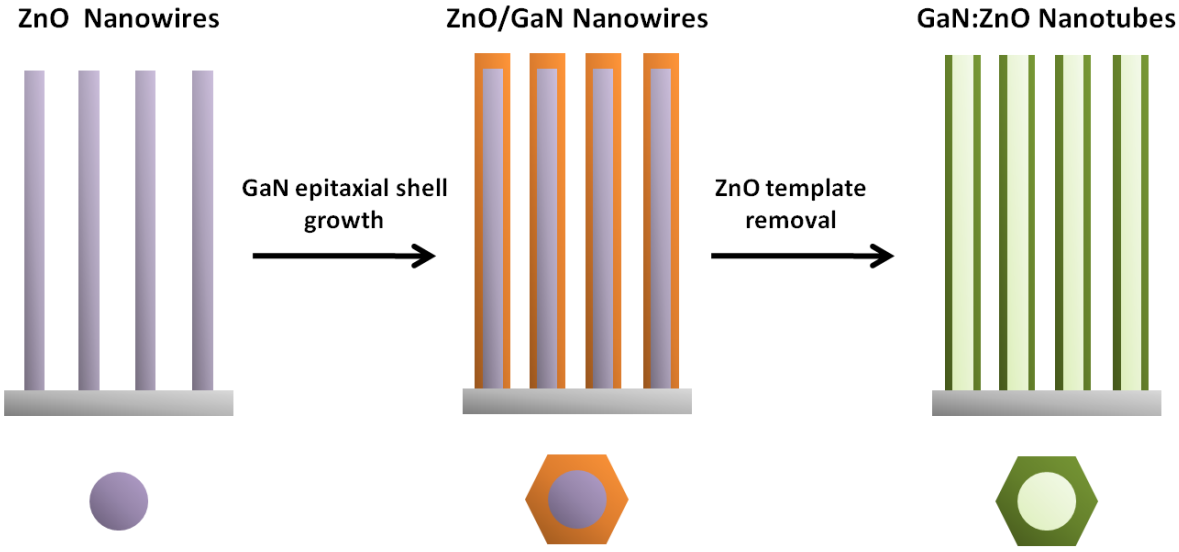

Figure 66 – Schematic of Method 1: Schematic showing the synthetic procedure used to generate oriented arrays of GaN:ZnO nanotube arrays for photocurrent measurements.

nanowire templates were removed, leaving behind GaN:ZnO nanotube arrays. A more detailed procedure is given below.

First, ZnO nanowire arrays were prepared using the procedure described in 3.6.b.i except that the ZnO seed layer was generated using a solution casting of ZnO precursors rather than the deposition of ZnO nanoparticle seeds. In this case, the ZnO layer was formed by drop-casting a solution of Zn acetate is absolute ethanol onto the desired substrate. Before the solution was allowed to dry completely, the substrate was rinsed with ethanol and dried under a stream of N_2. This process was repeated for a total of 4 depositions and then the films were annealed in air at 300°C for 25 min to generate ZnO. This entire deposition and annealing

process was repeated a second time to ensure the formation of a uniform ZnO film. The high degree of orientation of the solution-deposited ZnO films promoted the growth of vertical [002]-oriented ZnO nanowire arrays[24].

GaN was deposited onto the ZnO nanowire arrays using a home-built system consisting of a Lindberg-blue tube furnace with a 1-in quartz tube and ¼-in inner quartz tube used for the delivery of the trimethyl gallium (TMG) precursor. The TMG was stored in a bubbler and cooled to -10.9 °C. A 5 sccm flow of N_2 was bubbled through the TMG and then further diluted with 150 sccm of N_2. At the output of the inner quartz tube the TMG precursor was reacted with 20 sccm of NH_3 to produce GaN. The ZnO nanowire array substrates were positioned 0.5 cm in front of the inner quartz tube. The furnace was heated to 600°C under NH_3 before the TMG and N_2 flows were turned on. After a 90 sec growth time the TMG and NH_3 were switched off and the substrates were heated for 10 min at 600°C before being cooled to room temperatures. To create hollow nanotubes the ZnO/GaN core/shell nanowires were etched in NH_3 at 700°C for 40 min.

4.4.a.ii - $(Ga_{1-x}Zn_x)(N_{1-x}O_x)$ Nanotube Synthesis – Method 2

For the second method, nanowire films were used rather than nanowire arrays to enable the preparation of larger amount of GaN:ZnO nanotubes (Figure 67). The ZnO nanowires were synthesized using a protocol similar to that reported by Yuhas et al[25]. 0.486 g of anhydrous Zn acetate (Aldrich), 101 µL of oleic acid (99%), and 25 mL of trioctylamine (98%) were combined in a 50 mL single-neck, round bottom flask that was fitted with a condenser. The flask was lowered into a pre-heated silicone oil bath at 300°C. After heating the precursor solution (under stirring) for about 15 minutes, the zinc acetate dissolved to give a clear solution. The solution turned white after an additional 30 minutes signaling the nucleation of the ZnO nanowires. To achieve nanowires of the desired length the solution was heated for an additional 45 min. Once the reaction was complete the flask was removed from the oil bath and allowed to cool to room temperature. The triocylamine was poured off the top of the flask and the product was washed 3 times in ethanol.

The ZnO nanowires were suspended in ethanol and sonicated for 60 min to break apart

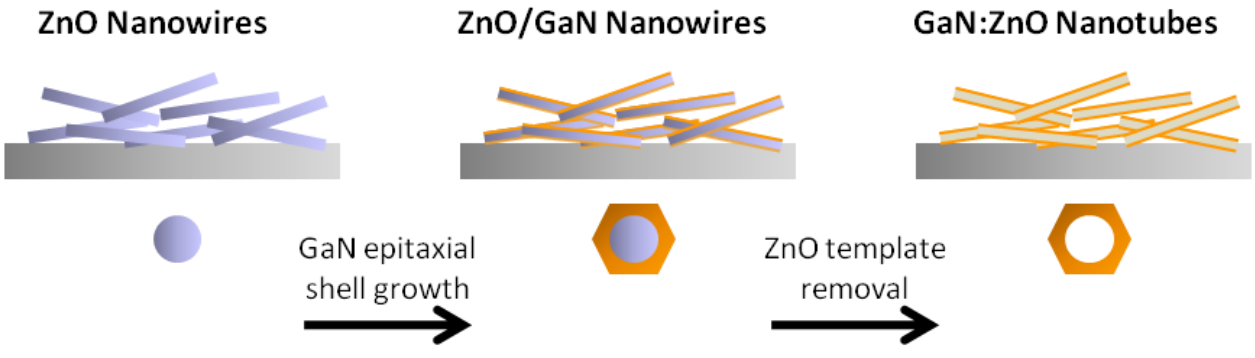

Figure 67 – Schematic of Method 2: Schematic showing the synthetic procedure used to generate GaN:ZnO nanotube films for GC measurements.

any nanowire bundles. Double-polished quartz substrates were cut in 1 x 1 cm pieces and cleaned by sonication in isopropanol and acetone. The ZnO nanowire solution was dropcast on the quartz pieces and slowly dried to produce uniform films of ZnO nanowires. The film thickness depended in the concentration of the ZnO solution.

GaN:ZnO nanotubes were generated via the ZnO nanowire templates using the same procedure described in Method 1. Afterwards the GaN:ZnO nanotubes were sonicated off the quartz into a solution of water and then sonicated for an additional 60 min to break apart the nanotube film. Centrifugation was used to isolate the nanotube product.

4.4.b – Structure and Composition of $(Ga_{1-x}Zn_x)(N_{1-x}O_x)$ Nanotubes

ZnO and GaN both crystallize into the wurtzite structure and have very similar lattice constants of a: 3.249 Å, c: 5.207 Å for ZnO and a: 3.189 Å, c: 5.185 Å for GaN. Due to the small amount of lattice mismatch between GaN and ZnO, GaN can be grown epitaxially on top ZnO and vice versa. For the generation of GaN:ZnO nanotubes, ZnO nanowire templates were used for the epitaxial casting of a single-crystal GaN layer. During the deposition of GaN by MOCVD, ZnO from the nanowire template was incorporated into the GaN layer creating an alloy of GaN and ZnO. The ZnO nanowire template was then etched away leaving GaN:ZnO nanotubes.

4.4.b.i – Characterization of $(Ga_{1-x}Zn_x)(N_{1-x}O_x)$ Nanotubes (Method 1)

The XRD peaks of the GaN:ZnO nanotubes generated by the first synthetic method (Figure 68) can be assigned to a wurtzite structure and are intermediate in position between ZnO and GaN, though they more closely resemble GaN. This indicates the formation of a solid solution of GaN and ZnO with a higher percentage of GaN. The 002 peak is dominant in the XRD pattern signifying the high degree of alignment within the GaN:ZnO nanotube arrays. The SEM images in Figure 69 follow the arrays through the synthetic procedure, starting first with the ZnO nanowires, then the ZnO/GaN – core/shell nanowires, and finally the GaN:ZnO nanotubes. As can be seen in Figures 69c and d, the tips of the nanotubes were open after the removal of the ZnO nanowire template. It's not clear at this time what causes the

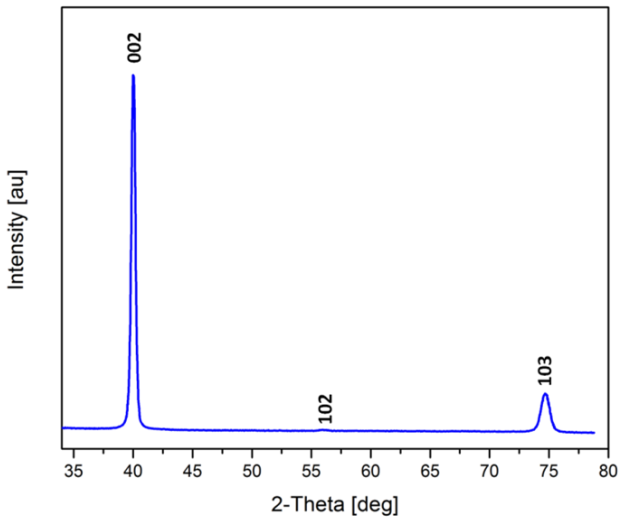

Figure 68 – XRD pattern of GaN:ZnO nanotubes synthesize by the 1st method: XRD pattern showing the high degree of alignment within the GaN:ZnO nanotubes.

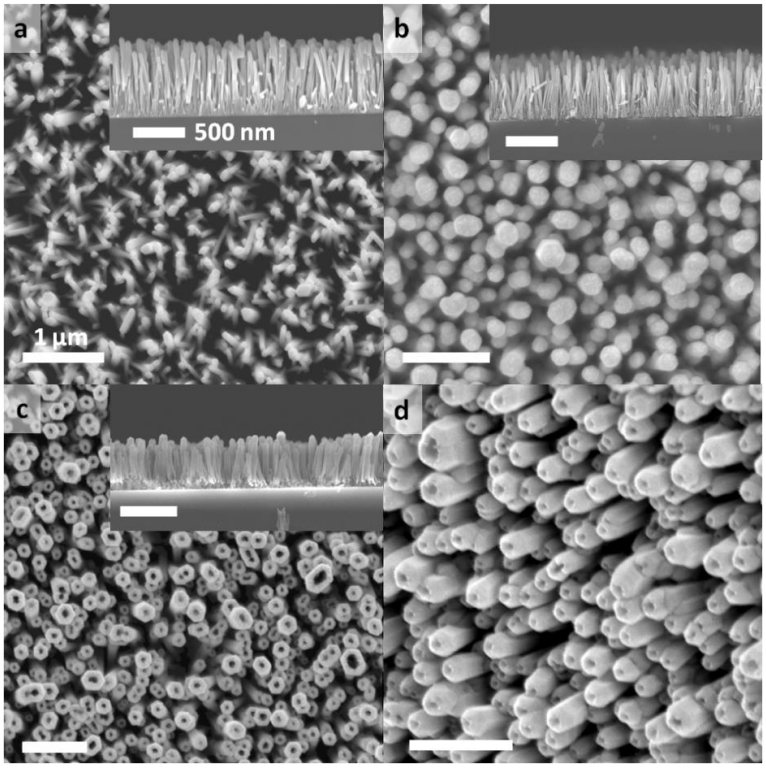

Figure 69 – SEM images of nanowire/nanotube arrays through the synthetic (Method 1) process: (a-c) Top-down and cross-sectional (inset) SEM images of (a) the starting ZnO nanowire array, (b) the ZnO/GaN-core/shell arrays, and (c) the GaN:ZnO nanotube arrays. (d) SEM image taken at a 45° tilt showing the open tips of the GaN:ZnO nanotubes.

nanotubes to open at the tips. However, this geometry is ideal for photoelectrochemical water splitting since the open tips will permit electrolyte to move feely inside the nanotubes allowing both the outer and inner surfaces to participate in water splitting.

A previous report on GaN nanotubes synthesized by epitaxial casting noted that the inner surfaces of the nanotubes were hexagonally faceted as a result of the hexagonal facets of the starting ZnO nanowire templates[22]. The outer surfaces of the nanotubes were smooth. The smaller ZnO nanowires used in this approach have less well-defined facets than the larger vapour phase grown ZnO nanowires. It is interesting to see in the SEM images is Figures 69c and d that the inner surface of these nanotubes is smooth while the outer surface is hexagonally faceted. The hexagonal facets on the outer surface indicate development of the wurtzite crystal habit. The hexagonal faceting can also be seen in top-down TEM images of the GaN:ZnO nanotubes (Figure 70a, inset).

TEM samples were prepared by sonicating the nanotube arrays into a solution of isopropanol and dropcasting

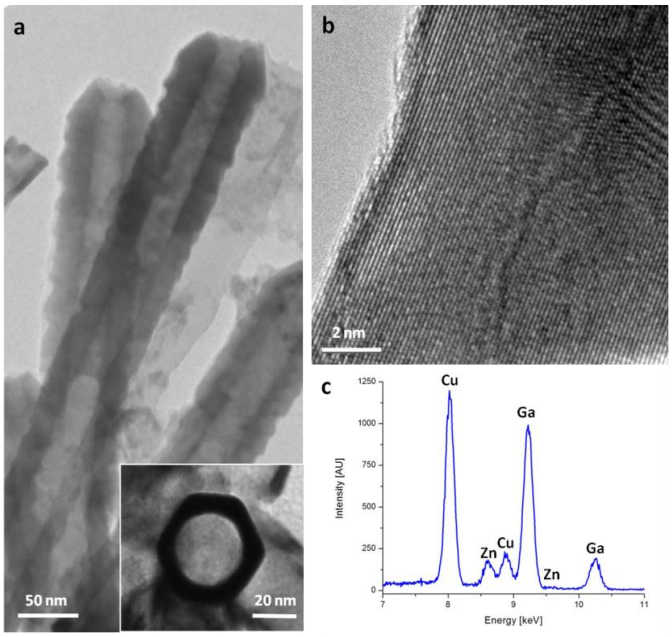

Figure 70 – TEM images and EDS spectrum of GaN:ZnO nanotubes (Method 1): (a) Low-magnification TEM images of a group of GaN:ZnO nanotubes. Inset is a top-down image showing the hexagonal facets on the outer surface of the nanotube. (B) HRTEM image of a GaN:ZnO nanotube displaying its single-crystallinity. (s) EDS spectrum showing the presence of both Ga and Zn within the nanotubes.

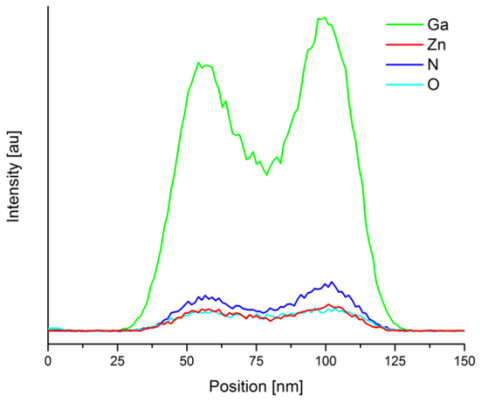

Figure 71 – EDS line profile of a GaN:ZnO nanotube: EDS profile across the diameter of a GaN:ZnO nanotube indicating that the nanotubes are indeed hollow in the center.

the solution on lacey carbon support grids. The nanotubes were completely open from tip to base (Figure 70a) and the dimensions were generally 40-50 nm for the inner tube diameter and 20 nm for the tube walls. HRTEM images of the nanotubes (Figure 70b) indicate that the epitaxial casting approach was successful in generating single-crystal GaN:ZnO nanotubes. The ZnO composition of the GaN:ZnO nanotube arrays could be controllably varied from approximately 10 to 1% (by EDS) by increasing the NH_3 etching time. To further confirm that the nanotubes were hollow in the center, an EDS line scan was taken across the diameter of a GaN:ZnO nanotube. As can be seen in Figure 71, the Ga, Zn, N, and O signals all peaked at the edges of the nanotubes and dipped to a minimum at the center. This profile is characteristic of a hollow nanotube geometry.

The structural and compositional characterization of the nanotubes prepared by Method 1 indicate that the synthesis was successful in generating single-crystal GaN:ZnO nanotubes with ZnO compositions up to 10%. The nanotubes were well-aligned on the substrates and had open tips which will allow electrolyte to reach both the inner and outer surfaces of the nanotubes for water splitting. Previous reports by Maeda et al. on GaN:ZnO photocurrent measurements indicate a large degree of difficulty in obtaining electrical contact to the powder as well as between particulates in the powder[26]. The nanotubes in our oriented arrays are electrically connected to one another and are also directly connected to the substrate. By growing these nanotubes on conductive substrate, such as Ti foil, it should be possible to measure the photocurrent of these arrays without any additional processing steps.

4.4.b.ii – Characterization of $(Ga_{1-x}Zn_x)(N_{1-x}O_x)$ Nanotubes (Method 2)

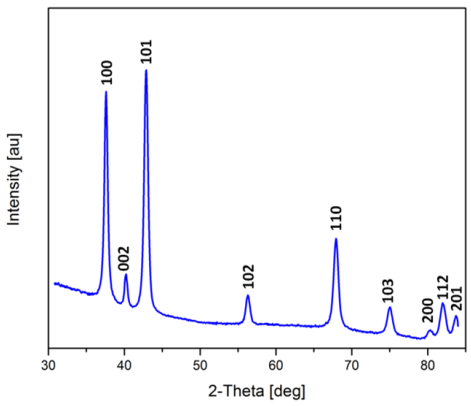

The XRD pattern on the GaN:ZnO nanotubes grown by Method 2 (Figure 72) is similar to that of the nanotubes synthesized by Method 1. However, the pattern from the nanotube films is of a powder sample rather than an oriented sample, so all the wurtzite peaks are evident. SEM images (Figures 73) through the synthetic procedure show a thickening of the

Figure 72 – XRD pattern of GaN:ZnO nanotubes synthesized by the 2nd method: XRD pattern showing a wurtzite crystal structure corresponding to a solid solution of GaN and ZnO.

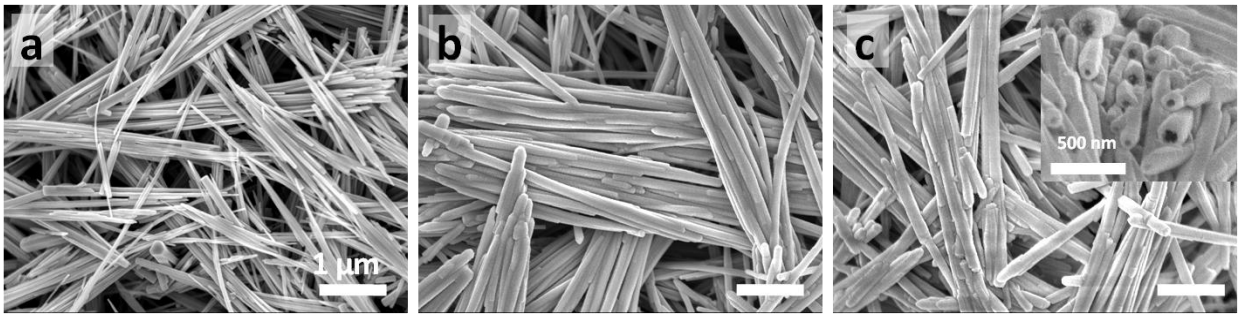

Figure 73 – SEM images of nanowire/nanotube arrays through the synthetic (Method 2) process: SEM images of (a) ZnO nanowire film, (b) ZnO/GaN – core/shell nanowire films, and (c) GaN:ZnO nanotube film. Inset is a cross-sectional view of the film showing the open tips of the GaN:ZnO nanotubes.

nanowires after GaN deposition. Depending on the thickness of the ZnO nanowire film, the nanowires on the bottom of the film may not be coated with GaN. These uncoated nanowires are simply etched away with the rest of the ZnO templates in the final step. Once the ZnO templates are removed the tips of the nanotubes open (Figure 73c, inset), similar to the oriented nanotubes.

The starting ZnO nanowire templates for this synthetic procedure have diameters of 40-60 nm and lengths of ~10 µm. Thus, the inner tube diameters are around 40-60 nm and the

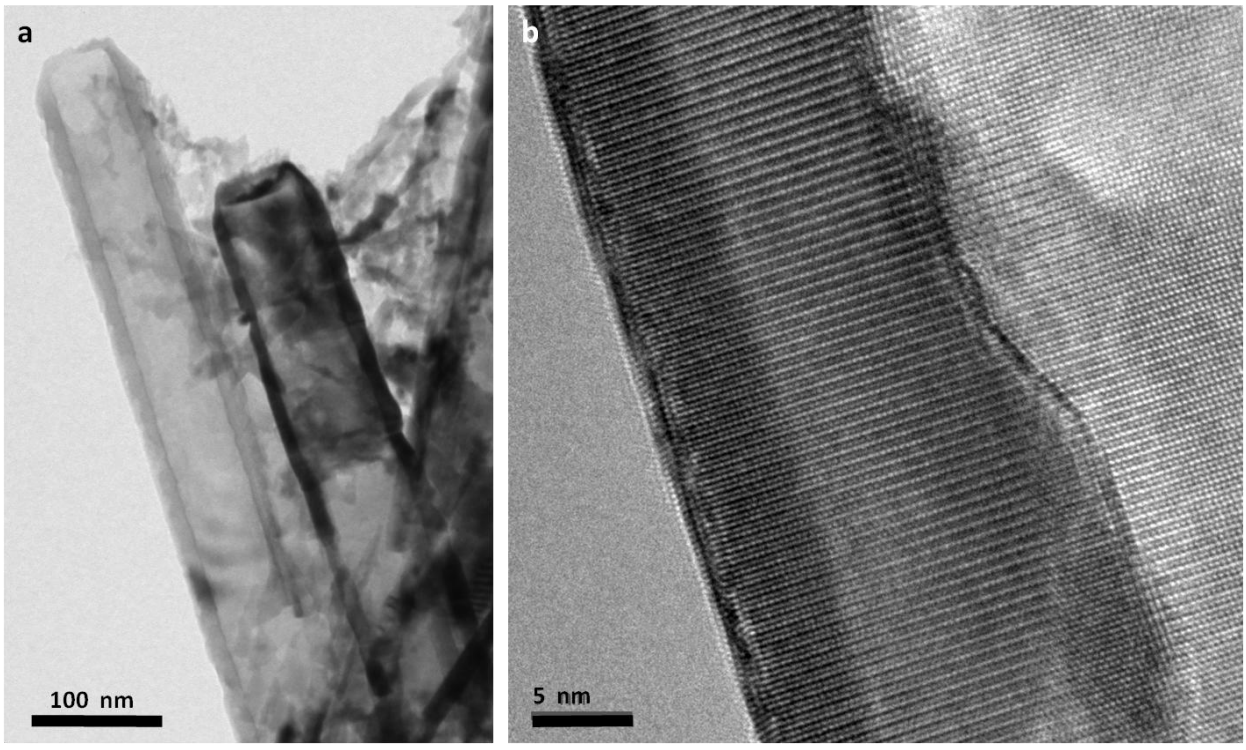

Figure 74 – TEM images of GaN:ZnO nanotubes (Method 2): (a) Low-magnification TEM image of a group of GaN:ZnO nanotubes showing the open tips and hollow interiors. The extraneous material is section of nanotube walls that broke apart during the sonication. (b) HRTEM image of a GaN:ZnO nanotube showing its single-crystallinity.

tube walls are ~20 nm as before. The other material evident in the TEM image in Figure 74a is broken nanotube sections from the lengthy sonication used to break apart the nanotube films. The nanotubes produced by this method are also single-crystalline which is evident in the HRTEM image shown in Figure 74b. The ZnO composition of these GaN:ZnO nanotubes could be controllably tuned from about 10 to 1% simply by increasing the NH_3 etch time. EDS measurements taken at different locations on the same nanotube indicate a high degree of uniformity within the nanotubes, with a standard deviation of only 1.3. It should be noted that the nanotubes can be etched in HCl as well, which results in a slightly higher ZnO compositions. However, the vapor NH_3 etch was generally used because residual HCl left on the nanotubes could affect the water splitting activity since Cl^- is more readily oxidized that H_2O.

4.4.c – Optical Properties of $(Ga_{1-x}Zn_x)(N_{1-x}O_x)$ Nanotubes

Since the goal of alloying the GaN and ZnO was to achieve visible absorption, the optical properties, both absorption and photoluminescence, were characterized. GaN:ZnO nanotubes were synthesized on 1x1 cm transparent quartz substrates for absorption measurements. Due to a large amount of scattering on both the nanowire arrays and films it was necessary to use an integrating sphere setup. The integrating sphere is able to collect scattered and transmitted light enabling measurement of the true absorbance. The illumination source for the absorption measurements was a collimated 300 W Xe lamp. A pinhole was used in the front of the integrating sphere to obtain a small beam at the sample position. The diameter of the beam was approximately 0.5 cm and was positioned in the center of the sample. To calculate the sample absorbance one spectrum was taken in which the beam hit ("hit") the sample and another was taken in which the beam missed ("miss") the sample. A spectrum was also taken in which the sample was not present ("out") in the integrating sphere. There was negligible

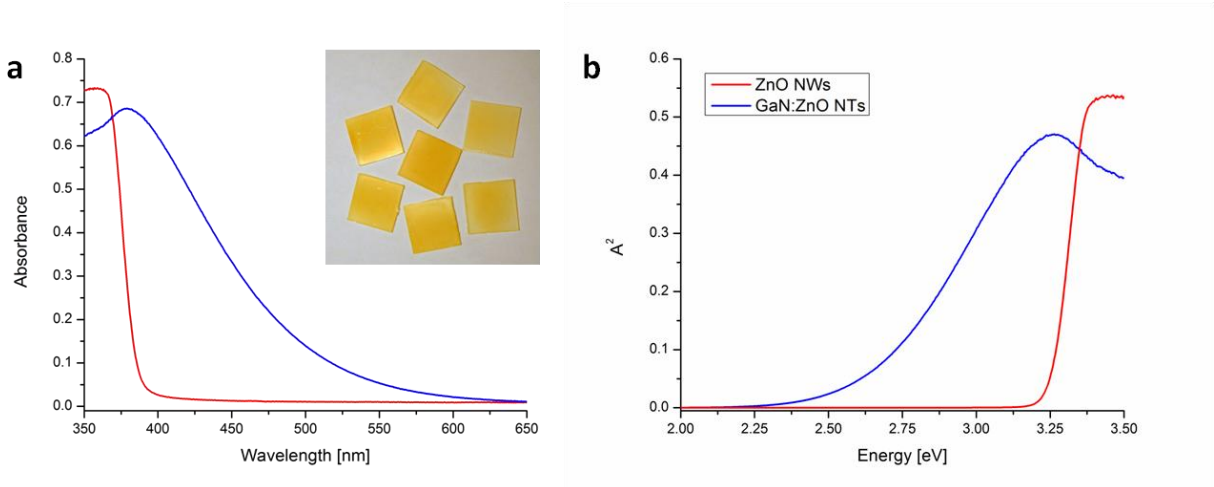

Figure 75 – GaN:ZnO Nanotube Absorbance: (a) Absorbance of a GaN:ZnO nanotube film (blue) and the starting ZnO nanowire film (red). Inset is an image of several GaN:ZnO nanotube films displaying their bright yellow color. Each substrate is 1x1 cm. (b) A^2 vs. energy used to determine the band gap of the GaN:ZnO nanotubes.

difference between the "out" and "miss" spectra indicating that there was very little absorption in the sample after the initial pass of the beam. The absorbance is equal to –log("hit"/"miss").

The absorbance of a GaN:ZnO nanotube film is shown in Figure 75. Compared to the starting ZnO nanowires, which are shown in red, the GaN:ZnO nanotubes shows a significant increase in visible absorption with a tail extending all the way out to about 600 nm. This increase in visible absorption is also evident from the yellow/orange color of the nanotube films shown in the inset in Figure 75a. To determine the bandgap of the nanotubes the square of the absorbance was plotted vs. energy (Figure 75b). A linear fit of the GaN:ZnO nanotube data between 3.15 and 2.75 eV was used to get the x-intercept. Based on the absorbance, the bandgap of the GaN:ZnO nanotubes shifted to 2.63 eV compared to the 3.25 eV bandgap of the starting ZnO nanowires. This significant shift in the bandgap is similar to the results reported by Domen for GaN:ZnO samples with 20% ZnO[13]. However, the GaN:ZnO nanotube sample shown in Figure 75 had a ZnO composition ~8%.

The photoluminescence (PL) of the GaN:ZnO nanotubes was measured using the 325 nm line of a continuous wave HeCd laser. The PL showed a superposition of two broad peaks; the first peak was centered around 500 nm and the second peak was centered around 675 nm (Figure 76). Other nanotube samples only showed one broad peak centered around 675 nm. It's interesting to note that some nanotube samples exhibited broad band edge-like PL that was red-shifted to as far as 419 nm. However, when the same samples were measured 6 months later, the PL closely resembled that of the original ZnO/GaN – core/shell nanowires (and that of the pure ZnO nanowires) and the red-shifted band edge peak was completely absent. It's possible that this change in PL is a result of some amount of phase separation over time, with the final PL dominated by ZnO. No time-dependent change in PL was observed in samples that only showed the broad defect-like peaks shown in Figure 76.

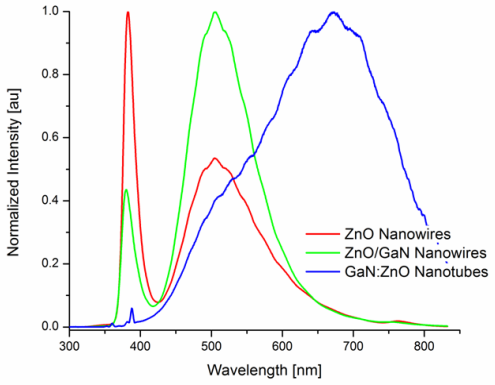

Figure 76 – GaN:ZnO Nanotube Photoluminescence: PL of ZnO, ZnO/GaN nanowires, and the GaN:ZnO nanotube films. The GaN:ZnO nanotubes show two peaks centered around 500 nm and 675 nm.

4.4.d – Photoelectrochemical Water Splitting with $(Ga_{1-x}Zn_x)(N_{1-x}O_x)$ Nanotubes

Previous reports from the Domen group noted that negligible amounts of H_2 and O_2 were detected in water splitting experiments when cocatalysts were not used[10]. Maeda et al. performed an extensive study on a wide variety of cocatalysts to determine which was most effective at enhancing the water splitting efficiency of GaN:ZnO[27]. They found that a mixed oxide of Rh and Cr ($Rh_{2-y}Cr_yO_3$) gave the largest production of H_2 and O_2. Using this $Rh_{2-y}Cr_yO_3$ catalyst they achieved an apparent quantum efficiency of 5.9%[14].

4.4.d.i – Addition of H^+ Reduction Cocatalysts to $(Ga_{1-x}Zn_x)(N_{1-x}O_x)$ Nanotubes

To promote efficient water splitting, $Rh_{2-y}Cr_yO_3$ nanoparticles were added to the surfaces of the GaN:ZnO nanotubes using a procedure similar to that previously reported by the Domen group[10]. Briefly, 1.0 mg of $Na_3Cl_6Rh{\cdot}6H_2O$ and 1.0 mg of $Cr(NO_3)_3{\cdot}xH_2O$ were added to 20 mL of water. The solution was sonicated to fully dissolve the precursors. 1 mL of this solution was added to ~ 3 mg of dry nanotubes (Method 2) in a scintillation vial. The nanotube and cocatalyst solution were sonicated in a heated sonicator for about 3 hours at ~70°C until the water was completely evaporated from the vial. Sonication was used to agitate the nanotubes to enable homogeneous deposition of the cocatalyst precursors. The entire sample was then calcined in air at 350°C for 1 hour to produce the $Rh_{2-y}Cr_yO_3$ nanoparticle cocatalysts.

After calcination, $Rh_{2-y}Cr_yO_3$ nanoparticles decorated both the inner and outer walls of the GaN:ZnO nanotubes (Figure 77). XRD patterns taken after nanoparticle decoration exhibited two new peaks located at 34.5° and 65°. The crystalline nanoparticles were about 2-5 nm in diameter and were well dispersed on the surface. The weight percent of nanoparticles could be tuned by adjusting the amount of precursor that was added to the nanotubes. If too much precursor was used the entire surface of the nanotubes was covered by nanoparticles. Since the O_2 generation occurs directly on the surface of the nanotubes it is important that bare surface remain exposed.

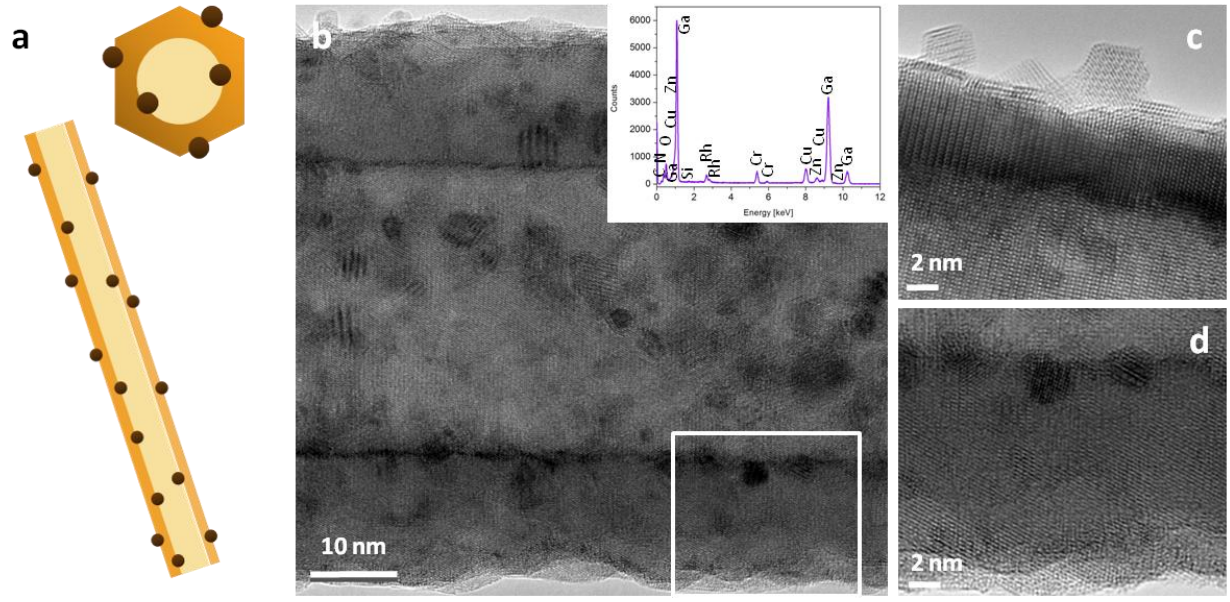

Figure 77 – Addition of $Rh_{2-y}Cr_yO_3$ cocatalysts: (a) Cartoon showing GaN:ZnO nanotubes decorated with $Rh_{2-y}Cr_yO_3$ nanoparticles, (b-d) HRTEM images showing crystalline $Rh_{2-y}Cr_yO_3$ nanoparticles decorated on both the inner and outer surfaces of the nanotube walls. The image in (d) is a close up of the area boxed in image (a). Inset in (b) in an EDS spectrum showing the presence of Rh and Cr.

4.4.d.ii – Photoelectrochemical Water Splitting Measurement Setup

Figure 78 – Custom-made water splitting reactor: Hybrid glass-quartz reactor used for water splitting measurements

Water splitting reactions were carried out in a specially designed 14 mL hybrid glass – quartz reactor (Figure 78). The reactor contained two separate reservoirs. The first reservoir was made of quartz and was used for sample illumination. The second reservoir was used to catch any solution that might bubble over during the sample degassing procedure. The sample was illuminated with a 500 W Hg (Xe) lamp with water filter (Newport/Oriel) through the quartz section of the reactor. The nanotube suspension was loaded into the reactor with a stir bar and sealed with air-free o-ring caps and connectors. The solution was degassed by pulling vacuum on the electrolyte and refilling the reactor with ultra-high purity (UHP) Ar. The reactions were run at ~1 atm and the pressure was monitored during the reaction using a pressure gauge. The reaction gases were automatically injected into an Agilent micro GC with molecular sieve column and TCD detector with Ar carrier gas. The entire setup (Figure 79), including the reactor, GC, and gas delivery lines were enclosed in an acrylic glovebox to prevent leakage of air into the reactor. The lamp was positioned just outside the glovebox and the beam passed through a quartz window in the side of the box to reach the reactor.

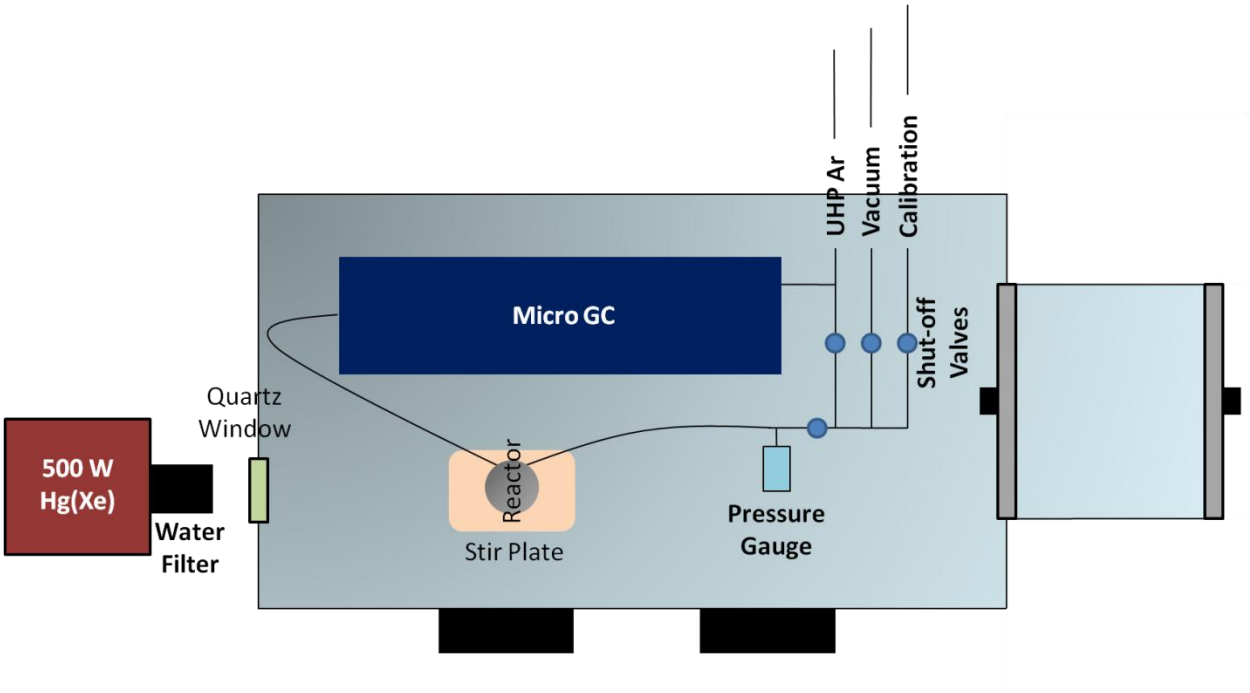

Figure 79 – Schematic of the water splitting setup: Schematic showing the placement of the lamp, GC, and reactor with the glovebox as well as the gas and vacuum lines that were directly connected to the reactor.

The GC was calibrated using 3 different calibration mixtures of H_2 and O_2 gases in UHP Ar from Praxair. The mixtures were as follows: 1) 100 ppm H_2, 100 ppm O_2, 2) 500 ppm H_2, 250 ppm O_2, and 3) 1500 ppm H_2, 750 ppm O_2. The calibration was performed in the same reactor that was used for the water splitting measurements.

4.4.d.iii – Photoelectrochemical Water Splitting with $(Ga_{1-x}Zn_x)(N_{1-x}O_x)$ Nanotubes decorated with $Rh_{2-y}Cr_yO_3$ Cocatalysts

GaN:ZnO nanotubes prepared by method 2 were used for water splitting experiments. Approximately 3 mg of the dried GaN:ZnO nanotubes loaded with $Rh_{2-y}Cr_yO_3$ cocatalysts were used for each reaction (Figure 80). The nanotubes were suspended in 2 mL of aqueous electrolyte adjusted to pH 4.5 with H_2SO_4. To ensure a good dispersion, the solution was sonicated for a few seconds.

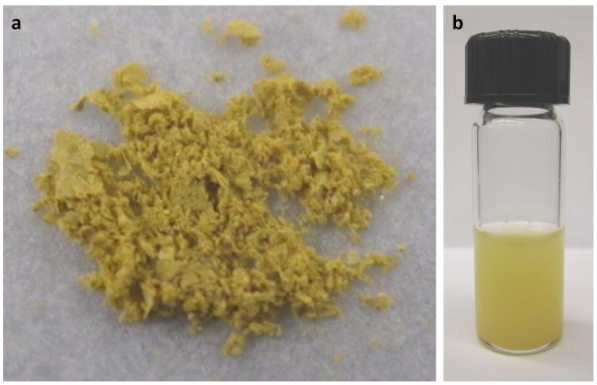

Figure 80 – GaN:ZnO Nanotubes decorated with $Rh_{2-y}Cr_yO_3$ cocatalysts: Optical images showing (a) dried GaN:ZnO nanotubes, and (b) GaN:ZnO nanotubes suspended in electrolyte for water splitting measurements.

After degassing the solution and confirming the complete removal of ambient O_2 and N_2 via GC measurement, the nanotubes were illuminated with a 500 W Hg (Xe) lamp. The solution was stirred continuously to keep the nanotubes suspended. To avoid any possible contamination of the reaction gases, the samples were automatically pulled from the reactor by an internal pump in the micro GC. 2-3 samples were taken for each point to ensure that the samples were representative of the product gases in the reactor head space and not just the gases in the smaller gas delivery lines. To check for air leaks within the reactor the N_2 signal was monitored over time. Simultaneous increases in the N_2 and O_2 signals indicated leakage and the data was discarded.

Figure 81 shows a typical time course for water splitting using 3.75 mg (~45 µmol) of GaN:ZnO nanotubes. For this particular sample, 5 separate measurements were performed, totaling 156 hours of illumination. Both the initial and final measurements show a linear increase in H_2 with comparable H_2 production rates of approximately 0.25 and 0.33 µmol/hour, respectively. A similar rate was observed in the same sample tested at low pressure (20 torr) under water vapor, indicating that the GaN:ZnO nanotubes can be used in both a liquid and vapor phase.

Despite, the constant rate of H_2 production, no O_2 was observed. However, it is clear that something within the reactor is being oxidized. Some photocatalysts, such as TiO_2 and $TiSi_2$, photo-adsorb O_2 onto their surfaces[28,29]. In the case of $TiSi_2$, the O_2 could be removed by heating the photocatalyst/electrolyte solution to temperatures over 100°C. After releasing the O_2 from the surfaces of the $TiSi_2$, a stoichiometric 2:1 ratio of H_2:O_2 was observed. Adsorbed O_2 may also form peroxides on the surface of the photocatalysts. Arakawa et al. found that the addition of Na_2CO_3 to the electrolyte solution resulted in stoichiometric evolution of H_2 and O_2

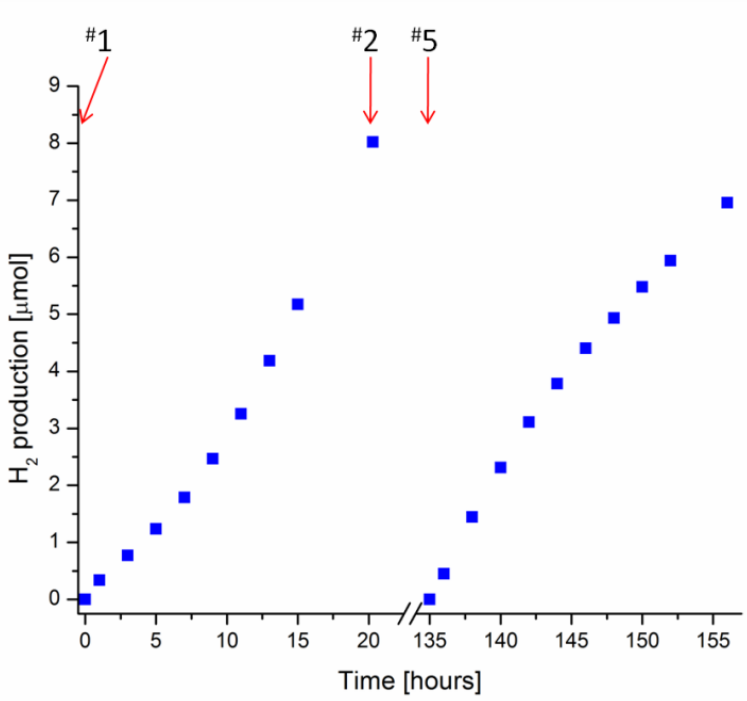

Figure 81 – H_2 generation under illumination on GaN:ZnO nanotubes: Time course showing a linear increase in H_2 production over time. No O_2 was observed. The arrows indicate the start of a new measurement series.

in several photocatalysts[29]. The Na_2CO_3 is believed to accelerate the oxygen desorption through the generation of peroxycarbonate intermediates. Of course, in the case of many semiconductors, especially those with smaller bandgaps, the absence of O_2 can be explained by the photodegradation of the photocatalyst itself.

TEM characterization of the GaN:ZnO nanotubes before and after water splitting experiments show no obvious change in their composition or structure. Also, if the GaN:ZnO nanotubes were being continuously oxidized, there should be a linear increase in N_2 over time[30]. However, this was not observed. In addition, since the same nanotube sample was able to produce H_2 at a steady rate for over 156 hours, it's unlikely that any significant photodegradation occurred.

Similar to TiO_2 and $TiSi_2$, the O_2 may be adsorbed on the GaN:ZnO surface; still the constant rate of H_2 generation indicates that this is not the case. One would expect the H_2 generation to decrease over time as the surface of the semiconductor is covered in oxygen. Even after 66 hours of constant illumination, the GaN:ZnO H_2 rate remained steady. The same result should be expected in the case of surface peroxide formation. In addition, a peroxide test in the solution after illumination showed no evidence of peroxides.

One interesting thing to note is that an additional chemical species was observed in GC chromatograms with elution times around 2.0 min. The peak area of this species increases linearly over time with H_2. Based on this evidence, it's likely that this peak represents some additional product within the system that is serving as a hole scavenger to facilitate H_2 generation. Further experiments are necessary to elucidate the composition of this species.

4.4.e – $(Ga_{1-x}Zn_x)(N_{1-x}O_x)$ Nanotubes: Conclusions

GaN:ZnO nanotubes were successfully synthesized via ZnO nanowire templates using an epitaxial casting approach. The nanotubes were single-crystalline, homogeneous in composition, and exhibited high surface areas. By Method 1, oriented nanotubes were grown

in direct electrical contact with the substrate to facilitate photocurrent measurements. GaN:ZnO nanotube films were synthesized by Method 2 for GC measurements. After decorating the GaN:ZnO nanotubes with $Rh_{2-y}Cr_yO_3$ cocatalysts, the nanotubes showed a linear increase in H_2 under illumination. No O_2 was observed. The oxidation reaction is currently under intense study. It's also unclear at this time why the water splitting behavior of the nanotubes is different from that of the powder photocatalysts reported by the Domen group. Future research should focus on PEC measurements using the oriented nanotube arrays to elucidate more information regarding the photoanodic behavior of the GaN:ZnO nanotubes. Finally, the efficiency of H_2 production should be determined in both that GaN:ZnO nanotube and powder photocatalysts to determine what, if any, enhancement can be achieved by the nanotube morphology.

4.5 – $(In_{1-x-y}Ga_yZn_x)(N_{1-x}O_x)$ Nanotubes

It is well known that III-V alloys, such as InGaN, can offer a wide range of bandgap tunability. InGaN alloys, depending on their composition, can access a range of bandgaps from 1.0 eV all the way to 3.4 eV[31]. Thus, the introduction of In into the GaN:ZnO nanotubes should help to further improve their visible absorption. Kamata et al. reported the synthesis of $In_{5.26}Ga_{19.1}Zn_{13.7}N_{1.4}O_{60.7}$ by nitridation of a Ga-Zn-In-O powder[30]. Unlike the GaN:ZnO materials described in the previous section, this InGaN:ZnO material showed a large deficiency in N due to the low temperature used for the nitridation. The material was not well-crystallized but the band edge was shifted out all the way to 600 nm, exhibiting even more visible absorption than GaN:ZnO with a similar Ga/Zn ratios. Despite the poor crystallinity, InGaN:ZnO was able to generate H_2 and O_2 in the presence of hole and electron scavengers, respectively.

Using an epitaxial casting approach it could be possible to synthesize single-crystal InGaN:ZnO nanotubes with stoichiometric N compositions. Since the N2p orbitals are responsible for shifting the VBM to less positive potentials (reducing the bandgap), it's important that N be present in stoichiometric proportions. By using a direct growth of the nitride rather than a nitridation of the oxide material, it should be possible to achieve a more correct N composition.

4.5.a – Synthesis of $(In_{1-x-y}Ga_yZn_x)(N_{1-x}O_x)$ Nanotubes

,

InGaN:ZnO nanotubes were synthesized using the same procedure given in 4.4.a.i with the addition of a trimethyl indium (TMI) precursor. The TMI was heated to ~30°C to achieve the desired vapour pressure. 5-50 sccm of N_2 were bubbled through the TMI bubbler before being combined with the TMG and N_2 dilution gases in the inner quartz tubes. The TMI and TMG were reacted with NH_3 at the output of the inner tube. All other synthetic conditions were the same.

4.5.b – Structure and Composition of $(In_{1-x-y}Ga_yZn_x)(N_{1-x}O_x)$ Nanotubes

Using the oriented ZnO nanowire array template, vertical arrays of InGaN:ZnO nanotubes were synthesized with diameters of ~100 nm and lengths of ~800 nm (Figure 82). The surfaces of the nanotubes appear corrugated in the SEM images, and upon closer look, the nanotubes seem to be porous (Figure 82b). This porous structure may have resulted from the thermal instability of InN during the 700°C NH_3 etch[30].

The In composition of the InGaN:ZnO nanotubes could be controlled by changing the flow rate through the TMI bubbler. At 5 sccm the composition was ~0.5% while at 50 sccm it was ~7.0% (by EDS). It's probable that higher In compositions could be achieved by using higher flow rates. The ZnO composition was similar to that of the GaN:ZnO nanotubes with compositions between 8 and 10% for samples etched under NH_3 for 30 min. At this time the O and N content of the InGaN:ZnO nanotubes is unknown. However, since the InGaN was synthesized by direct reaction of TMG and TMI with NH_3 the composition should be close to the stoichiometric ratio of ~90% (compared to O). XRD patterns indicate that the nanotubes have a wurtzite crystal structure, as expected. HRTEM images and electron diffraction patterns taken of the InGaN:ZnO nanotubes indicate that they are single crystalline (Figure 82d).

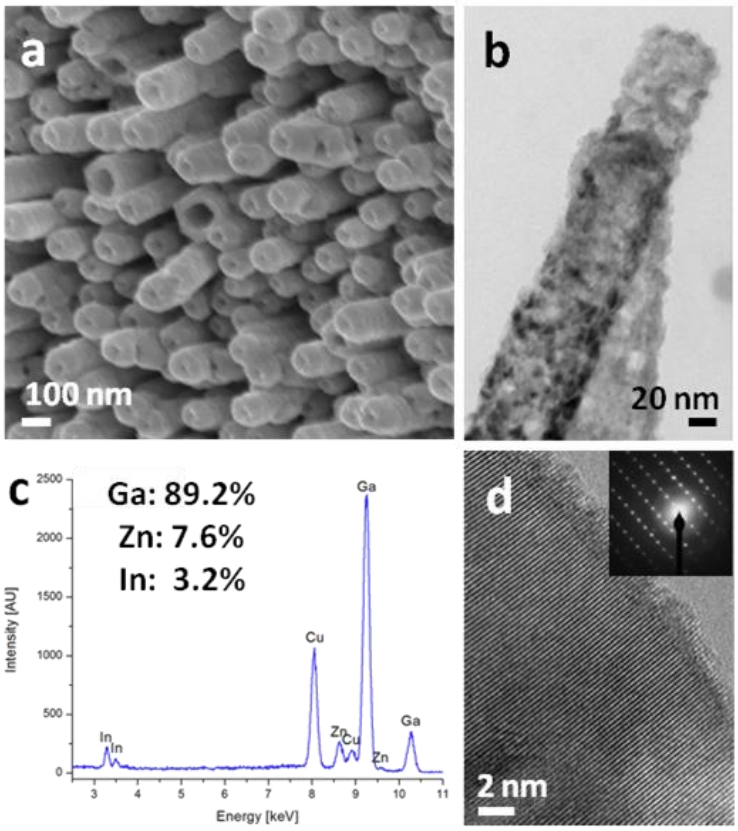

Figure 82 – SEM, TEM, and EDS of InGaN:ZnO Nanotubes: (a) SEM image of an InGaN:ZnO nanotube array taken at a 45° tilt. (b) Low-magnification image of a group of InGaN:ZnO nanotubes showing a seemingly porous structure. (c) EDS spectrum taken from a group of InGaN:ZnO nanotubes. (d) HRTEM image showing the single crystallinity of the InGaN:ZnO nanotubes. Inset is an ED pattern.

4.5.c – Optical Properties of $(Ga_{1-x}Zn_x)(N_{1-x}O_x)$ Nanotubes

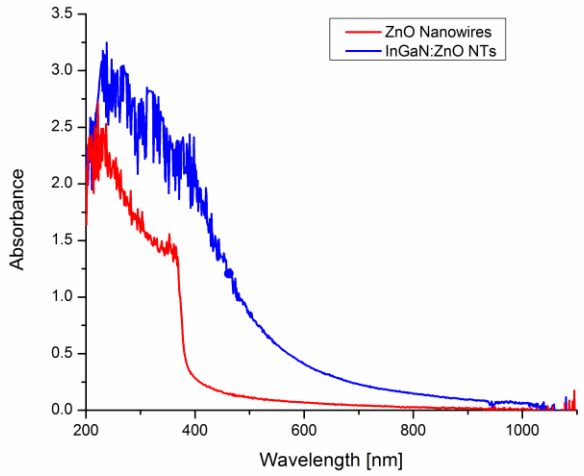

Figure 83 – InGaN:ZnO Nanotube Absorbance: Absorbance of an InGaN:ZnO nanotube array (In: 3.7%, Ga: 91.3%, Zn: 4.9%) and the starting ZnO nanowire array highlighting the increase in visible absorption in the nanotubes.

The InGaN:ZnO nanotubes synthesized by this method appeared orange-ish brown in color, indicative of visible absorption. The absorbance of InGaN:ZnO nanotubes grown on quartz substrates was analyzed using a UV-Vis equipped with a special fiber setup. The setup consisted of 2 optical fibers, each connected to a collimator. The first fiber was used to deliver the light to the sample while the second was used to collect the light transmitted through the sample. The fibers were carefully aligned to achieve a maximum transmission signal. Absorbance spectra taken of the InGaN:ZnO nanotubes exhibited a significant increase in visible absorption (Figure 83). Unfortunately, since these measurements were not taken using an integrating sphere it is difficult to determine whether the absorption tail that extends across the visible range is from true absorbance or from scattering. However, using absorbance spectra taken from InGaN:ZnO nanotubes with varying compositions it was clear that in nanotubes with similar ZnO compositions, the band gap decreased with increasing In composition. This indicates that the presence of In effectively reduced the bandgap of the nanotubes. Further investigation into the optical properties of this material should be pursued in the future.

4.5.d – $(In_{1-x-y}Ga_yZn_x)(N_{1-x}O_x)$ Nanotubes: Conclusions

InGaN:ZnO nanotubes with In compositions up to 7% and Zn compositions up to 10% were synthesized using a epitaxial casting of InGaN onto ZnO nanowire templates. The In composition could be tuned by varying the concentration of TMI during the synthesis. The InGaN:ZnO nanotubes were single crystalline and exhibited enhanced visible absorption compared to both the starting ZnO nanowires and the GaN:ZnO nanotubes synthesized by similar methods. Future research should focus on more in-depth structural and optical characterization of this material. It would also be of particular interest to test the water splitting activity of InGaN:ZnO nanotubes under visible light.

4.6 – References

1. Fujishima, A. and K. Honda, *Electrochemical Photolysis of Water at a Semiconductor Electrode.* Nature, 1972. **238**(5358): p. 37-38.
2. Ni, M., et al., *A review and recent developments in photocatalytic water-splitting using TiO2 for hydrogen production.* Renewable & Sustainable Energy Reviews, 2007. **11**(3): p. 401-425.
3. Kato, H. and A. Kudo, *New tantalate photocatalysts for water decomposition into H-2 and O-2.* Chemical Physics Letters, 1998. **295**(5-6): p. 487-492.
4. Kato, H., K. Asakura, and A. Kudo, *Highly efficient water splitting into H-2 and O-2 over lanthanum-doped NaTaO3 photocatalysts with high crystallinity and surface nanostructure.* Journal of the American Chemical Society, 2003. **125**(10): p. 3082-3089.
5. Ikarashi, K., et al., *Photocatalysis for water decomposition by RuO2-dispersed ZnGa2O4 with d(10) configuration.* Journal of Physical Chemistry B, 2002. **106**(35): p. 9048-9053.
6. Maeda, K. and K. Domen, *New non-oxide photocatalysts designed for overall water splitting under visible light.* Journal of Physical Chemistry C, 2007. **111**(22): p. 7851-7861.
7. Maeda, K., et al., *GaN : ZnO solid solution as a photocatalyst for visible-light-driven overall water splitting.* Journal of the American Chemical Society, 2005. **127**(23): p. 8286-8287.
8. Wei, W., et al., *Origin of the visible light absorption of GaN-Rich Ga1-xZnxN1-xOx (x=0.125) solid solution.* Journal of Physical Chemistry C, 2008. **112**(40): p. 15915-15919.
9. Maeda, K., et al., *Overall water splitting using (oxy)nitride photocatalysts.* Pure and Applied Chemistry, 2006. **78**(12): p. 2267-2276.
10. Maeda, K., et al., *Photocatalyst releasing hydrogen from water - Enhancing catalytic performance holds promise for hydrogen production by water splitting in sunlight.* Nature, 2006. **440**(7082): p. 295-295.
11. Maeda, K., et al., *Overall water splitting on (Ga1-xZnx)(N1-xOx) solid solution photocatalyst: Relationship between physical properties and photocatalytic activity.* Journal of Physical Chemistry B, 2005. **109**(43): p. 20504-20510.
12. Yashima, M., et al., *Crystal structure and optical properties of (Ga1-xZnx)(N1-xOx) oxynitride photocatalyst (x=0.13).* Chemical Physics Letters, 2005. **416**(4-6): p. 225-228.
13. Maeda, K. and K. Domen, *Solid Solution of GaN and ZnO as a Stable Photocatalyst for Overall Water Splitting under Visible Light.* Chemistry of Materials, 2010. **22**(3): p. 612-623.
14. Maeda, K., K. Teramura, and K. Domen, *Effect of post-calcination on photocatalytic activity of (Ga1-xZnx)(N1-xOx) solid solution for overall water splitting under visible light.* Journal of Catalysis, 2008. **254**(2): p. 198-204.
15. Law, M., J. Goldberger, and P.D. Yang, *Semiconductor nanowires and nanotubes.* Annual Review of Materials Research, 2004. **34**: p. 83-122.
16. Shen, G.Z., Y. Bando, and D. Golberg, *Recent developments in single-crystal inorganic nanotubes synthesised from removable templates.* International Journal of Nanotechnology, 2007. **4**(6): p. 730-749.
17. Lu, M.C., et al., *Synthesis and formation mechanism of gallium nitride nanotubular structure.* Electrochemical and Solid State Letters, 2005. **8**(7): p. G153-G155.

18. Xie, X., et al., *Zn-Doped Gallium Nitride Nanotubes with Zigzag Morphology.* Journal of Physical Chemistry C, 2009. **113**(33): p. 14633-14637.
19. Hu, J.Q., et al., *Growth of single-crystalline cubic GaN nanotubes with rectangular cross-sections.* Advanced Materials, 2004. **16**(16): p. 1465-1468.
20. Hu, J.Q., et al., *Gallium nitride nanotubes by the conversion of gallium oxide nanotubes.* Angewandte Chemie-International Edition, 2003. **42**(30): p. 3493-3497.
21. Liu, B.D., et al., *Wurtzite-type faceted single-crystalline GaN nanotubes.* Applied Physics Letters, 2006. **88**(9): p. 093120.
22. Goldberger, J., et al., *Single-crystal gallium nitride nanotubes.* Nature, 2003. **422**(6932): p. 599-602.
23. Thapa, S.B., et al., *MOVPE growth of GaN around ZnO nanopillars.* Journal of Crystal Growth, 2008. **310**(23): p. 5139-5142.
24. Greene, L.E., et al., *General route to vertical ZnO nanowire arrays using textured ZnO seeds.* Nano Letters, 2005. **5**(7): p. 1231-1236.
25. Yuhas, B.D., et al., *Transition-metal doped zinc oxide nanowires.* Angewandte Chemie-International Edition, 2006. **45**(3): p. 420-423.
26. Hashiguchi, H., et al., *Photoresponse of GaN:ZnO Electrode on FTO under Visible Light Irradiation.* Bulletin of the Chemical Society of Japan, 2009. **82**(3): p. 401-407.
27. Maeda, K., et al., *Improvement of photocatalytic activity of (Ga1-xZnx)(N1-xOx) solid solution for overall water splitting by co-loading Cr and another transition metal.* Journal of Catalysis, 2006. **243**(2): p. 303-308.
28. Ritterskamp, P., et al., *A titanium disilicide derived semiconducting catalyst for water splitting under solar radiation - Reversible storage of oxygen and hydrogen.* Angewandte Chemie-International Edition, 2007. **46**(41): p. 7770-7774.
29. Arakawa, H. and K. Sayama, *Solar hydrogen production. Significant effect of Na2CO3 addition on water splitting using simple oxide semiconductor photocatalysts.* Catalysis Surveys from Japan, 2000. **4**(1): p. 75-80.
30. Kamata, K., et al., *Synthesis and photocatalytic activity of gallium-zinc-indium mixed oxynitride for hydrogen and oxygen evolution under visible light.* Chemical Physics Letters, 2009. **470**(1-3): p. 90-94.
31. Kuykendall, T., et al., *Complete composition tunability of InGaN nanowires using a combinatorial approach.* Nature Materials, 2007. **6**(12): p. 951-956.

Appendix A:
List of Publications and Patents

Publications:

M. Fardy, C. Nguyen, M. Natera Comte, and P. Yang, "$(Ga_{1-x}Zn_x)(N_{1-x}O_x)$ Nanotubes for Photoelectrochemical H_2 Production", in preparation.

M. Fardy*, S. Andrews*, M. Moore*, S. Aloni, M. Zhang, V. Radmilovic, and P. Yang, "Atomic-Level Control of the Thermoelectric Properties in Polytypoid Nanowires", *Chem. Sci.* (2010) (*co-authors).

J. Tang, H.-T. Wang, D. H. Lee, **M. Fardy**, Z. Huo, T. P. Russell, and P. Yang, "Holey Silicon as efficient thermoelectric material", *Nano Lett*. **10**, 4279 (2010).

P. Yang, R.Yan, and **M. Fardy**, "Semiconductor nanowires, what's next?" *Nano Lett.* **10**, 1529 (2010).

W. Liang, O. Rabin, A. Hochbaum, **M. Fardy**, M. Zhang, and P. Yang, "Thermoelectric Properties of p-type PbSe Nanowires", *Nano. Res.,* **2**, 394 (2009).

W. Liang, A. Hochbaum, **M. Fardy**, M. Zhang, and P. Yang, "Field-Effect Modulation of Seebeck Coefficient in Single PbSe nanowires", *Nano. Lett.,* **9**, 1689 (2009).

Z. Huo, F. Tsung, W. Huang, **M. Fardy**, R. Yan, Y. Li, X. Zhang, and P. Yang, "Self-Organized Ultrathin Oxide Nanocrystals", *Nano. Lett.,* **9**, 1260 (2009).

M. Fardy and P. Yang, "Lilliputian light sticks", (News and Views), *Nature,* **451**, 408 (2008).

M. Fardy*, A. Hochbaum*, J. Goldberger, and P. Yang, "Synthesis and Thermoelectric Characterization of Lead Chalcogenide Nanowires", *Adv. Mater***. 19**, 3047 (2007) (*co-authors).

L. D'Ottone, D. Bauer, P. Campuzano-Jost, **M. Fardy**, and A.J. Hynes. "Kinetic and mechanistic studies of the recombination of OH with NO_2: Vibrational deactivation, isotopic scrambling, and product isomer branching ratios." *Faraday Discuss.* **130**, 111 (2005)

L. D'Ottone, D. Bauer, P. Campuzano-Jost, **M. Fardy**, and A.J Hynes. "Vibrational deactivation studies of OH X $^2\Pi$ (v = 1-5) by N_2 and O_2" *Phys. Chem. Chem. Phys.* **6**, 4276 (2004)

Patents:

J. Goldberger, **M. Fardy**, O. Rabin, A. Hochbaum, M. Zhang, and P. Yang
"Method of non-catalytic formation and growth of nanowires"
United States Patent: 7781317

W. Liang, A. Hochbaum, **M. Fardy**, O. Rabin, M. Zhang, and P. Yang
"Process for altering the thermoelectric properties of a material"
United States Patent Application: 20090293928